universität wien

MASTERARBEIT | MASTER'S THESIS

Titel | Title

Highly siderophile element and Re-Os isotope compositions of the 3.5 Ga Tomka Iron Formation, Daitari Greenstone Belt, India

verfasst von | submitted by

Aubert Salzmann BSc

angestrebter akademischer Grad | in partial fulfilment of the requirements for the degree of

Master of Science (MSc)

Wien | Vienna, 2025

Studienkennzahl lt. Studienblatt | Degree programme code as it appears on the student record sheet:	UA 066 815
Studienrichtung lt. Studienblatt | Degree programme as it appears on the student record sheet:	Masterstudium Erdwissenschaften
Betreut von | Supervisor:	Univ.-Prof. i.R. Dr. Christian Köberl
Mitbetreut von | Co-Supervisor:	Dipl.-Min. Dr. Toni Schulz

Table of contents

Abstract

Banded Iron Formation (BIF) are marine-chemical sedimentary rocks rich in iron (12-40 wt.%) and confined to the Precambrian. They are considered valuable geochemical archives for recording ancient seawater compositions and redox conditions of the early Earth.

This study focused on the ~3.5-3.3 Ga Tomka BIF, located in the Daitari Greenstone Belt of the Singhbhum Craton in eastern India. This work investigates the distribution of highly siderophile elements (HSEs) and aims to apply the Re-Os isotopic system in an attempt to construct an isochron and assess whether the Os isotopic composition reflects its pristine Archean seawater signal. This marks the Tomka BIF as the oldest BIF to date in which this approach has been applied.

Using established wet chemistry techniques and isotope dilution methods, Os and other HSEs were extracted from the whole-rock powdered samples representing different lithologies (shale, Fe-rich-, chert-, and mixed layers). Osmium content and isotopic composition were analyzed using N-TIMS, while the remaining HSE concentrations were determined using ICP-MS. The Tomka BIF has average Ir concentrations of ~0.03 ppb, providing no indication of extraterrestrial input. The samples contain minimal to no syn-depositional (detrital) alterations, due to the very low concentrations of Al and Zr, which are indicative of such alterations, and only variable to little amount of post-depositional alterations based on its Sr contents. Six samples of the Tomka BIF with PUM-like $^{187}Os/^{188}Os$ initial ratio (~0.13) were used to construct a Re-Os regression line, interpreted to represent a partially closed Re-Os system. This yields a calculated age of 3,557 ± 668 Ma, which falls within the range of existing age estimates (~3.51 to ~3.28 Ga).

The $^{187}Os/^{188}Os_{(i)}$ ratio derived from the regression line (~0.11) is interpreted as a proxy for the global Archean seawater Os budget. This primitive upper mantle (PUM)-like initial Os isotope ratio aligns with the existing scarce Archean data, which are thus far mainly based on organic-rich mudrocks, and it suggests a dominant contribution of unradogenic material delivering mantle-like Os to the depositional zone. This contrasts with a more radiogenic Os seawater signature in the Proterozoic, which was far more influenced by oxidative weathering of the felsic continental crust.

Zusammenfassung

Bändereisenerze (BIFs) sind marin-chemisch sedimentäre Gesteine mit einem hohen Eisengehalt (12-40 wt. %) und sind auf das Präkambrium beschränkt. Sie gelten als bedeutende geochemische Archive zur Rekonstruktion der Zusammensetzung des Meerwassers und der Redoxbedingungen auf der frühen Erde.
Diese Studie konzentrierte sich die etwa 3,5-3,3 Milliarden Jahre alte Tomka-BIF, die sich im Daitari-Grünsteingürtel des Singhbhum-Kratons im Osten Indiens befindet. Untersucht wurden die Verteilung von hoch siderophilen Elementen (HSEs) sowie die Anwendung des Re-Os-Isotopensystems mit dem Ziel eine Isochrone zu konstruieren und zu prüfen, ob die Os-Isotopenzusammensetzung ein ursprüngliches archaisches Meerwassersignal reflektiert. Die Tomka BIF stellen hierdurch die bislang ältesten BIFs dar, an denen diese Methodik angewendet wurde.

Mittels etablierter nasschemischer Verfahren und Isotopenverdünnungsmethoden, wurde Osmium und andere HSEs aus den gemahlenen Gesteinsproben extrahiert, welche die verschiedenen Lithologien repräsentieren (Schiefer, Fe-reich, Chert, und gemischte Lagen). Die Osmium Konzentration und die Os-Isotopenzusammensetzung wurden mittels N-TIMS bestimmt, während die übrigen HSE-Konzentrationen mit ICP-MS analysiert wurden. Die Tomka-BIF weist durchschnittliche Ir-Konzentrationen von ~0.03 ppb auf, was keinen Hinweis auf extraterrestrischen Beitrag liefert. Die Proben zeigen weiters sehr niedrige Konzentrationen von Al und Zr was auf nur minimale bis keine detritalen Alterationen hindeutet und einen variablen bis geringen Grad an post-depositionaler Alterationen, basierend auf den Sr-Gehalten. Sechs Proben, welche ein PUM-ähnliches initiales $^{187}Os/^{188}Os$-Verhältnis (~0.13) besitzen, wurden zur Konstruktion einer Re-Os-Regressionslinie verwendet. Diese wird als Ausdruck eines teilweise geschlossenen Re-Os-Systems interpretiert. Dadurch wird ein berechnetes Modellalter von 3,557 ± 668 Ma erhalten, welches innerhalb des Bereichs des existierenden Altersrahmens (~3.51 bis ~3.28 Ga) liegt.

Das aus der Regressionslinie abgeleitete $^{187}Os/^{188}Os_{(i)}$-Verhältnis (~0.11) wird als Näherungswert für das globale archaische Os-Budget im Meerwasser interpretiert. Dieses „primitive upper mantle“ (PUM)-ähnliche Initialverhältnis stimmt mit der bislang geringen Datenlage für das Archaikum überein, welches bisher hauptsächlich von organisch-reichem Schlammgestein (organic-rich mudrock) stammt. Dieses Ergebnis

deutet auf eine dominante Zufuhr von unradiogenem Osmium aus Tiefsee-Hydrothermalschlot-systemen mit mantelähnlicher Signatur hin. Dies steht im Gegensatz zu den radiogenen Meerwassersignaturen des Proterozoikums, welche stärker durch oxidative Verwitterung der felsischen kontinentalen Kruste beeinflusst waren.

Acknowledgments

I would like to express my gratitude to everyone who supported me during the process of working and writing on my master thesis and all those who have contributed to it.

First and foremost, I would like to thank my supervisors Univ.-Prof. Dr. Christian Köberl and Dr. Toni Schulz for making this thesis possible, for sharing their knowledge and helping me throughout the process of this thesis.

I would especially like to thank Dr. Toni Schulz for his tireless and unwavering support, for his patience in teaching me the necessary laboratory and analytical techniques to obtain my results, but also for helping me in shaping this thesis as a whole. Without his endless help this thesis would not have been possible.

Furthermore, I want to thank Dr. Sebastian Viehmann for his support and for sharing knowledge about the topic of this thesis, but also for providing the samples, together with Dr. Jaganmoy Jodder.

Lastly, I would like to thank my family and friends, whose constant support encouraged me and helped me going during the writing of this thesis.

Acknowledgment of the usage of AI

I acknowledge the use of the AI tool ChatGPT (https://chatgpt.com/) to help me in the refinement of my academic language and to generally identify improvements in the writing style. I confirm that I have read and understood the AI usage guidelines from the University of Vienna and that this thesis complies with them.

List of Tables

List of Figures

List of Abbreviations

BIF ..... Banded Iron Formation
$CHCl_3$ ..... Chloroform
DGB ..... Daitari Greenstone Belt, Daitari Greenstone Belt
DROsS ..... Durham Romil Osmium Standard
GIF ..... Granular Iron Formation
GOBE ..... Great Ordovician Biodiversification Event
H_2SO_4 ..... Sulfuric acid
HBr ..... Hydrobromic acid
HCl ..... Hydrochloric acid
HFSEs ..... High Field Strength Elements
HNO_3 ..... Nitric acid
HREE ..... Heavy Rare Earth Element
HSE ..... Highly siderophile elements
ICP-MS ..... Inductively Coupled Plasma Mass Spectrometry
IF ..... Iron Formations
IOG ..... Iron Ore Group
MIF ..... Micritic Iron Formation
MSWD ..... Mean Square of the Weighted Deviates
OKUM ..... Ontario komatiite ultramafic
OMG ..... Older Metamorphic Group
OMTG ..... Older Metamorphic Tonalite Gneiss
ORM ..... Organic-rich mudrocks
PTFE ..... Polytetrafluoroethylene
PTME ..... Permo Triassic Mass Extinction
REE ..... Rare Earth Elements
SC ..... Singhbhum Craton
SGBC ..... Singhbhum Granite Batholitic Complex
TIMS ..... Thermal Ionization Mass Spectrometer
TTG ..... Tonalite-Trondhjemite-Granodiorite
YMS ..... Yunmengshan

Objective of the thesis

The current understanding of the redox evolution of the Archean hydrosphere and atmosphere, as well as the development of the emerged continental lithosphere remains incomplete. One way to fill these gaps in the understanding of Earth's history is through the study of banded iron formations (BIFs). These marine sediments represent spatio-temporal archives for seawater signatures. Due to its redox-sensitivity, the Re-Os isotope system provides the potential to reconstruct the depositional environment of these chemical sediments (Bekker et al., 2014). Prior Re-Os studies of Precambrian BIFs (Schulz et al., 2021; Prost et al., 2024) demonstrated that after deposition the system remained isotopically partly closed, allowing for constraints of the approximate depositional ages. However, more Re-Os studies on BIFs are necessary.

This study focuses on what it thought to be one of the oldest best-preserved BIFs, the ~ 3.5 Ga Tomka BIF in Eastern India. This study aims to address the following questions:

1. Does the BIF behave as an open or closed system? Before considering the samples as representing primary Re-Os seawater signatures, all samples will be screened for potential syn- and/or post-depositional alterations to ensure the Re-Os-isotope data accurately reflects the depositional environment.
2. Can a first direct dating of the Tomka BIF be achieved? The Re-Os isotopic system will be utilized to construct a regression line in the $^{187}Os/^{188}Os$ vs. $^{187}Re/^{188}Os$ diagram, potentially providing the first direct dating attempt of the Tomka BIF, including a discussion about the meaning of this "age" (depositional vs. secondary overprint).
3. Which sources contributed to the Archean Os isotopic seawater composition? The $^{187}Os/^{188}Os$ signature can serve as an indicator to assess the influence of contributions to the seawater columns from which the BIF precipitated of (i) early emerged continents (in the form of potentially radiogenic detritus and/or riverine influx via oxidative Re mobilization) and (ii) less radiogenic (mantle-like) deep-sea hydrothermal vent systems.
4. How do the results compare to previous BIFs? The results of this study will be placed into a broader context by: (i) comparing the Re-Os data from the Tomka BIF with those of other BIFs to trace temporal trends in the marine Os isotope

record, evaluate differences in system behavior and to asses possible similarities in isotopic composition, and (ii) integrating this data into a larger framework for reconstructing Precambrian redox conditions and seawater composition, also considering Re-Os studies on organic-rich mudrocks (ORM) and carbonates.

1 Introduction

1.1 Evolution of the atmosphere and hydrosphere through time

The Hadean Eon, started around at 4.567 Ga with the accretion of the Earth and ending around at 4.0 Ga with the upper boundary being set by the formation of the oldest rocks we know, the Acasta Gneiss (Bowring and Williams, 1999). This ~0.5 Gyr period of no rock record causes many propositions and models debating the nature of oceans and the early atmosphere (e.g. Stern and Bleeker, 1998). The only confirmed remnants of the Hadean crust are provided by the Jack Hills zircons, with an age of around 4.4 Ga, which have been argued (based on δ^{18}signatures) to contain evidence for the earliest existence of water on the Hadean Earth (Wilde et al., 2001; Harrison, 2009; Andreasen and Sharma, 2009; O'Neil et al., 2011; Lowenstein et al., 2014). A major question coupled with the existence of water is first and foremost its source. There are multiple hypotheses, and it is very likely that they all played a role in the efforts to explain the origin of the water. One being the acquisition of water directly from the solar nebula (Mottl et al., 2007, and references therein), another being the accumulation of water through "wet" accretion of terrestrial building blocks (Drake and Righter, 2002; Drake, 2005). Prominently advocated in the past is the hypothesis of late impacts of comets and carbonaceous chondrites (Mottl et al., 2007; Lowenstein et al., 2014) capable of delivering significant volatile inventories that could explain the existence of terrestrial oceans. Whatever the source, based on the information extracted from the Jack Hills zircons, oceans could have been existing from around 4.4 Ga (Harrison, 2009), although the oldest confirmed marine sediments, those (Isua supracrustal belt of southern west Greenland), are, with an age of around 3.8 Ga, around 500 Myr younger (Nutman et al., 1997; Valley et al., 2002). The early oceans are assumed to be characterized by their anoxic and ferruginous conditions (Poulton and Canfield, 2011). Based on the sulfur isotope record of Archean sediments and the abrupt demise of mass-independent fractionation signatures ($\Delta^{33}S$) (indicating very low O_2 levels) at around 2450 Ma, an oxygenation of the terrestrial hydro- and atmosphere system was proposed, culminating in the "Great Oxidation Event" (Farquhar et al., 2000; Holland, 2002; Lowenstein et al., 2014). The Great Oxidation Event (GOE) describes a steep increase in the abundance of oxygen in the Earth's atmosphere, probably triggered by a combination of abiogenic and biogenic processes, the latter including the onset and rise of photosynthesis (Lyons et al., 2014, 2024). Even though free oxygen was

available, the deep oceans likely continued to be anoxic. This was hypothesized by Canfield (1998), arguing that the oxygen concentration was not high enough to "ventilate" the deep oceans. Prior to the globally detectable GOE, oxygen whiffs (Figure 1.1) might have created local oxygen oases (Holland, 2006; Olson et al., 2013). Following the GOE, oxygen levels did not remain stable but experienced less oxic excursions over a few hundred million years, probably caused by a multitude of biochemical effects (Anbar et al., 2007; Lyons et al., 2014). However, after the GOE, at around 1.8 Ga, the existence of BIFs came to a sudden demise, and remained absent from the geological rock record until their reappearance in the Neoproterozoic (Holland, 2006; Lowenstein et al., 2014). A proposed reason could be a decrease in deep-sea hydrothermal vent activity, but there is only limited data available for it around this time period (Condie et al., 2009). Another being an increase in sulfide production leading to the removal of the dissolved iron in the oceans as iron sulfides, i.e., pyrites (Canfield, 1998).

The state of the oceans during the Mesoproterozoic is disputed (Lowenstein et al., 2014), with dominantly euxinic (anoxic and rich in H_2S) deep oceans (Canfield oceans) being a popular model (Canfield, 1998). Though it has lost favor, because of the limited data being better explained by iron-rich anoxic conditions and euxinic conditions being limited to mid-depth ocean margins (Lyons et al., 2009; Poulton and Canfield, 2011; Planavsky et al., 2011). Thus, it is now believed that the oceans during the era of the "boring billion" (between 1.85 to 0.85 Ga; Holland, 2006) were oxic at the surface, euxinic in mid-depth waters and ferruginous, meaning anoxic but iron rich, in the deep-sea (Shen, 2002; Lowenstein et al., 2014; Lyons et al., 2014). The small IF deposits during this time period can be explained by episodical hydrothermal activity which, on rare occasions, delivered ferrous iron towards shallower waters where it underwent oxidation and precipitated as Fe(III) oxyhydroxide particles (Bekker et al., 2014).

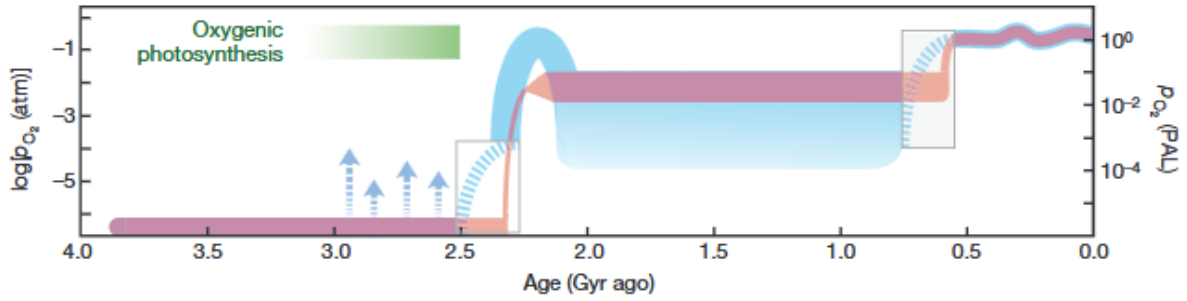

Figure 1.1: *Diagram illustrating the evolution of atmospheric oxygen through Earth's history. Two different models are being recorded here: The red curve indicates a two-step evolution of atmospheric oxygen, while the blue curve argues for an emerging model (modified after Lyon et al., 2014).*

With the Neoproterozoic, around 0.85 Ga ago, the oxygen concentration in the atmosphere as well as the sulphate content of the oceans began to increase up to near present-day conditions (see Figure 1.1; Holland, 2006). Most prominent in this era were the glaciations of the Cryogenian age, the Sturtian (<740-647 Ma) and the Marinoan (<660-635 Ma) glaciations, together with the Gaskier (~580 Ma) glaciation in the Ediacarian period. The global extent of these glaciations, and how they came to be, are still debated (Hyde et al., 2000; Fairchild and Kennedy, 2007). The proposal of a completely snow-covered Earth ("Snowball Earth") for the Sturtian and the Marinoan glaciation, happening due to the albedo effect (e.g. Hoffman and Schrag, 2002; De Vrese et al., 2021, and references therein), is the most widely known hypothesis, though alternative models also do exist. Another idea is that Earth was completely covered in ice, except the regions around the equator ("Slushball Earth") (Hyde et al., 2000; Hoffman and Schrag, 2002). With the Neoproterozoic Oxidation Event another major change of the atmospheric chemistry took place, caused by an increase in burial rate of organic carbon. This reduces processes that consume oxygen (Canfield et al., 2007; Och and Shields-Zhou, 2012; Lyons et al., 2014).

During the Phanerozoic the atmospheric oxygen levels varied considerably (Holland, 2006). Throughout the Ordovician period, and extending into the Siluarian, the oxygen concentration in the atmosphere rose continuously, extending into the Silurian. The so-called Great Ordovician Biodiversification Event (GOBE), was very likely linked to rising oxygen levels. This was argued because, similarly, the increase in atmospheric oxygen is thought to be a leading cause of the "Cambrian explosion" (Edwards, 2019). During the Permo-Carboniferous times the O_2-concentration in the atmosphere reached its maximum at around 35 vol.% likely caused by the development of large vascular plants and the associated increase in the burial of organic matter (Holland, 2006). This was followed by the Permo-Triassic Mass Extinction (PTME), which is thought to be a big contributor to the ensuing long-term decrease in oxygen levels, due to large scale vegetation loss and the thus limitation on photosynthesis, finally stabilizing at around 25 vol.% during the Late Triassic. After the Cretaceous-Paleogene boundary, the oxygen levels decreased again to today's concentrations of around 20 vol.% (Berner et al., 2003; Mills et al., 2023).

1.2 Iron Formations

Iron formations (IFs) are iron-rich and siliceous marine-chemical sedimentary rocks (see Figure 1.2), which are confined to the Precambrian rock record, and can be found globally. Their Fe- and silica content ranges between 12 and 40 wt.% and from 40 to 60 wt.% respectively. The iron is predominantly mineralized as hematite (Fe_2O_3), martite (a hematite pseudomorph after magnetite) and magnetite (Fe_3O_4). These minerals formed out of Fe(III) oxyhydroxide-silica particles, which first precipitated from the water column onto the seafloor (e.g., Percak-Dennett et al., 2011). Because of the high iron-concentration inside these minerals (Fe ≥56 wt.%) iron formations comprise the principal source of iron for the steel industry. Chert (SiO_2) is the major silica mineral in iron formations, but also Fe-rich silicate minerals, such as stilpnomelane or greenalite can be found. Carbonate minerals, especially Fe-carbonates, such as siderite and ankerite, are also often present in iron formations (Bekker et al., 2014; Konhauser et al., 2017; Mänd et al., 2022).

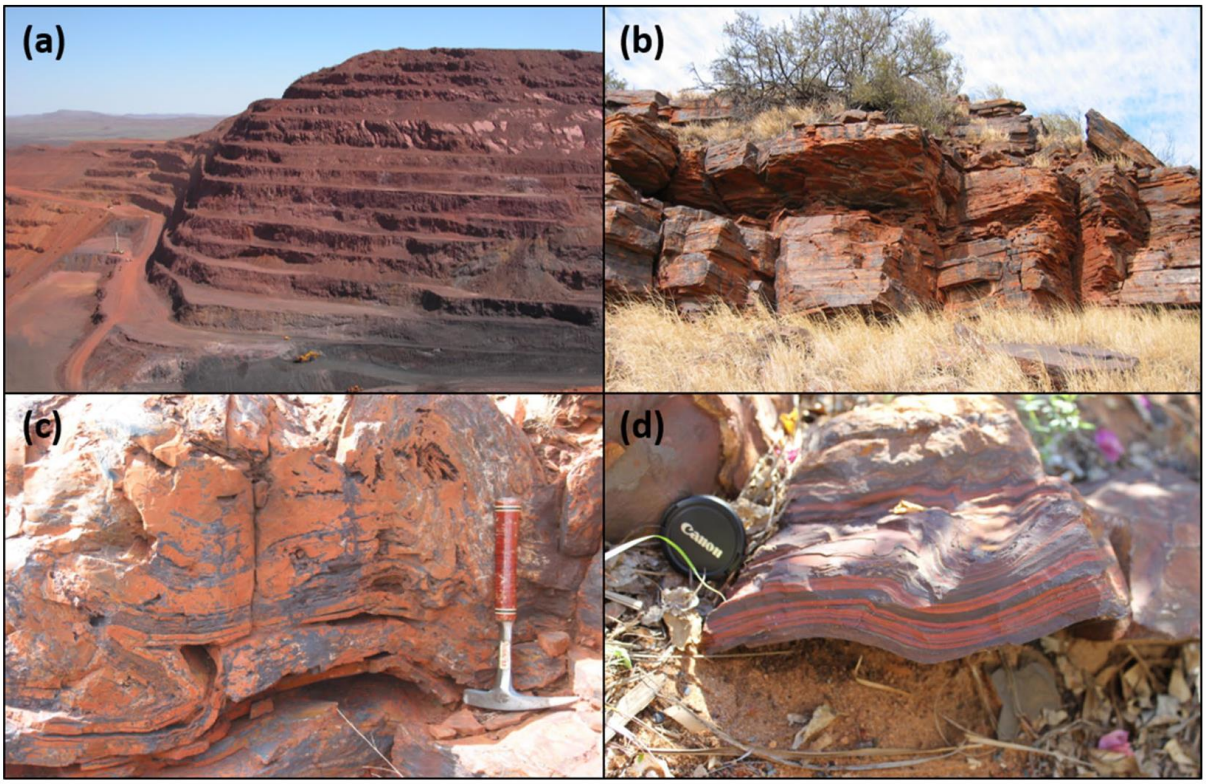

Figure 1.2: *Representative images of Iron Formations: (a) Image of the Tom Price BIF in Western Australia; (b) Image of the BIF in Gamohaan Hill in South Africa (c) Closeup of Gamohaan Hill; (d) hand specimen of the Hamersley Group Banded Iron Formations in Western Australia. Adapted from Dreher et al. (2021, p. 594).*

Iron formations are also of great scientific interest, for being able to constrain the evolution of Precambrian marine environments (Van Hise and Leith, 1911; Trendall, 2002; Bekker et al., 2014; Mänd et al., 2022, and references therein). Understanding

the depositional mechanisms of BIFs has been a widely discussed topic, and a concrete answer has yet to be established. What can be said about the origin of BIFs is that it is generally agreed upon that the minerals in IFs are not primary in origin. They tend to have undergone post-depositional alterations under diagenetic and metamorphic conditions and, in some cases, post-depositional fluid flow. For the deposition of Fe-rich minerals to occur, dissolved Fe^{2+} (ferrous) must oxidize to insoluble Fe^{3+} (ferric). This is thought to have occurred in three ways, (i) via oxygenic photosynthesis by cyanobacteria or their predecessors, (ii) due to anoxygenic photosynthesis (or metabolic oxidation), also referred to as photoferrotrophy, by Fe^{2+}-oxidizing bacteria and (iii) through abiotic photochemical oxidation by UV-light from the sun, which is discussed in more detail in Chapter 1.2.2 (Kappler et al., 2005; Konhauser et al., 2017; Thompson et al., 2019; Bekker and Kovalick, 2021; Mänd et al., 2022).

Based on texture, IFs can be divided into those composed of fine-grained chemically precipitated mud, called micritic iron formations (MIFs), and those IFs that are predominantly composed of granules, called granular iron formations (GIFs). MIFs can often be found in bandings of different scales, from microlamination (millimeter to submillimeter-sized layers) up to macrolamination with meter-thick layers and comprise the so-called banded iron formations (BIFs), which dominate the global occurrences (Figure 1.2 a-d) (Beukes and Gutzmer, 2008; Mänd et al., 2022). GIFs, on the other hand, are made from sand-size grains and are typically cross-bedded. There is another type of IFs based on texture, which is referred to as Rapitan-type IF, which show thin-bedding of fine grained hematite-quartz rock, but is lacking a mesobanding like the BIFs (Klein and Beukes, 1993; Trendall, 2002). They are associated with glacial diamictites and were deposited during the Neoproterozoic (Sturtian and Marinoan) glaciations, with a few small deposits being formed during the Paleoproterozoic and the Mesoarchean (Klein and Beukes, 1993; Klein, 2005; Beukes and Gutzmer, 2008). They can also be differentiated from Algoma- and Superior type based on its difference in mineralogy (Klein and Beukes, 1993).

When looking at the depositional setting, IFs can be subdivided into two types, Algoma and Superior. The Algoma-type is present in association with various volcanic rocks such as submarine mafic-ultramafic and felsic volcanic rocks, but also volcanoclastic greywackes. The bands of the Algoma-type typically show thin bands of ferruginous

grey or jasper chert, hematite, and magnetite. Occasionally carbonate- or sulfide-iron facies are locally present. They likely formed near volcanic arcs apparently under the influence of hydrothermal activity and are of comparably smaller extent (rarely larger than 10 km and typically not >50 m in thickness; Konhauser et al., 2017). Iron formations that formed prior to 3.0 Ga, can be generally described as belonging to the Algoma-type (Gross, 1965; Gross et al., 1980; Konhauser et al., 2017; Mänd et al., 2022). Some examples for Algoma type IFs are the Temagami IF (e.g., Fyon and Cole, 1989) or the IF deposits from the ~2.71 Ga Woodburn Lake greenstone belt (e.g., Barrett et al., 1988; Gourcerol et al., 2016).

The other major type of IFs, the Superior-type, developed on continental-shelf environments near the shore, in association with shelf sediments like carbonates and clastic sediments, and only a minor amount of volcanic rocks. Superior-type IFs are also laterally more extensive (sometimes over 100,000 km^2) in comparison to the Algoma-type IFs (Konhauser et al., 2017). This, however, does not necessarily imply that Algoma-type IFs were always smaller in extent, as most had been deformed by tectonic processes, meaning their original size is likely to be underestimated (Bekker et al., 2014). Known Iron Formations of this type would be the Krivoy Rog BIF (e.g., Belevtsev et al., 1983) or the IFs from the Transvaal Supergroup (e.g., Beukes and Klein, 1990). It should also be noted that a clear distinction between the two types of iron formations is not always possible when talking about the Archean successions, since they are, as mentioned before, often affected by strong deformations. Examples for this distinction problem would be the Dales Gorge Member of the Brockman IF, which has been classified in the past as both Superior- (e.g., Gross et al. 1980) and also Algoma-type (e.g., Dimroth 1976), and the Hamersley Basin, where neither type fits perfectly (Gross, 1965; Gross et al., 1980; Trendall, 2002).

1.2.1 Temporal distributions and dating of IFs

Iron formations appear throughout Earth's history, but, as previously mentioned, are mostly confined to the Precambrian, between the Eoarchean and the Paleoproterozoic. In Figure 1.3 the deposition of IFs in metric tons over Earth's history is depicted, where it is evident that before 2.4 Ga BIFs were dominantly deposited. Age constraints for Archean and Paleoproterozoic IFs are dated using U-Pb and Pb-Pb geochronology by, i.e., whole rock and zircon dating of the IFs directly or of units above or beneath (e.g., Hegner et al., 1984; Alexander et al., 2008; Ndime et al., 2019). In the absence of

suitable layers or samples for U-Pb geochronology, Re-Os geochronology offers an alternative means of constraining depositional ages, either by indirect dating (e.g., Rooney et al., 2014) or by whole rock dating of the IF-layers (e.g., Schulz et al., 2021; Prost et al., 2024). The oldest known IFs, from the Eoarchean (4-0 – 3.6 Ga), are the ~3.8 Ga BIF in the Isua greenstone belt in western Greenland (e.g., Dymek and Klein 1988; Nutman et al. 1997), and the ≥3.75 Ga IF from the Nuvvuagittuq Supracrustal Belt in northern Québec (e.g., Mloszewska et al. 2012). IFs older than 3.0 Gyr are relatively rare, with the reason being not entirely clear, but it could simply represent a preservation bias. Another problem with IFs of this age is that they have often undergone amphibolite- or higher-grade metamorphosis, leading to substantial open system behavior, compromising geochemical and geochronological analyses. An example of a well-preserved Paleoarchean (3.6 Ga – 3.2 Ga) IF is the Tomka BIF in the Singhbhum Craton, India, with an approximated age <~3.51 Gyr, which was calculated from U-Pb SHRIMP dating of zircons in an underlying formation (for more detailed information, see Chapter 2.2; Mukhopadhyay et al., 2008; Mukhopadhyay, 2020). The southern region of this craton has only undergone low-grade metamorphism and is discussed in detail in Chapter 2.2 and onward, as this is the region where the samples of this study were taken from.

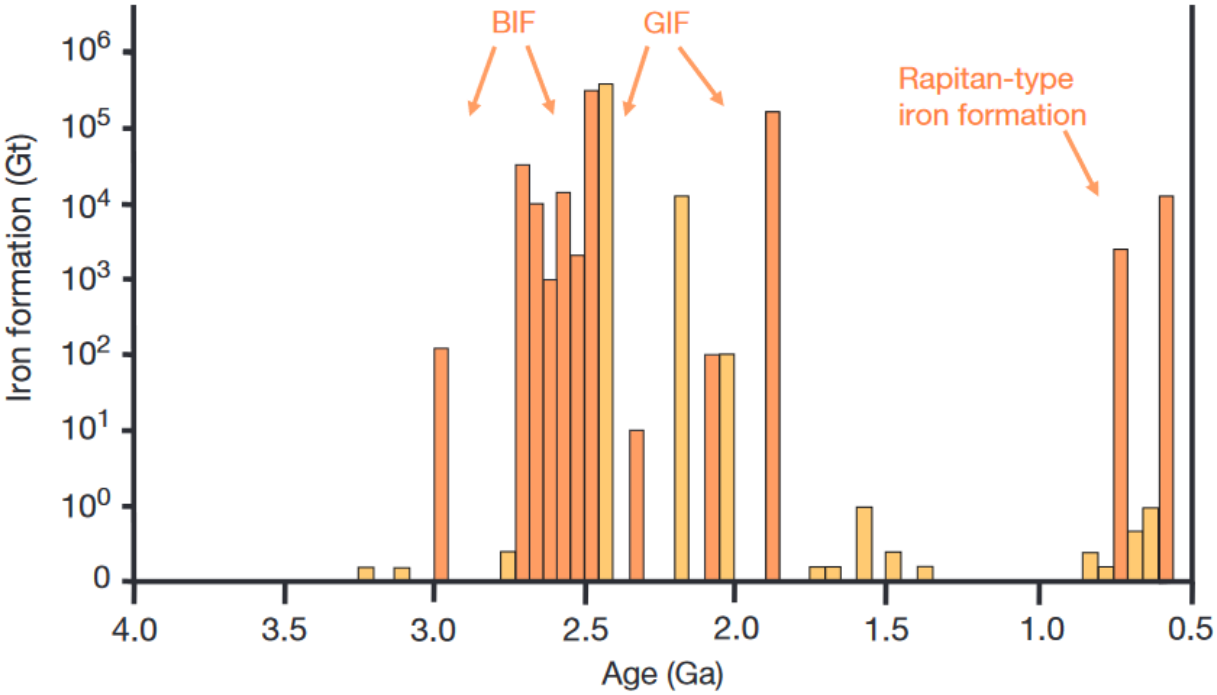

Figure 1.3: *Deposition of iron formations in metric (Giga-) tons over time. The deeper orange color left of the 1.0 Ga mark stands for BIFs and right of it for the Rapitan-type IF. The lighter orange color is for GIF (granular iron formation) deposits (modified after Bekker et al., 2014).*

The Meso- to Neoarchean was characterized by strong cratonization and widespread, mostly submarine, volcanism. IFs during this period, although formed in both depositional types, were mostly of Algoma-type like the BIFs from the Yilgarn block of Western Australia (e.g., Gole 1981). IFs of the Superior-type were scarce, (e.g., IFs in the Witwatersrand and the Pongola Supergroup of South Africa, which is part of the Kaapvaal Craton). Notably, about two thirds of all iron in Precambrian IFs was deposited between 2.6 and 2.4 Ga, including the Hamersley Range (Western Australia), the Transvaal Supergroup (South Africa) and the Lake Superior Region (USA) (Trendall, 2002; Klein, 2005; Bekker et al., 2014).

From the end of the Paleoproterozoic (~1.8 Ga) onwards until the beginning of the Neoproterozoic (~0.75 Ga) no major IFs were deposited ("boring billion"). Following this abrupt decline of (B)IF deposition, they reappeared during the Neoproterozoic as Rapitan-type IF, associated with glacial deposits. For these younger IFs, U-Pb geochronology is also used (e.g., Klein and Beukes, 1993; Hoffmann et al., 1996; Basta et al., 2011), but in some cases $^{40}Ar/^{39}Ar$ is also used (e.g., Piacentini et al., 2013). Prominent examples for such iron formations can be found in the Urucum Region, Brazil (Gaskiers glaciation; Dorr II, 1945), the eponymous Rapitan Group, Canada (Sturtian glaciation; Helmstaedt et al., 1979; Macdonald et al., 2010) (Klein and Beukes, 1993; Klein, 2005; Cox et al., 2013). With the beginning of the Phanerozoic, iron formations disappeared completely from the geologic record (Konhauser et al., 2017).

A possible time constraint for IFs, which should be discussed, is the possible banding of IFs. The processes governing the formation and timing of the deposition of these bandings remain poorly understood and may vary between years to hundreds of thousands of years (e.g., Li, 2014; Lantink et al., 2019, 2022; Schad et al., 2019). Li (2014), for example, proposed that nanobands, which are within the nanometer scale, indicate diurnal cyclicity caused by the circadian metabolism of microorganisms, and that microbands, which are on a sub-millimeter scale, cycle on an annual basis. In another approach, De Oliveira Carvalho Rodrigues et al. (2019) argues for orbital eccentricity (Milankovitch forcing) as a cause of the banding, yielding accumulation rates of approximately 1-2 cm/kyr for macrobands. Similarly, Lantink et al. (2019) calculated an accumulation rate of multiples of 100 kyr for meter-thick bands, by linking the banding to Milankovitch forcing. Presenting a new model, Herwartz and Viehmann (2024) linked the periodical layering of Si-rich and Fe-rich bands with changes in water

turbidity. This regulates light penetration of the ocean water and thus the depth of Fe^{2+} oxidation by photoferrotrophs.

1.2.2 Formation mechanisms for (Banded-) Iron Formations

The iron source that led to IF precipitation has been a widely debated topic for several decades (Holland, 1973; Konhauser et al., 2017). Holland (1973, 1984) calculated that if the iron was carried to the IF depositional sites as dissolved (i.e., Fe^{2+}) riverine load, in case of the Hamersley Basin (Western Australia), several rivers the size of the Amazon River would be needed to account for the amount of iron precipitated. This, however, is very unlikely. Moreover, iron formations usually have minimal to no detrital contributions, i.e., no riverine input of terrigenous material to the oceans, which also argues against the hypothesis of a riverine source of the iron (Holland, 1973, 1984; Konhauser et al., 2017). Volcanic gases are also an unlikely source of iron in IFs, for reasons similar to those that discount dissolved riverine input. To be able to supply enough iron to account for deposits the size of those in the Hamersley Basin, it would require emissions from a thousand of volcanoes (given a rate of 35-50 tons of iron released per year; Holland, 1973). Currently, the most accepted hypothesis for the source of iron in Precambrian IFs are deep-sea hydrothermal vent systems (Bekker et al., 2010, and references therein). This could also by itself explain the characteristic mesobanding of BIFs, dictated by intervals of enhanced hydrothermal activity, leading to iron-rich mesobands, and low hydrothermal output, which, in turn, led to periods of the deposition of interbedded chert (Isley, 1995; Trendall, 2002; Rasmussen et al., 2013; Li et al., 2015; Dodd et al., 2022). The deposition of Neoproterozoic BIF, by constrast, is associated with glacial sediments, as evidenced by the presence of dropstones and diamictites within these BIFs, and is inferred to reflect the return to Archean-like ferruginous and anoxic basin conditions (Canfield et al., 2008; Cox et al., 2013; Gaucher et al., 2015).

Many questions about the genesis of IFs are still uncertain, among other things, because of a lack of modern analogues. In any case, for iron formations to form, insoluble Fe^{3+} (Fe^{3+} is insoluble in water even in trace amounts if less than 1 µmol of oxygen is present; Bekker et al., 2010; Bekker and Kovalick, 2021) must precipitate after soluble Fe^{2+} was transported to the depositional site followed by oxidation. As mentioned above in Chapter 1.2, three possible main ways of oxidation have been

proposed. These processes are illustrated in Figure 1.4 and are briefly discussed below. An extensive amount of literature exists on this subject, which mostly has in common the use of non-traditional stable isotopes (e.g., iron) as an ideal tool to disentangle the different oxidation paths in Fig. 1.4. However, a detailed description is beyond the scope of this work and the reader is referred to the literature (see Bekker et al., 2014, and references therein for a detailed review).

The oxidation method via UV-light (A in Figure 1.4) could have been a possibility in the period before the rise of atmospheric oxygen, as there would not have been an ozone layer protecting against the high amounts of ultraviolet light reaching the Earth's surface (Cairns-Smith, 1978; Braterman et al., 1983; Anbar and Holland, 1992). However, Konhauser et al. (2007) experimentally found that the effect of UV oxidation of Fe^{2+} is rather insignificant in ocean waters saturated with ferrous iron phases.

Iron oxidation via metabolic microbial mechanisms (B in Figure 1.4) is believed to be the main contributor for iron oxidation for IF deposition prior to ~2.4 Ga (Bekker et al., 2010, 2014). The process can be differentiated into two main pathways: anoxygenic photosynthesis (photoferrotrophy) and microaerophilic bacteria (Bekker et al., 2010, 2014; Konhauser et al., 2017). While photoferrotrophy works with bacteria (photoferrotrophs) that use Fe^{2+} as an electron donor instead of H_2O, producing Fe^{3+} (Hartman, 1984; Bekker et al., 2014; Konhauser et al., 2017), Fe^{2+} oxidation via microaeophilic bacteria works using Fe^{2+} as an electron donor (producing iron hydroxides), oxygen as the electron acceptor, and CO_2 to convert the oxygen into organic carbon (Bekker et al., 2010, 2014; Konhauser et al., 2017). Notably, in today's oceans microaeophilic bacteria are a dominant way for Fe^{2+} oxidation in the vicinity of deep sea hydrothermal vent systems (Søgaard et al., 2000; Emerson and Moyer, 2002).

Another way of iron oxidation is by cyanobacteria producing O_2 (C in Figure 1.4). In the absence of any eukaryotic fossil record before ~1.9 Ga, Cyanobacteria must have been the first important and primary producers of oxygen utilizing photosynthesis in the Archean oceans (Han and Runnegar, 1992; Knoll et al., 2006; Bekker et al., 2014).

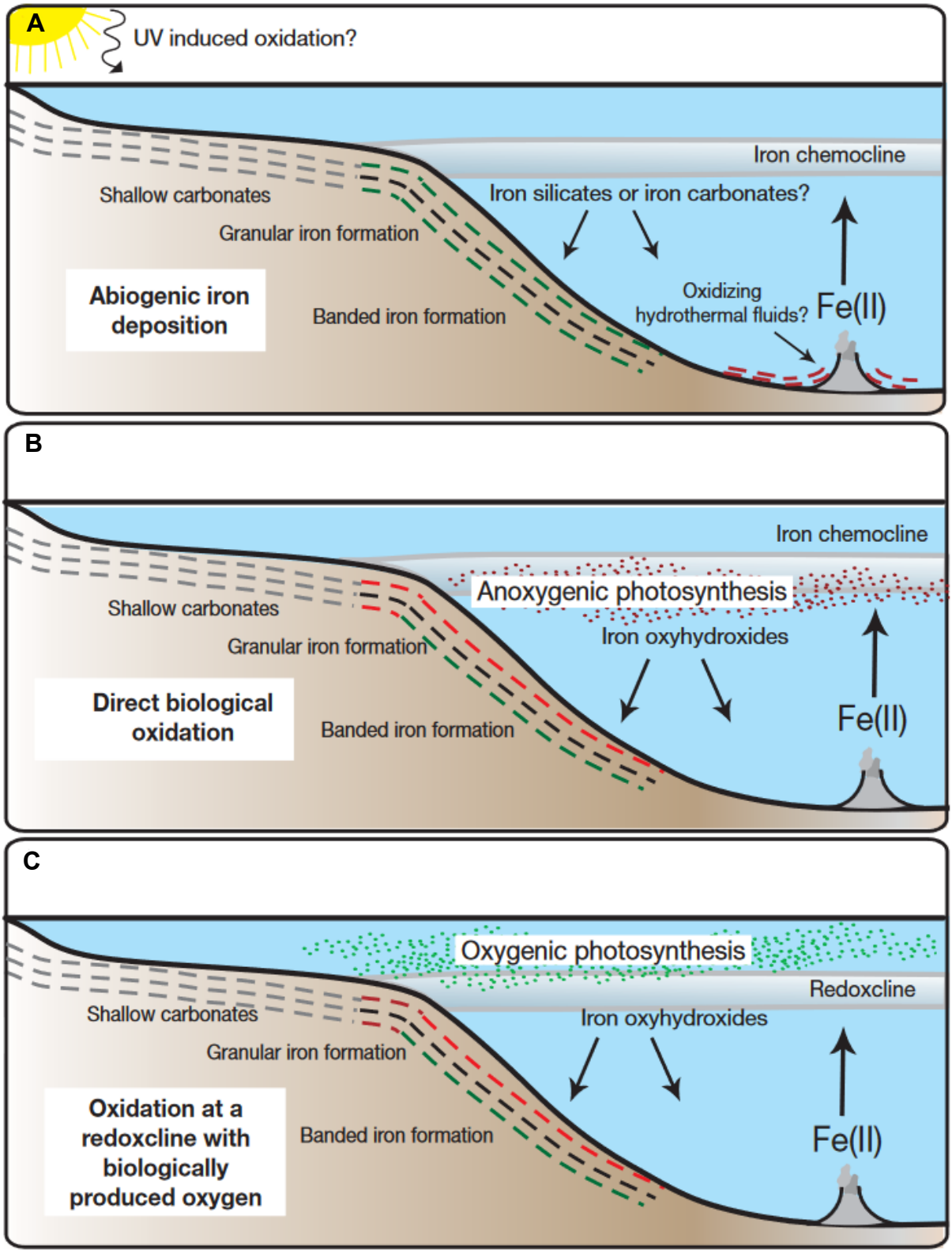

Figure 1.4: *Simplified model illustrating mechanisms of iron oxidation and IF deposition. A: Iron oxidation via UV-light; B: Iron oxidation via metabolic, specifically anoxygenic, photosynthesis (photoferrotrophy); C: Iron oxidation via biologically produced O_2 (cyanobacteria) (modified after Bekker et al., 2010).*

1.2.3 BIFs as proxies for ancient seawater

Iron formations are prominent candidates for examining the composition and chemical evolution of ancient oceans, since their precursor minerals, either directly precipitated from seawater, or formed by interaction with it. It can thus be assumed, that these minerals preserve the marine chemical signature of the time they precipitated (Bekker et al., 2014). Additionally, iron formations are observed to generally have low concentrations of crustal-sourced and immobile elements such as Al (in the form of Al_2O_3), Ti, Zr, Th etc., which indicates an authigenic origin (i.e., precipitated directly from seawater at the site of deposition) and the preservation of the original geochemical signatures. However, contaminations in the form of syn-depositional (i.e., clastic detritus like aluminosilicates) or post-depositional alterations through diagenesis or a metamorphic overprint, could alter the geochemistry of these marine sediments and thus would not provide accurate information about the initial seawater signal. It is thus important to study IFs for increased concentrations of such crustal-derived elements to rule out any syn- and/or post-depositional alterations (see Chapter 5.1) (Bau, 1993; Viehmann et al., 2015a, 2016; Bekker and Kovalick, 2021).

Rare earth elements (REEs), which are the focus of in this chapter, and other (trace) elements, such as phosphorous (P), nickel (Ni), chromium (Cr), and manganese (Mn) have been commonly used as a geochemical tool to decipher the pristine nature of IF samples (i.e., do they represent the seawater signal from which they precipitated?) (Bau and Dulski, 1996; Bolhar et al., 2004; Robbins et al., 2016; Konhauser et al., 2017). In general, the REEs and yttrium (REY for short) are a group of elements also called lanthanides (atomic numbers 57-70), which occur exclusively in a trivalent oxidation state, except – and importantly - for Ce and Eu. The latter two elements, because of their redox sensitivity, may have oxidation states of +4, in the case of Ce under oxidizing conditions, and +2 for Eu in reducing conditions at high temperatures, respectively. Yttrium is often included when talking about REEs, because of its similar atomic radius as some of the rare earth elements and its oxidation state of +3 (Bau, 1996; Linnen et al., 2014), making it a geochemical twin to some REEs. The use of REEs, or more specifically REY, in investigating IFs serves two primary purposes: First and foremost, to utilize the redox-sensitive properties of REEs and yttrium to uncover the oxidation- and deposition mechanisms in IFs. Second, for tracing possible sources of the iron in IFs due to characteristic concentration patterns of REYs in, e.g., hydrothermal fluids, allowing for direct comparison with REY signatures in IFs

(Klinkhammer et al., 1983; Derry and Jacobsen, 1990; Alexander et al., 2008; Bekker et al., 2014). For such interpretations, the studied rocks must represent a reliable archive of the seawater composition. For this, the REYs are also used as a tracers for syn- and post-depositional alterations, due to the dependence of the REY composition on the source (e.g., hydrothermal, continental, etc.) and environment (e.g., pH, salinity, etc.) during deposition (Viehmann et al., 2015a, 2016).

Previous studies on IFs, such as on the Urucum BIF (e.g., Viehmann et al., 2016) and the Tomka BIF (the topic of this study, e.g., Kienle, 2024), demonstrated the reliability of using the REYs as a proxy for the marine seawater composition. Both studies first looked at the concentrations of such crustal-sourced, immobile elements (e.g., Al, Zr, Hf, etc.) to check the purity of the samples. For the Tomka BIF, immobile element concentrations such as Th and Hf were extremely low (<0.09 ppm) and in some cases even below the limit of detection. Zirconium had slightly elevated concentrations compared to Th and Hf (0.13-2.84 ppm), but, in summary, most samples of the Tomka BIF can be described as pure (Kienle, 2024). In comparison, the samples from the Urucum BIF contain elevated concentrations of Th (0.06-4.64 ppm) and Hf (0.02-1.87 ppm) and strongly elevated values of Zr (1.98-85.0 ppm) indicating partially impure samples (Viehmann et al., 2016). To (further) distinguish between the pure and the impure samples, REY patterns were analyzed for characteristic features of modern seawater, including positive La and Gd anomalies, negative Ce anomalies (for further information see De Baar et al., 1985; Bau, 1996, 1999, and references therein). Patterns that are sub-parallel to those of modern seawater indicate chemical purity, as observed in the Tomka BIF (Kienle, 2024) and in some samples from the Urucum BIF. Although Tomka BIF is considered pure for the REY and HFSE systems (Kienle, 2024), this is not directly transferable for the HSE concentrations and Re-Os isotopic system, which is the topic of the following chapter.

1.3 Highly siderophile elements

The six platinum-group elements, Os, Ir, Ru, Pt, Rh, and Pd, together with Re, and Au are termed highly siderophile elements (HSEs). The HSEs are defined by their strong affinity towards metallic phases, relative to silicates (Walker, 2009; Brenan et al., 2016). Because of this affinity, one would expect that the HSEs in the Earth's mantle would be effectively depleted, due to the partitioning of these elements into the core. However, the mantle concentrations of HSEs are only about 150 to 200 times lower

compared to chondritic meteorites, higher than assumed by their (experimentally derived) partition coefficients between mantle and silicate (Becker et al., 2006; Walker, 2009). To facilitate comparisons between the different reservoirs, the concentration of selected HSEs in CI chondrites, the primitive upper mantle (PUM) and the upper continental crust (UCC) are as follows: For CI chondrites: Re (~41.0 ppb), Os (~491 ppb), Ir (~462 ppb) and Pt (~943 ppb) (Fischer-Gödde et al., 2010); for the PUM: Re (~0.35 ppb), Os (~3.90 ppb), Ir (~3.50 ppb) and Pt (~7.60 ppb) (Becker et al., 2006); for the UCC: Re (~0.20 ppb), Os (~0.03 ppb), Ir (~0.02) and Pt (~0.51 ppb) (Peucker-Ehrenbrink and Jahn, 2001). To obtain representative data of the UCC average, Peucker-Ehrenbrink and Jahn (2001) utilized loess samples as a proxy for the upper continental crust, due to it originating from the erosion of continental rocks.

In conjunction with broadly chondritic interelement HSE ratios in the mantle, this gave rise to the hypothesis of a late accretion component of chondritic material to the Earth, the so called “Late Veneer Hypothesis”, contributing about ~0.5% of the total material of the Earth after core formation (Walker, 2009; Fischer-Gödde and Kleine, 2017). It was first proposed by Kimura et al. (1974) and Chou (1978) that such a process may have occurred after core formation and the Moon-forming impact, and is thought to have consisted of a mixture of meteoritic matter, likely including between 5-20% of suprachondritic iron meteorite-like material (Fischer-Gödde and Becker, 2012; Palme and O’Neill, 2014).

Besides the wide usage of HSEs in the field of cosmo- and geochemistry, including, for example, planetary differentiation (i.e., core formation) and mantle differentiation processes (as briefly discussed above) (e.g., Walker, 2009, and references therein), the formation of the continental lithosphere (e.g., Peucker-Ehrenbrink and Jahn, 2001) and as markers for the identification of meteoric signatures in impact melt rocks (e.g., Koeberl, 2014, and references therein), which cannot be reviewed here in detail. Two aspects that are important for this study need to be explained in more detail: (i) the ^{187}Re-^{187}Os decay system that comprises only HSE elements, and (ii) the marine HSE and Os isotope record.

1.4 ^{187}Re-^{187}Os isotopic system:

1.4.1 Overview of the Re-Os isotopic system and its applicability

Rhenium, atomic number 75, has two naturally occurring isotopes: ^{185}Re (37.40%) which is stable, and ^{187}Re (62.60%) (abundances from Audi et al., 2003), which decays via β^- decay into ^{187}Os with a half-life of 4.15 x 10^{10} years, as determined by Selby et al. (2007). Osmium, atomic number 76, has seven naturally occurring isotopes, of which five are presumably stable: ^{184}Os (0.02%), which decays via α-decay into ^{180}W (half-life 1.12 x 10^{13} yr; Peters et al., 2014), ^{186}Os (1.59%), which also decays via α-decay into ^{182}W with an half-life of 2.0 x 10^{15} yr, the five stable isotopes ^{187}Os (1.96%), ^{188}Os (13.24%), ^{189}Os (16.15%), ^{190}Os (26.26%) and ^{192}Os (40.78%) (abundances from Audi et al., 2003). Two osmium isotopes are radiogenic in nature, ^{187}Os, as already mentioned, is the daughter isotope of ^{187}Re, and ^{186}Os is the product of an α-decay of ^{190}Pt with a half-life of 4.97 x 10^{11} yr (Braun et al., 2017). Both systems are used in geochemical studies, the ^{190}Pt-^{186}Os system being mostly limited to applications in ore systems (Norman, 2023). However, the ^{187}Re-^{187}Os system has seen far more and wider applications, due to its capabilities as a geochronometer (e.g., Hannah and Stein, 2012; Walker, 2015, and references therein) as well as a tracer for the reconstruction of the seawater record (e.g., Peucker-Ehrenbrink and Ravizza, 2000, 2020, and references therein).

During partial melting, Os remains highly compatible, whereas Re behaves more incompatible. This difference in behavior leads to the enrichment of Re in partial melts and thus extremely variable Re/Os ratios in the crust (Walker, 2015; Peucker-Ehrenbrink and Ravizza, 2020). Via radiogenic ingrowth, the variability in Re/Os ratios, over time, leads to a huge variability in ^{187}Os/^{188}Os ratios, ranging from ~0.13 in the mantle (Meisel et al., 2001) to average crustal values of ~1.4 (Peucker-Ehrenbrink and Jahn, 2001). The contrast between the less radiogenic mantle (with its near chondritic signature; ~0.13; Fischer-Gödde et al., 2010) and the radiogenic crustal values makes this system a suitable source marker in magmatic and marine systems (see Rooney et al., 2024, for a recent review). Besides being a source tracer, the Re-Os radionuclide system can be applied as a geochronometer. Figure 1.5 illustrates a generalized and simplified isochron diagram for the Re-Os system. The x-axis represents the ^{187}Re/^{188}Os ratio, while the y-axis represents the ^{187}Os/^{188}Os ratio. At the initial time (t=0), all samples share a certain, but unknown, initial ^{187}Os/^{188}Os$_{(i)}$ ratio.

Over time, ^{187}Re undergoes radioactive decay to ^{187}Os, increasing the $^{187}Os/^{188}Os$ ratio in proportion to the $^{187}Re/^{188}Os$ ratio of the samples (e.g., minerals). The variable radiogenic ^{187}Os ingrowth – in an isotopically closed system – leads to a linear relationship, following a linear equation, as illustrated in Figure 1.5. On the left side of the equation is the measured $^{187}Os/^{188}Os$ ratio. The right side includes the initial $^{187}Os/^{188}Os$ ratio, the measured $^{187}Re/^{188}Os$ ratio, and an exponential term containing the decay constant and the sample's unknown age t. Because the equation is linear, the initial $^{187}Os/^{188}Os$ ratio can be determined as the y-intercept of the best-fit line through the data points. Once this value is known, the age of the sample can be calculated, by solving the equation. There are many possibilities for an elevated error in the data, such as uncertainties for sample weighing, spike calibrations (the isotope dilution technique is briefly described in Appendix A1), the mass spectrometric measurement statistics and blank correction calculations (see method section) (Stein, 2014).

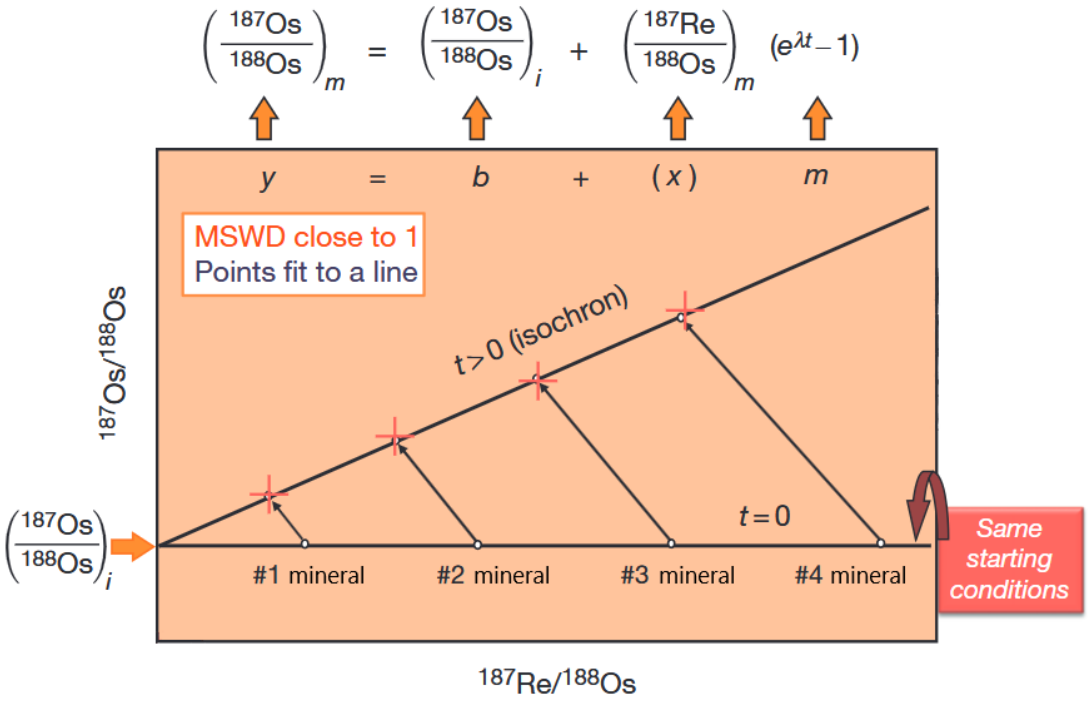

Figure 1.5: *Schematic illustration of the Re-Os isochron dating method. Each mineral sample are assumed to share the same starting conditions and deposition time. After some time t>0 an amount of ^{187}Re decayed into ^{187}Os, shifting the points from the starting line t=0 up and to the left. The linear regression of these points, which behave according to the decay function on the top, can then be used to receive the $^{187}Os/^{188}Os$ initial and the age of the sampled rock (modified after Stein, 2014).*

1.4.2 The marine HSE and ^{187}Os record

Concentrations of the highly siderophile elements in the seawater are exceptionally low compared to those of the upper continental crust (UCC). Rhenium, for example, has a concentration of ~7 ppt in seawater, Os a concentration of ~0.01 ppt (Stein and Hannah, 2014), Ir of only about ~0.003 ppt (Li et al., 2007), and the Pt content varies between 0.039 ppt and 0.896 ppt (Mashio et al., 2017; Liu et al., 2018).
HSEs occur in different phases in seawater. For example, Re is present as an oxyanion, ReO_4^- (Anbar et al., 1992), similar to Os, which (in the oxidized state of +8) occurs as either $H_2OsO_5^0$ or $H_3OsO_6^-$ (Mashio et al., 2017). The species in which Ir can be found in seawater is not entirely clear, but is thought to be in the form of the hydrolysis species $Ir(OH)_3^0$ (Bruland et al., 2014), while Pt occurs as $PtCl_5(OH)^{-2}$ (Mashio et al., 2017). Highly siderophile elements might be delivered to the oceans (in the direction of lesser significance; Peucker-Ehrenbrink and Ravizza, 2000) via (i) continents as detrital- or dissolved (riverine) input, (ii) aeolian or (to a lesser extent) via cosmic dust, or (iii) via deep sea hydrothermal vent systems (Peucker-Ehrenbrink and Ravizza, 1996; Hannah and Stein, 2012; Mashio et al., 2017, and references therein). However, deep sea hydrothermal vent systems, while playing only a minor role for most HSEs (because of local precipitation), are significant contributors for Os. Osmium rapidly oxidizes to highly soluble species, enabling its widespread distribution in the oceans up to the photic zone (Ravizza and Turekian, 1989; Peucker-Ehrenbrink and Ravizza, 2000).

The Re-Os isotopic system is used as a powerful tracer for reconstructing the geochemical evolution of Earth's oceans and being able to track large-scale environmental changes through time. This is due to the (previously mentioned) contrasting geochemical behavior of Re and Os and the redox sensitivity of these elements (Peucker-Ehrenbrink and Ravizza, 2000). Under oxidizing conditions both Re and Os are mobilized, while behaving insoluble under reducing (anoxic or euxinic) conditions. This, in turn, means that for Re and Os can be transported into the oceans by means of chemical weathering, an oxygenated atmosphere was necessary (Hannah and Stein, 2012; Stein and Hannah, 2014). Adding to the useful properties of Os isotopes as tracers for the oceanic chemistry is the short residence time of Os in seawater between 20.000 – 50.000 yr, compared to the long residence time of Re (~750 kyr; Colodner et al., 1993), which gives it the ability to track short-term changes

in the composition of seawater (seawater mixing times are ~1000 yr; Liu et al., 2024) (Hannah and Stein, 2012; Rooney et al., 2024).

The present day $^{187}Os/^{188}Os$ ratio of the modern seawater has a comparably radiogenic value of ~1.06 (compared to the $^{187}Os/^{188}Os$ ratio of a CI chondrite: ~0.126; Fischer-Gödde et al., 2010) (Peucker-Ehrenbrink and Ravizza, 2000). This value results from the different radiogenic sources, like aeolian dust, and the input from rivers, and unradiogenic sources, such as cosmic dust or input from hydrothermal vent systems (see Figure 1.6).

A comparably radiogenic $^{187}Os/^{188}Os$ ratio can be added to the seawater by riverine sources with a global average of around 1.4, with locally significantly higher values (Peucker-Ehrenbrink and Ravizza, 2000). Possible explanations for differences in local riverine $^{187}Os/^{188}Os$ ratios are differences in the lithology of the eroded continental material and preferential weathering of organic-rich sediments, like black shales (Peucker-Ehrenbrink and Hannigan, 2000; Peucker-Ehrenbrink and Ravizza, 2000). These sedimentary rocks, with a high content of organic carbon, are highly enriched in Re and Os, due to their ability to efficiently incorporate trace elements, including platinum group elements such as Re and Os, from the seawater (Peucker-Ehrenbrink

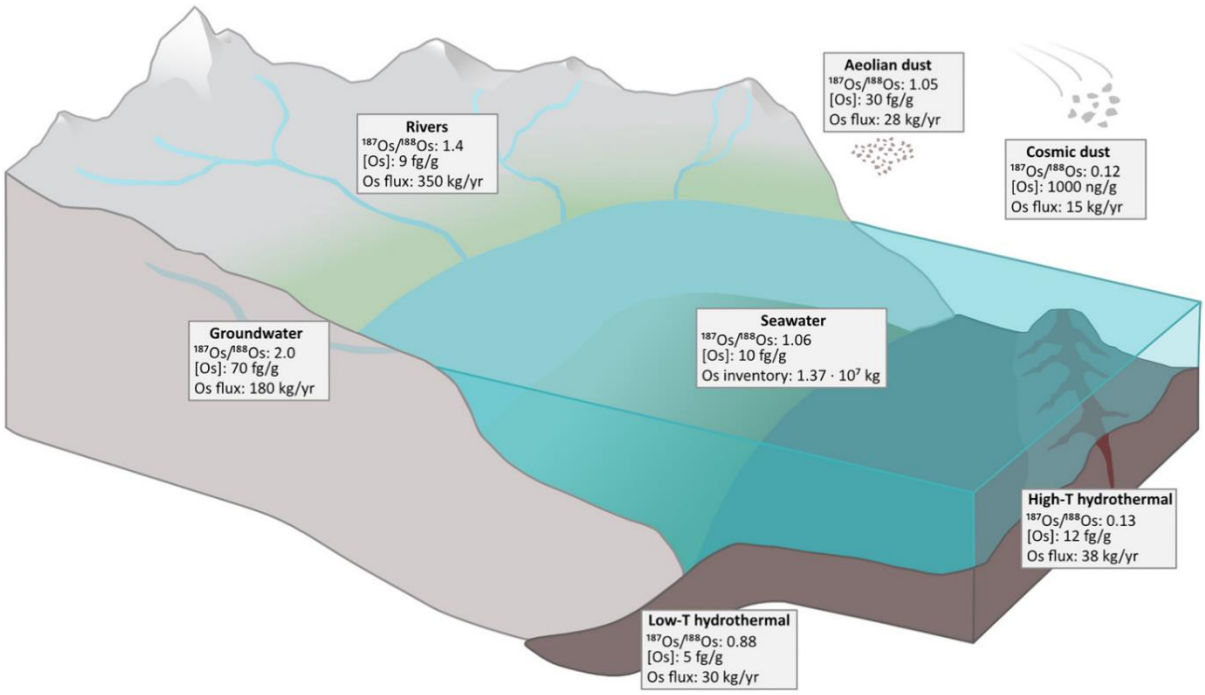

Figure 1.6: *Overview of the main Re and Os sources and reservoirs for seawater. Modern seawater is radiogenic in nature with a similar $^{187}Os/^{188}Os$ ratio to aeolian dust, but a less radiogenic value compared to the riverine input. Notably, it is rather difficult to assume a global average due to the dependency of the riverine Re and Os concentrations on the composition of the bedrock and weathered material (modified after Rooney et al., 2024).*

and Hannigan, 2000; Peucker-Ehrenbrink and Ravizza, 2000). This leads to a very radiogenic signature of ~1.6-3.0 (Pierson-Wickmann et al., 2000; Charbonnier et al., 2022) over time. Weathering of these rocks leads to a significant loss in the Os budget (45% - 90 wt.%; Peucker-Ehrenbrink and Hannigan, 2000), which, in turn, raises the radiogenic Os budget of riverine systems and contributes around 350 kg/yr of Os to the oceans (Peucker-Ehrenbrink and Ravizza, 2000).

Another potentially big contributor to the marine Os budget could be the input from groundwater, but only a limited dataset is available. Paul et al. (2010) studied the groundwater from the Bengal plain which has a $^{187}Os/^{188}Os$ ratio of 2.0 on average. If the ~0.07 ppt of Os could be a representation of the Os concentration in groundwater worldwide, it would add roughly 180 kg/yr of Os. For the radiogenic $^{187}Os/^{188}Os$ ratio of groundwaters a correlation can be observed, between the Os isotopic ratio of groundwaters and those of the sediments which are transported by the rivers which predominantly influence that area (Paul et al., 2010). A similar problem emerges for the input of aeolian dust into the Os seawater budget. Based on the limited data, it is thought to record a upper continental crust like $^{187}Os/^{188}Os$ ratio of ~1.05 (Peucker-Ehrenbrink and Ravizza, 2000) with an annual contribution to the Os seawater inventory of ~28 kg (Rooney et al., 2024).

The aforementioned radiogenic contributors to the marine $^{187}Os/^{188}Os$ budget have a, on average, higher $^{187}Os/^{188}Os$ ratio than the modern seawater (~1.06; Peucker-Ehrenbrink and Ravizza, 2000). However, a source of significantly less radiogenic $^{187}Os/^{188}Os$ are deep-sea hydrothermal vent systems, which typically contribute mantle-like HSE and ^{187}Os signatures to the seawater. The influence of these deep-sea vent systems on the global ^{187}Os seawater budget might have changed over time. A possible reason for this are changes in the mantle convection activities, that, when enhanced, lead to increased activity of deep-sea hydrothermal vent systems, in turn introducing larger amounts of less radiogenic, mantle-derived osmium (with low $^{187}Os/^{188}Os$ between 0.13-0.88, depending on the temperature; Sharma et al., 2007; Lu et al., 2017) into seawater, thereby lowering the marine osmium isotope ratio (Peucker-Ehrenbrink and Ravizza, 2000; German and Seyfried, 2014). The contribution of hydrothermal systems to the $^{187}Os/^{188}Os$ ratio of the seawater is of minor nature, as these systems – depending on temperature – typically depict a rather low flux of Os 30-38 kg/yr to the seawater (Rooney et al., 2024, and references therein).

This is possibly because of the tendency of Os to get sequestered into sulfide minerals which are forming in the hydrothermal vents and around on the seafloor (Syverson et al., 2021). However, due to possible differences in the seawater chemistry, the impact of high-temperature hydrothermal vents for the seawater could have been greater in the past (Katchinoff et al., 2021).

Extraterrestrial matter mostly has a chondritic $^{187}Os/^{188}Os$ of 0.12 (Fischer-Gödde et al., 2010), which was probably constant throughout Earth's history.

Contributions of extraterrestrial matter to the seawater osmium isotope budget can occur via two pathways: (i) the continuous influx of cosmic dust and (ii) episodic impact events. As the annual constant Os flux of cosmic dust is <15 kg/yr (Peucker-Ehrenbrink and Ravizza, 2000), it does not meaningfully alter the marine $^{187}Os/^{188}Os$ ratio. Impact events on the other hand can cause spikes in the seawater osmium isotope signature due to the high osmium concentration (~491 ppb; Fischer-Gödde et al., 2010). Such marine Os isotopic spikes in Earth's history are discussed later on in this chapter.

By using the method described in Chapter 1.4.1 of calculating the $^{187}Os/^{188}Os_{(i)}$ and known age data, an osmium seawater evolution curve (see Figure 1.7 and 1.8) can be

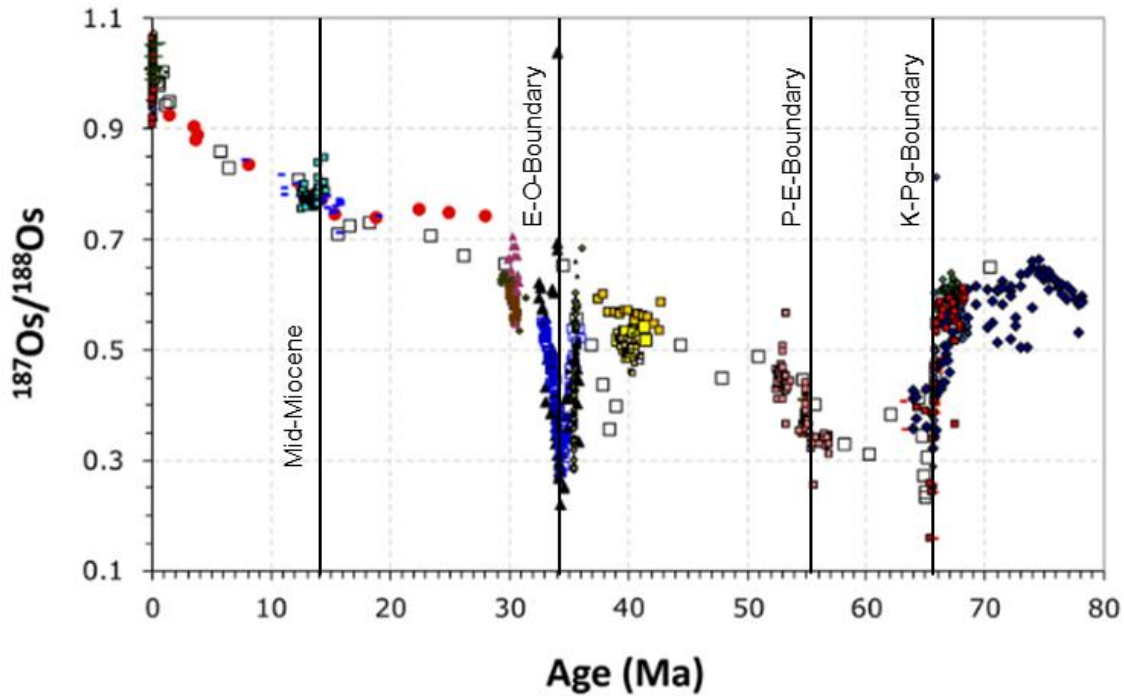

Figure 1.7: *Seawater $^{187}Os/^{188}Os$ evolution curve of the past 80 Ma. Four excursions of the Os isotope ratio can be observed: The Cretaceous-Paleogene-Boundary (linked to Deccan volcanism and the Chicxulub impact event), the Paleocene-Eocene-Boundary (likely caused by the Paleocene-Eocene Thermal Maximum PETM), the late Eocene (Popigai and other impact events) and one in the Mid-Miocene (proposed cause is the Middle Miocene Climatic Optimum MMCO) (modified after Peucker-Ehrenbrink and Ravizza, 2020).*

plotted. Even though the short residence time of osmium in seawater (~20 to 50 yr; Rooney et al., 2024) makes it quite susceptible to short-term excursions (e.g., impact events), it can still reflect long-term trends (Rooney et al., 2024). In Figure 1.7, a seawater $^{187}Os/^{188}Os$ curve of the past 80 Myr can be observed, where four excursions can be differentiated. The first of those is the Cretaceous-Paleogene boundary, which marks the beginning of the Cenozoic and an excursion of the seawater $^{187}Os/^{188}Os$ ratio from a more radiogenic value of ~0.60 to a near-chondritic and unradiogenic value of ~0.15 (see Figure 1.8) (Ravizza and Peucker-Ehrenbrink, 2003; Peucker-Ehrenbrink and Ravizza, 2020). This shift is thought to be linked to both Deccan volcanism and the Chicxulub impact event, where it was noted by Robinson et al. (2009) that the weathering of the Deccan flood basalts ($^{187}Os/^{188}Os_{(i)}$: ~0.129; calculated by Allègre et al., 1999) initially decreased the seawater osmium isotope ratio over a span of ~200 kyr and then stabilized at a $^{187}Os/^{188}Os$ ratio of ~0.4. After this stabilization the Os ratio plummeted towards a chondritic value, which can be explained by the Cretaceous-Paleogene impact event (Chicxulub), due to its aforementioned high Os concentration and the chondritic $^{187}Os/^{188}Os$ (Ravizza and Peucker-Ehrenbrink, 2003; Robinson et al., 2009; Rooney et al., 2024). Another example for a strong negative excursion from the trend of a steadily more radiogenic sweater osmium isotope ratio occurred in the late Eocene, where the $^{187}Os/^{188}Os$ ratio shifted towards a chondritic-like value, interpreted to be caused by another episodic impact event, the Popigai impact, which, however, was only one of several around this time (Paquay et al., 2014).

Until the Cretaceous-Paleogene border, marking the beginning of the Cenozoic, much work focused on analyzing pelagic carbonate sequences. When looking back in time even further, pelagic carbonates are becoming more rare throughout the Mesozoic until they are essentially missing from the geological record before the Paleozoic-Mesozoic boundary (Peucker-Ehrenbrink and Ravizza, 2012, and references therein). This led to the predominant use of organic-rich mudrocks (ORM) to further reconstruct the evolution of the $^{187}Os/^{188}Os$ in seawater (see Peucker-Ehrenbrink and Ravizza, 2020, and references therein), and more recently, to the application of banded iron formations for this purpose (e.g., Schulz et al., 2021; Prost et al., 2024, and this study). Organic-rich mudrocks (e.g., black shales) are useful for studying the marine Os isotope curve, due to their elevated concentrations of platinum group elements, such as osmium. A potential problem, when studying ORMs for their osmium isotopy, is a potential

contamination from nonhydrogenous (i.e., not seawater-derived) matter such as detrital material (Cohen et al., 1999).

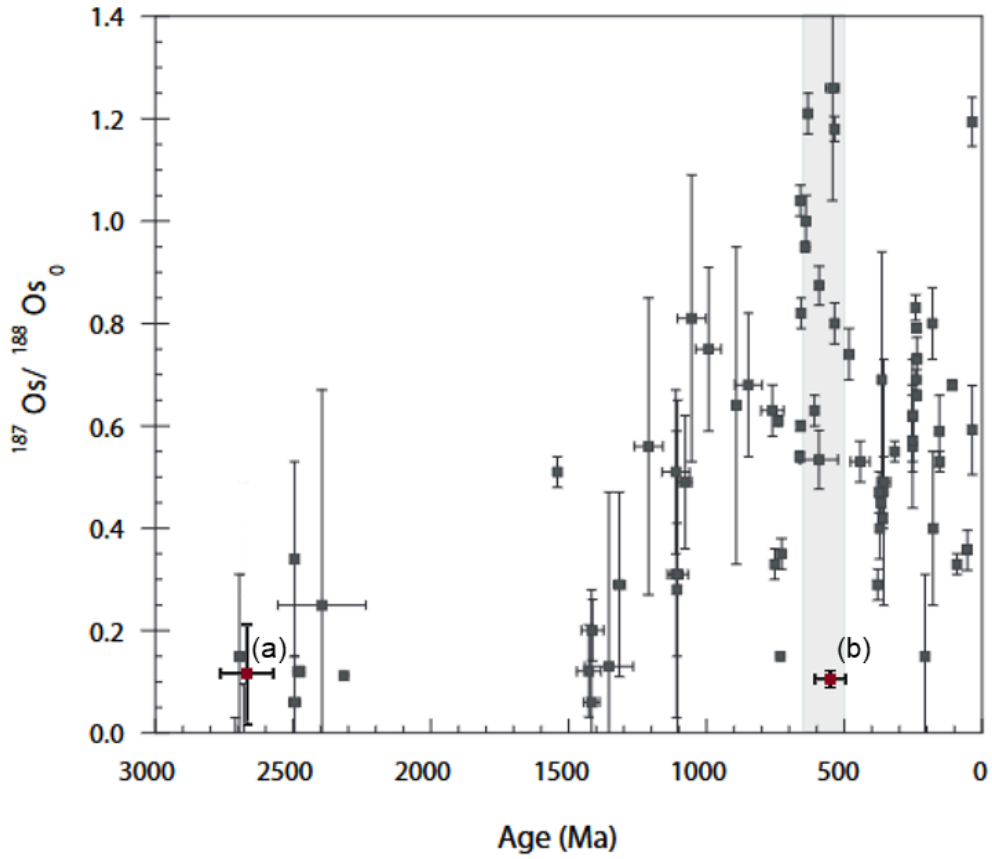

Figure 1.8: *Osmium seawater curve and age data with error-bars over the last 3 billion years of organic-rich materials. Results from two other studies on BIFs (red data points) were added: (a) Schulz et al. (2021); (b) Prost et al. (2024). The shaded area around the boundary of the Proterozoic and the Cambrian marks an unusually high excursion of the Os isotopic ratio (modified after Peucker-Ehrenbrink and Ravizza, 2020).*

In Figure 1.8, the osmium seawater evolution curve is plotted, recording data over the last 3 billion years. A general trend that can be observed is that the $^{187}Os/^{188}Os$ ratio is changing from an unradiogenic, chondritic-like, ratio in the Archean and Paleoproterozoic towards highly radiogenic values in the late Neoproterozoic exceeding those of the present-day Os isotope ratio (Peucker-Ehrenbrink and Ravizza, 2020; Rooney et al., 2024). This initial period of a low, chondritic-like $^{187}Os/^{188}Os$ ratio can be explained by a lack of oxidative weathering, due to a lack of oxygen itself, leading to a marine osmium isotope budget likely being dominated by hydrothermal sources (~0.13-0.88; Sharma et al., 2007; Lu et al., 2017). This trend continues until after the Great Oxidation Event, when oxidative mobilization of Re and Os into seawater was possible, leading to a rise in $^{187}Os/^{188}Os$ (Hannah et al., 2004; Kendall et al., 2015). Prior to the late Neoproterozoic peak in the $^{187}Os/^{188}Os$ ratio, the osmium seawater curve shifted toward more unradiogenic initial values. This trend may reflect

an increased input of mantle-derived osmium, either through hydrothermal activity or the weathering of basaltic rocks. The extensive weathering of basaltic material would have enhanced the consumption of atmospheric CO_2, potentially contributing to the onset of the Sturtian "snowball" glaciation (Goddéris et al., 2003; Rooney et al., 2014, 2015). The causes of the radiogenic peak in seawater $^{187}Os/^{188}Os$ ratios during the Neoproterozoic remain debated. Two leading hypotheses are an increased flux of continental material to the oceans (e.g., Van Acken et al., 2013) and the termination of the Sturtian glaciation (e.g., Rooney et al., 2014). However, due to the limited sample size, resolving this question remains difficult and is at risk of being overinterpreted (Peucker-Ehrenbrink and Ravizza, 2020).

The Paleozoic, like the Precambrian, lacks a well-constrained record of high-resolution Os isotope seawater compositions. However, existing studies have focused on intervals associated with major geological events (Peucker-Ehrenbrink and Ravizza, 2020). Percival et al. (2019) analyzed Devonian strata from around the Frasnian-Famennian mass extinction (Kellwasser event), which are marked by an increase in $^{187}Os/^{188}Os$ during this period of ~0.31 to ~0.83, interpreted as evidence for enhanced erosion of continental material. This continental input led to a more radiogenic seawater signal, which coincided with the mass extinction. A key limitation of this study, along with similar research on the Ordovician-Silurian boundary (e.g., Finlay et al., 2010; Li et al., 2023) or the Permian-Triassic boundary (e.g., Georgiev et al., 2015), is the lack of empirical data from additional sites to strengthen their interpretations (Peucker-Ehrenbrink and Ravizza, 2000, 2020).

As mentioned above, ORMs are the main way of generating global marine $^{187}Os/^{188}Os$ signatures in the Proterozoic, which raises the question of whether they truly reflect the initial, global seawater signature. Recently, attempts have been made to use banded iron formations as proxies for the marine $^{187}Os/^{188}Os$ ratios (Schulz et al., 2021; Prost et al., 2024) to either validate the data from ORMs or if they do not have the same seawater signature. The Temagami BIF (Schulz et al., 2021) and the Urucum BIF (Prost et al., 2024) both have mantle-like $^{187}Os/^{188}Os_{(i)}$ ratios (see red squares in Figure 1.8). In the case of the Neoarchean Temagami BIF, this aligns well with existing data from coeval ORMs. In contrast, the Urucum BIF data appear to contradict current understanding of the late Neoproterozoic, which is being characterized by a highly radiogenic seawater signature. Nevertheless, the data for the Urucum samples are still interpreted as reflecting pristine seawater, potentially recording an unradiogenic

excursion during this otherwise radiogenic period, possibly linked to glaciation events (Prost et al., 2024).

2 Geological Overview and previous work on the Tomka BIF

2.1 The Singhbhum Craton

The Singhbhum Craton (SC) is one of six Cratons on the Indian Peninsular, located in eastern India (Fig. 2.1). It encompasses an area of approximately 50,000 km^2 and has an ellipsoidal shape, extending ~200 km from north to south and ~150 km from east to west (Ramakrishnan and Vaidyanadhan, 2010; Olierook et al., 2019). The craton hosts a rock record from the Paleoarchean to the onset of the Proterozoic at ~2.5 Ga and is predominantly composed of supracrustal rocks (Olierook et al., 2019; Mukhopadhyay and Matin, 2020; Jodder, 2021). The stratigraphic framework of the Archean record of the SC, has been the subject of numerous classifications (e.g., Dunn and Dey, 1942; Iyengar and Murthy, 1982; Saha, 1988). However, its key components can be broadly categorized into four major lithological groups: the Older Metamorphic Group (OMG), the Older Metamorphic Tonalite Gneiss (OMTG), the Singhbhum Granite Batholitic Complex (SGBC), and the Iron Ore Group (IOG) (Saha, 1994; Jodder, 2021, and references therein).

The OMG comprises a volcano-sedimentary sequence that underwent up to amphibolite-grade metamorphism and occurs, along with the OMTG, in the central part of the SC. The OMTG consists of a suite of tonalite-trondhjemite-granodiorite (TTG) gneisses, representing some of the oldest rocks of the Indian shield, with depositional ages of around ~3.4 Ga (Jodder, 2021; Hofmann et al., 2022, and references therein). Notably, these TGG gneisses contain xenocrystic zircons with an age of ~4.24 Ga and 4.03 Ga, interpreted as evidence of reworking from an even older crustal source (Chaudhuri et al., 2018).

The SGBC, often referred to simply as the Singhbhum Granite, occupies the central portion of the craton (see Fig 2.1) and can be subdivided petrographically into at least three granitic phases: Phase I and II, composed of tonalite and granodiorite and phase III, consisting of granite (Saha, 1994; Jain et al., 2020; Hofmann et al., 2022, and references therein). The emplacement of the SGBC postdates that of the OMTG and OMG. The reported oldest age is at ~3.35 Ga and the youngest age is at ~3.05 Ga, respectively (Chaudhuri, 2020, and references therein).

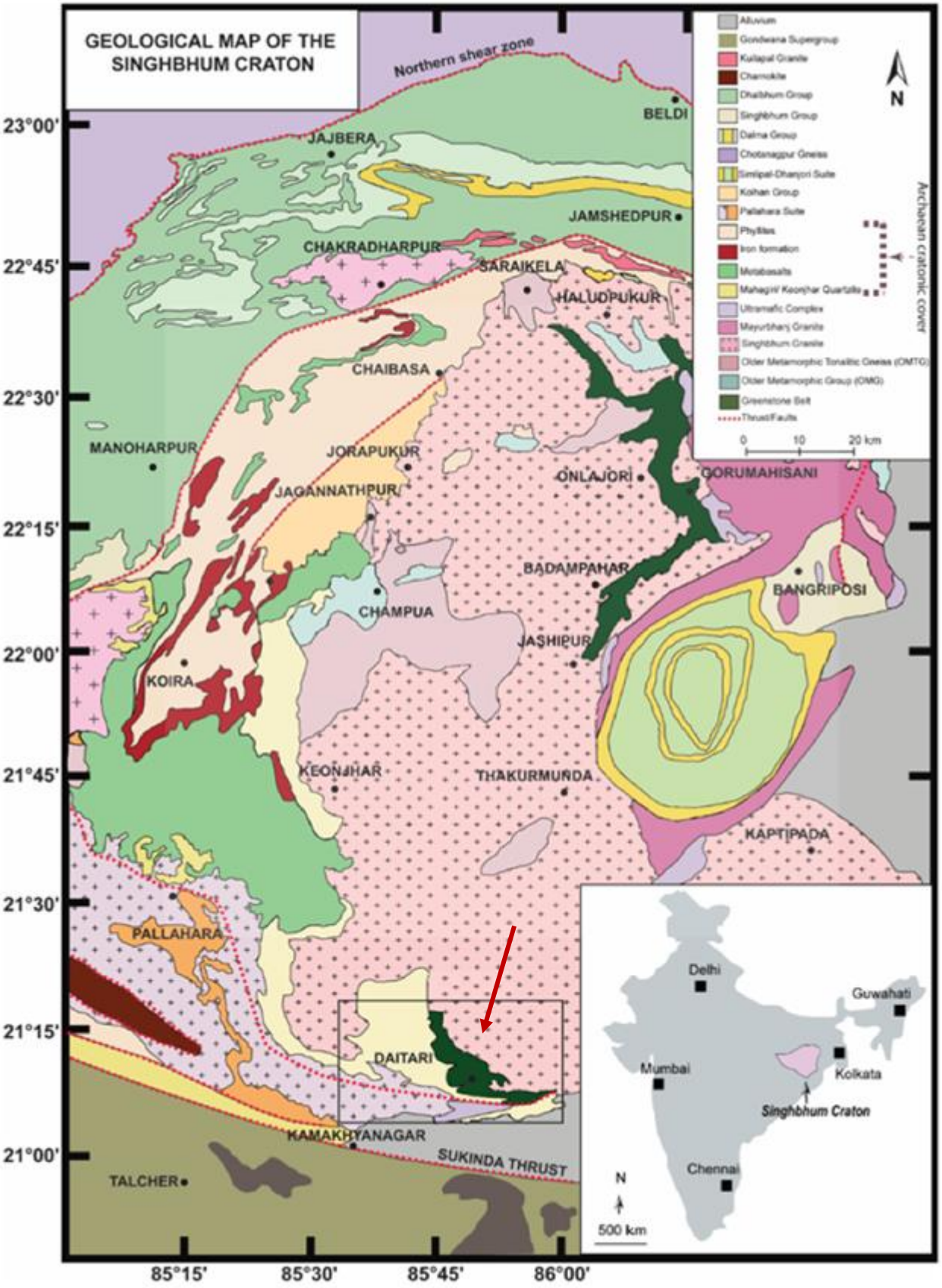

Figure 2.1: *Geological map of the Singhbhum Craton (SC) with a focus on the Archean geology. The red arrow points to the study area in the Daitari Greenstone Belt (modified after Jodder, 2021).*

The IOG contains successions of supracrustal rocks that experienced metamorphism not exceeding upper greenschist facies (Chaudhuri, 2020; Mukhopadhyay and Matin, 2020; Hofmann et al., 2022). The categorization of the IOG remains complex due to the variety of stratigraphic schemes proposed and used in the literature (e.g., Iyengar and Murthy, 1982; Saha, 1994; Ramakrishnan and Vaidyanadhan, 2010; Olierook et al., 2019; Jain et al., 2020; Mukhopadhyay and Matin, 2020). In principle, the IOG can be divided into three belts: (i) the Koira Belt, or western IOG, (ii) the Gorumahisani Greenstone Belt, or eastern IOG, and (iii) the Daitari Greenstone Belt (DGB), also called Daitari-Tomka Belt, or southern IOG, from which the samples analyzed in this study are derived. The Koira belt is interpreted to be the youngest sequence out of the three and is, therefore, frequently reassigned as the Koira Group, whereas the Gorumahisani Greenstone Belt and the Daitari Greenstone Belt are assigned to the Badampahar Group (Iyengar and Murthy, 1982; Jodder, 2021; Hofmann et al., 2022).

2.2 Daitari Greenstone Belt

The Daitari Greenstone Belt (DGB), as illustrated in Figure 2.1, is situated in the southernmost part of the Singhbhum Craton, covering an area of approximately 60 km^2. Around 70% of the DGB consists of mafic to ultramafic rocks that have undergone greenschist facies metamorphism. They are interbedded with banded chert and iron formation (Jodder, 2021; Hofmann et al., 2022; Jodder et al., 2023). As mentioned before, the DGB is assigned to the Badampahar Group, which includes a ~7-km-thick volcano-sedimentary sequence of the DGB, as proposed by Jodder (2021). The Badampahar Group is further subdivided into five formations (Figure 2.2):

(i) The Kalisagar Formation, being the lowest lithostratigraphic unit, comprising a ~3-km-thick succession of mafic/ultramafic rocks. Intrusive quartz-muscovite schists, dated between 3.51 and 3.39 Ga (Jodder et al., 2023), suggests that the mafic rocks of the Kailsagar Formation are older than 3.51 Ga.

(ii) The overlying Talpada Formation has a thickness of ~1.5 km and consists predominantly of felsic pyroclastic rocks, mainly dacitic to rhyodacitic in composition. Previously dated by Mukhopadhyay et al. (2008) (using uranium-lead (U-Pb) SHRIMP zircon dating in dacitic lava) and Jodder et al. (2023) (also using U-Pb SHRIMP zircon dating in dacite) to be ~3.51 Ga old,

this formation provides additional support for the interpretation that the underlying Kalisagar Formation predates 3.51 Ga.

(iii) The ~500-m-thick Sindirimundi Formation is dominantly made up of clastic sedimentary rocks, including conglomerates, sandstone and laminated shales. The stratigraphy follows an overall upward-fining trend, with conglomerates at the base transitioning into laminated shales and chert at the top. Samples from the turbidite sequence in the Sindirimundi Formation were dated by Jodder et al. (2023) using U-Pb SHRIMP zircon dating, giving an age of ~3.51 Ga which is practically identical to the age constraints of the Talpada Formation (Mukhopadhyay et al., 2008; Sreenivas et al., 2019).

(iv) The Tomka Formation, which will be discussed in more detail in the following chapter, is a ~700-m-thick consisting of conglomerates and, notably, banded black-and-white chert and iron formations (which are thought to have been deposited between ~3.51 to 3.28 Ga).

(v) The Talangi Formation is the uppermost unit of the Badampahar Group in the DGB. It consists of a ~1-km-thick sequence of basalts and thin cherts units. This formation is unconformably overlain by the Mahagiri quartzite-conglomerate (age: ~3.02 Ga; Mukhopadhyay et al., 2016), which does not belong to the Badampahar Group (Jodder, 2021; Jodder et al., 2023).

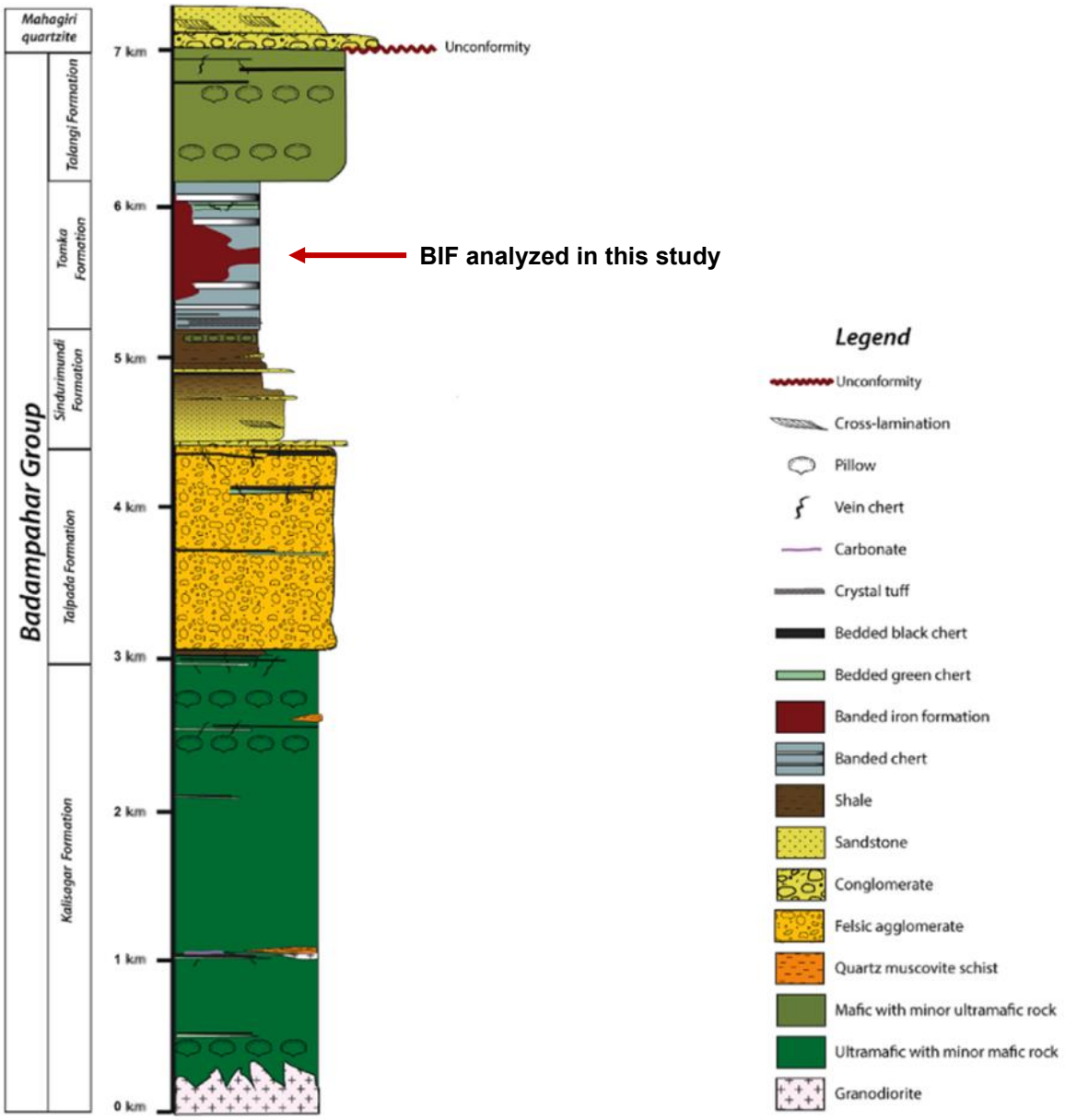

Figure 2.2: *Stratigraphic column of the Badampahar Group of the Daitari Greenstone Belt. The red arrow indicates the studied BIF in the Tomka Formation (modified after Jodder, 2023).*

2.3 Tomka Formation and BIF

The contact between the Tomka Formation and the underlying Sindirimundi Formation is conformable, marked by a conglomerate containing sandstone, which transitions into banded cherts and iron formation. No direct geochronological data are available for the Tomka Formation or the overlying Talangi Formation, due to no suitable material being present for age dating (Jodder et al., 2023). However, the Sindirimundi Formation, interpreted to have a maximum depositional age of ~3.50 Ga (Jodder, 2021; Jodder et al., 2023), provides a constraint for the overlying BIF, suggesting they formed within a similar time frame. Narrowing down the time frame further, the deposition of the Tomka Formation likely occurred between 3,507 ± 5 Ma, which is interpreted to be deposition

age of the Talpada Formation (Jodder et al., 2023), and 3,278 ± 9 Ma, defined by the age when the regional metamorphism of the Badampahar Group is thought to have taken place (Hofmann et al., 2022). These ages were derived from (i) zircon crystals in volcaniclastic rock within the Talpada Formation using U-Pb SHRIMP analysis (Jodder et al., 2023) and (ii) from zircon crystals of intruded granitoids from the OMG using U-Pb SHRIMP analysis. This leads to an approximated deposition age of the BIF of between ~3.51 to 3.28 Ga.

The BIF within the Tomka Formation consists of hematite- or magnetite-rich layers interbedded with Fe-rich silicates and white-chert. The iron formation bands include macrobands up to 0.5 m thick and mesobands ranging from 2 to 5 cm in thickness (Figure 3.1). The Tomka Formation is proposed to have formed in a submarine setting, consistent with an Algoma type BIF, a classification that was also applied to the BIFs of the eastern IOG in the Gorumahisani Greenstone Belt (Sarkar and Gupta, 2012; Jodder, 2021; Jodder et al., 2023).

Kienle (2024) analyzed rare earth elements and yttrium in these BIFs, demonstrating that their geochemical signatures closely resemble those of modern seawater. Her study found little to no evidence of detrital contamination, comparing it with the similar aged BIFs from the Moodies Group (~3.22 Ga; Heubeck et al., 2013; Bonnand et al., 2020) and younger BIFs such as those in the Mesoarchean Witwatersrand Supergroup (~2.90 Ga; Viehmann et al., 2015b) and the Pietersburg Greenstone Belt (~2.95 Ga; De Wit et al., 1993; Alexander et al., 2009). Additionally, her findings indicate that high-temperature hydrothermal input was the primary, if not the sole, fluid influencing BIF deposition in the Tomka Formation.

3 Samples and methods

3.1 Samples and Preparation

The rock samples chosen for this thesis were initially collected by A. Hofmann, J. Jodder (in the case of sample series DM17, DM22, DM71A and DM90), and S. Viehmann (sample series IND-DGB-BIF) in Daitari, India, in 2020. The selected samples are all from the Tomka Formation, except for sample DM71A, which is part of the underlying Sindirimundi Formation. Kienle (2024) found that these samples represent the Archean seawater composition arguably limited to no syn- or postdepositional alterations for the REEs, with the exception to sample DM71A, which was determined as a detrital aluminosilicate endmember.

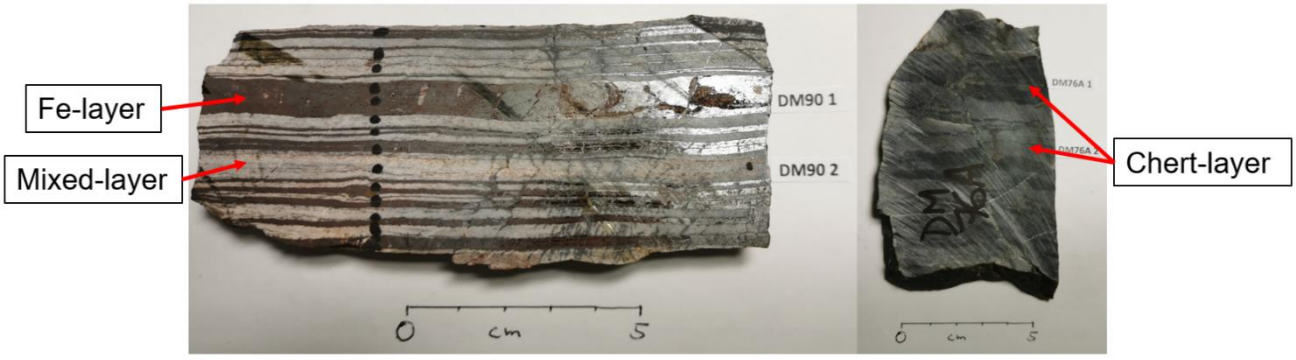

Figure 3.1: *Pictures of sample DM90 (left) and DM71A (right). Three different layer types can be observed with the unaided eye. The iron layer being red-brown in color, the mixed layer white and the chert layer black. The shale sample is not pictured here. Photo courtesy of S. Kienle.*

For the present thesis eight rock samples (Figure 3.1 showing two of them), received from Sebastian Viehmann, were cut into individual layers and prepared as homogenous powders, yielding a total of 15 samples for this thesis.

These 15 samples represent four different lithologies (see Figure 3.1): (i) an Iron-layer, (ii) a chert-layer, (iii) a mixed Fe-Si layer, and (iv) a single shale sample. Figure 3.1 shows two samples DM90 (the Fe-layer DM90-1 was not used in this thesis) and DM71A, where examples for all the lithologies, except the shale-layer, are evident. The Fe-layers are generally of red-brownish color and have a distinct metallic gloss. The Si-Fe-mixed layer has a white-greyish color, and the chert layer is black.

Sample	Latitude	Longitude	Sample layer-ID	Layer type
DM17C	21.0945	85.8841	DM17C2	Shale
DM17D	21.0945	85.8841	DM17D1	Chert
			DM17D2	Chert
DM22B	stream samples, no specific locality		DM22B2	Mixed layer
			DM22B3	Mixed layer
			DM22B4	Mixed layer
DM22D	stream samples, no specific locality		DM22D1	Fe-layer
			DM22D2	Fe-layer
DM71A	21.1131	85.7981	DM71A	Clay
DM90	21.1001	85.7925	DM90-2	Mixed layer
IND-DGB-BIF2 1	21.5634	85.4871	IND-DGB-BIF2 1a	Mixed layer
IND-DGB-BIF2	21.5634	85.4871	IND-DGB-BIF2 2	Mixed layer
			IND-DGB-BIF2 4	Mixed layer
			IND-DGB-BIF2 5	Mixed layer
			IND-DGB-BIF2 6	Mixed layer

Table 1: *Listing of the samples and sample layer-IDs including their GPS localities (in degrees). Data courtesy of S. Kienle.*

3.2 Methodology

3.2.1 Wet chemistry

The wet chemical treatment (see Figure 3.2 for an overview) of the sample included weighing about 200 mg of whole-rock powder of each sample into quartz-vials and adding 10 to 30 mg of a tracer solution for isotope dilution (spike, containing ^{99}Ru, ^{105}Pd, ^{185}Re, ^{190}Os, ^{191}Ir and ^{194}Pt; see Appendix A1). These steps were followed by the addition of ~2 ml of concentrated and double distilled concentrated HCl in small increments to remove any carbonate from the samples and to avoid CO_2 production during high pressure digestion. After full reaction (if any), ~5 ml of HNO_3 was added to the sample-spike mixture, forming aqua regia. The quartz vials where then sealed with a PTFE film and placed into an Anton-Paar high-pressure asher (HPA-S) for three hours at a temperature of 270 °C and a pressure of 100-130 bar. This process enabled sample-spike equilibration and leached the HSEs from the whole-rock samples into the aqua regia (Cohen and Waters, 1996).

Osmium separation

Following the HPA-S treatment, the vials were reopened and 3 ml $CHCl_3$ was added to bind osmium and prevent its volatilization, as the aqua regia oxidized osmium to the volatile compound osmium tetroxide (OsO_4). To separate the Os from the other HSEs,

the aqua regia-$CHCl_3$ fraction was transferred into centrifuge tubes. After adding 4 more milliliters of $CHCl_3$ to the aqua regia-$CHCl_3$ fractions, all vials were placed on a sample mixer. Subsequently $CHCl_3$ was separated from the aqua regia using pipettes and 15 ml Savillex beakers, which were pre-filled with 4 ml of ultrapure 9 M HBr. After several intermediate steps of adding small increments of $CHCl_3$ and further sample mixing, all $CHCl_3$ was transferred to the Savillex beaker. These beakers were placed on the sample mixer over night to allow partition of Os from $CHCl_3$ into the HBr phase, reducing the OsO_4 forming bromide complexes (Hexabromoosmate(IV)-complexes, i.e., $[OsBr_6]^{-2}$).

After mixing, the liquid in the beakers containing the $CHCl_3$-HBr mixture separated into two visibly unmixed phases (bottom layer of $CHCl_3$ and top layer of HBr). In a back-extraction procedure $CHCl_3$ was removed using micropipettes and the HBr dried down on a hotplate at 60 °C (Cohen and Waters, 1996). The final step for the separation of Os is the microdistillation described in Birck et al. (1997), where pure and concentrated H_2SO_4 was added together with a CrO_3 solution as oxidant to the Os sample, which oxidized and then partitioned (in a closed system) into a drop of ultrapure HBr. The remaining aqua regia was added to the undissolved sample and transferred into a Savillex beaker, dried down and subsequently treated with HF to dissolve the silicate phases (which host a substantial amount of Re).

HSE(-Os) separation

The aforementioned aqua regia, containing the rest of the HSEs, was now prepared for a two-step ion-exchange chromatography as described by Pearson and Woodland (2000). The chromatography, following a recipe (see Appendix A2) to isolate the rest of the HSEs (Ru, Re, Ir and Pt) minus Pd, which is collected in a separate column chemistry stage. In a two-stage chromatographic exchange chemistry in both cases the resin must be cleaned first, see recipe in Appendix A2 and then equilibrated before loading them with the sample. Following these procedures, in a first stage column chemistry, Pd was separately collected from the HSEs (minus Os), using an AG1X8 resin in the process. In a second stage chemistry, an LN-Spec column was used, also separating Pd first and the rest of the HSEs.

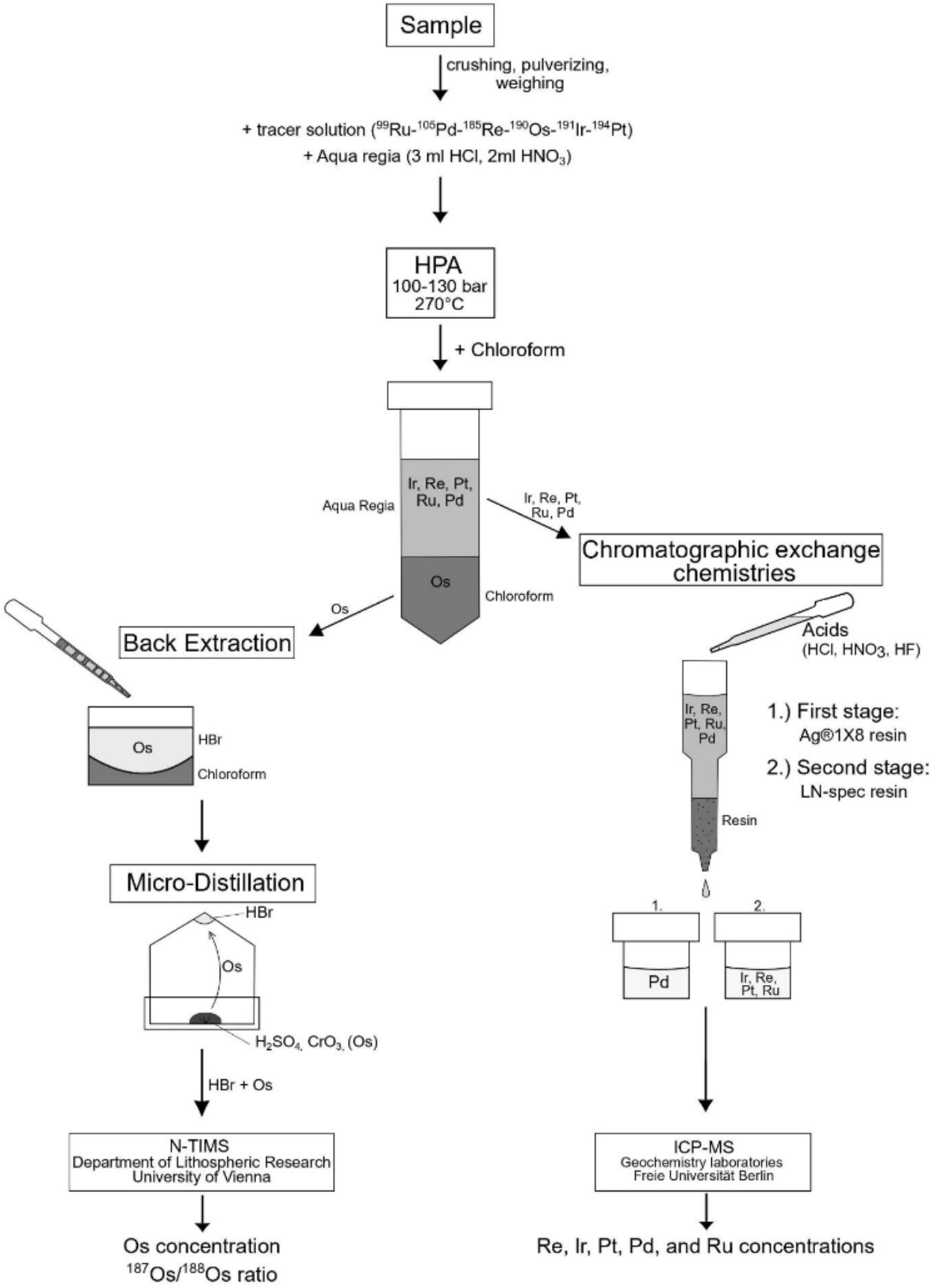

Figure 3.2: *Schematic diagram of the wet chemistry performed for this study. A description of the recipes for the chromatographic anion exchange chemistry can be found in Appendix A1 (modified after Wernitznig, 2023).*

3.2.2 Mass spectrometry

Osmium measurements

The measurements of the osmium isotopic composition were performed at the Department of Lithospheric Research at the University of Vienna, Austria, using a Thermo TRITON TIMS operating in negative ion mode. Osmium was subsequently loaded in the form of a bromide complex $(OsBr_6)^{2-}$ with a $NaOH/Ba(OH)_2$ activator. This $NaOH/Ba(OH)_2$ activator provided an oxygen source, promoting more efficient ionization of Os. Although isobaric interferences from W- or Pt-oxides were not detected, significant isobaric overlap of ^{187}Re on ^{187}Os occurred in some instances. This was monitored by measuring $^{185}ReO_3^-$ (mass 233) and corrected when present, typically amounting to fewer than 5 to 10 counts at mass 233. Mass fractionation was corrected offline using a $^{192}Os/^{188}Os$ ratio of 3.083 (Brandon et al., 2005; Luguet et al., 2008). During certain runs, oxygen was introduced into the vacuum chamber of the mass spectrometer to enhance ionization efficiency. The procedural Os blank was measured approximately 0.8 ppt, necessitating blank correction for all sample analyses. Alongside the sample measurements, repeated analyses (n=5) of ~10 pg loads of a DROsS (Durham Romil Osmium Standard) solution were conducted. These analyses employed the electron multiplier at signal intensities similar to those observed in the sample runs (approximately 1,000 to 100,000 counts at mass 240, corresponding to $^{192}OsO_3^-$), and the results were consistent with values reported in the literature (e.g., Luguet et al., 2008).

HSE(-Os) measurements

The HSE analyses (without Os) were carried out at the geochemistry laboratories of the Free University of Berlin, Germany, using a Thermo Element XR ICP-MS in the single collector mode, an Aridus I Desolvating Nebulizer system and methods described in Luguet et al. (2015). An in-house 1 ppb multi-element HSE standard solution was employed to monitor instrumental drift, with measurements taken at the start, midpoint, and conclusion of the analytical session. Mass bias was corrected relative to this standard using ratios of 0.5986 for $^{185}Re/^{187}Re$, 0.5957 for $^{191}Ir/^{193}Ir$, and 0.2117 for $^{198}Pt/^{195}Pt$. For all samples, these corrections proved negligible. Isobaric interferences from Hf affecting Ir and Pt were tracked and corrected during offline data processing.

To assess oxide formation, Hf-doped 1 ppb HSE solutions were analyzed at the beginning, middle, and end of each analytical session. Rhenium, iridium, and platinum were measured using a cyclonic borosilicate glass spray chamber. Procedural blanks for the study amounted to 12 pg for Re, 1.2 pg for Ir, 47 pg for Ru, 67 pg for Pt, and 54 pg for Pd. Blank corrections were applied by directly subtracting the blank contributions from the total analyzed amounts detected. Although blank corrections were applied to all cases due to the HSE contents of the samples, they were generally insignificant. Analytical quality was assessed through repeated measurements of the standard reference material OKUM (Ontario komatiite ultramafic; Meisel et al., 2013), which was processed alongside the samples. All analyses of the reference materials reproduce the certified values within a 2σ margin of error.

4 Results

4.1 Highly siderophile elements

Concentrations of all measured HSEs are given in Table 2. They vary from ~0.01 to ~4.16 ppb for Re, from ~0.11 to ~7.81 ppb for Os, from ~0.01 to ~0.06 ppb for Ir, from ~0.07 to ~5.68 ppb for Pt, from ~0.07 to ~0.86 for Ru and from ~0.82 to ~7.48 ppb for Pd. However, neglecting outliers (sample DM17D2 for Os, IND-DGB-BIF2 6 for Re and IND-DGB-BIF2 5 for Pt), these values average at 0.26 ± 0.02 ppb for Re, at 0.38 ± 0.01 ppb for Os, at 0.03 ± 0.003 ppb for Ir, at 0.41 ± 0.05 ppb for Pt, at 0.32 ± 0.03 ppb for Ru and at 2.10 ± 0.20 ppb for Pd. The interelement ratios, which are presented in Table 3, range from ~0.03 to ~32.0 for Re/Os, from ~2.41 to ~236 for Pt/Ir, from ~1.80 to ~296 for Os/Ir, from ~0.01 to ~0.98 for Ru/Pd, from ~0.004 to ~0.41 for Ir/Pt.

Concentrations of the HSEs in question from previously studied IFs, including data from the Urucum BIF (Prost et al., 2024) and those from the Temagami BIF (Schulz et al., 2021) vary from ~0.01 to ~4.00 ppb for Re, from ~0.001 to ~3.96 ppb for Os, from ~0.001 to ~0.17 ppb for Ir and from ~0.01 to ~2.18 ppb for Pt. There are no Ru and Pd data available for the Temagami BIF, but for the Urucum BIF the Ru concentrations lies between ~0.04 to ~5.80 ppb and from ~0.31 to ~2.31 ppb for Pd. Chu et al. (2023) analyzed ironstone samples from the Yunmengshan (YMS) formation, which have distinctly lower HSE contents of between ~0.002 to ~0.01 ppb for Re, from ~0.03 to ~0.04 ppb for Os, from ~0.35 to ~0.62 ppb for Ir, from ~4.59 to ~7.94 ppb for Pt, from ~0.90 to ~1.62 ppb for Ru and from ~0.20 to ~0.43 ppb for Pd. The interelement ratios from these IFs cover even wider ranges of values compared to the Tomka BIF, from ~0.05 to ~133 for Re/Os, from ~0.64 to ~545 for Pt/Ir, from ~0.32 to ~990 for Os/Ir, from ~0.13 to ~3.83 for Ru/Pd and from ~0.002 to ~1.55 for Ir/Pt (Schulz et al., 2021; Prost et al., 2024). Data from the YMS ironstones contain generally lower ratios from ~0.06 to ~0.46 for Re/Os, from ~9.64 to ~21.9 for Pt/Ir, from ~0.06 to ~0.09 for Os/Ir, from ~2.20 to ~8.06 for Ru/Pd and from ~0.05 to ~0.10 for Ir/Pt (Chu et al., 2023).

Rhenium and Os have the highest variability in terms of concentrations in all so far analyzed ironstones and BIFs, ranging from ~0.002 to ~4.00 ppb for Re and from ~0.001 to ~3.96 ppb for Os respectively, leading to a higher HSE abundance then the UCC (~0.20 ppb for Re and ~0.03 ppb for Os; Peucker-Ehrenbrink and Jahn, 2001) and that of modern seawater (~0.007 ppb for Re and ~$1.0 \cdot 10^{-5}$ ppb for Os; Stein and Hannah, 2014). The other HSE contents (Ir, Pt, Ru and Pd) are more uniform compared

to Re and Os, but they too contain strong outliers in some cases. For example, the Ru concentration in the Urucum BIF can be as high as 5.80 ppb and the Pt concentrations in the YMS ironstones are by far the highest in the present studies, being as high as 7.94 ppb.

In general, the Tomka BIF have rather uniform HSE concentrations, excluding outliers such as those mentioned above, that are comfortably within the previously presented ranges, except for Pd, which on average is on the upper end of the concentration range reported in the literature. With respect to the HSE abundance of the UCC and the modern seawater, the Tomka BIF has, on average, higher concentrations, with the exception of Pt, which has a concentration of ~0.51 ppb in the UCC (Peucker-Ehrenbrink and Jahn, 2001), higher than that of the Tomka BIF, averaging at ~0.41 ppb. Similar to more recent marine precipitates, like carbonates, Ir should also be able to preserve extraterrestrial signatures (e.g., asteroid impact-derived) in its rock record. Iridium spikes in some samples at the K-Pg boundary record concentrations of up to about 100 ppb (Claeys et al., 2002, and references therein). Iridium abundances this high have not been observed in iron formations, only up to concentrations of ~13 ppb in the Brockman IF (Glikson and Allen, 2004), which is interpreted to be a signal of an Archean asteroid impact. For the Temagami BIF, Urucum BIF, YMS ironstones and the Tomka BIF studied here, the Ir contents do not indicate any meteoritic admixture throughout all lithologies (not exceeding ~0.17 ppb).

Looking at the interelement ratios of the Tomka BIF compared to the presented literature data, no apparent trend can be observed, as the Tomka BIF ratios all are within the range of the interelement ratios from the literature. The only exception is the Ru/Pd ratio, which, for the Tomka BIF, has values (~0.01 to ~0.98) that are outside of the interelement ratios of the other BIFs (~0.13 to ~3.83; Schulz et al., 2021; Prost et al., 2024). For the Ru/Pd ratio of the YMS ironstone the opposite is true, with ratios outside the upper boundary of those from all the studied BIFs of ~2.20 to ~8.06 (Chu et al., 2023). Modern seawater interelement ratios, as well as the UCC data generally lie within the boundaries of the available BIF data (including the Tomka BIF), except for the Re/Os ratio of modern seawater, where the values (~700; Stein and Hannah, 2014) far exceed the maximum Re/Os ratio of the BIFs of ~133. In the case of the UCC, only the Os/Ir ratio is below the interelement ratios of the BIFs with ~1.41 (Peucker-Ehrenbrink and Jahn, 2001).

Samples	Lithology	Re [ppb]	Re 2σ	Os [ppb]	Os 2σ	Ir [ppb]	Ir 2σ	Pt [ppb]	Pt 2σ	Ru [ppb]	Ru 2σ	Pd [ppb]	Pd 2σ	$^{187}Os/^{188}Os$	2σ	$^{187}Re/^{188}Os$	2σ	$^{187}Os/^{188}Os(i)$
DM71A	Shale	0.014	0.005	0.518	0.008	0.029	0.004	0.491	0.041	0.173	0.047	1.381	0.217	0.407	0.004	0.133	0.051	0.399
DM17D1	Chert	0.359	0.033	1.068	0.002	0.029	0.002	0.602	0.125	0.633	0.034	2.345	0.220	0.142	0.001	1.603	0.150	0.045
DM17D2	Chert	0.354	0.028	7.81	0.32	0.029	0.004	0.070	0.007	0.553	0.027	1.111	0.131	0.127	0.001	0.216	0.027	**0.114**
DM17C2	Chert	0.573	0.051	0.800	0.027	0.040	0.005	0.351	0.031	0.482	0.028	1.280	0.161	0.154	0.003	3.422	0.435	-0.052
DM22D1	Iron	0.110	0.009	0.108	0.002	0.060	0.008	0.376	0.026	0.071	0.011	1.151	0.096	0.402	0.006	5.026	0.514	**0.101**
DM22D2	Iron	0.157	0.012	/	/	0.030	0.002	0.582	0.092	0.109	0.019	2.322	0.305	0.193	0.001	/	/	/
IND-DGB-BIF2 1a	Mix	0.141	0.029	0.316	0.006	/	/	/	/	/	/	/	/	0.264	0.003	2.163	0.495	**0.134**
IND-DGB-BIF2 2	Mix	0.130	0.010	0.166	0.002	0.034	0.003	0.472	0.042	0.174	0.024	1.442	0.176	0.361	0.002	3.844	0.336	**0.130**
IND-DGB-BIF2 4	Mix	0.407	0.035	0.397	0.006	0.040	0.004	0.780	0.080	0.193	0.030	1.650	0.162	0.220	0.002	4.941	0.507	-0.077
IND-DGB-BIF2 5	Mix	0.544	0.039	0.129	0.002	0.024	0.003	5.676	0.476	0.863	0.110	4.101	0.438	0.296	0.002	20.49	1.81	-0.934
IND-DGB-BIF2 6	Mix	4.16	0.60	0.130	0.001	0.034	0.003	0.466	0.066	0.096	0.016	7.484	0.393	0.243	0.001	155	24	-9.072
DM22B2	Mix	0.117	0.011	/	/	0.008	0.001	0.552	0.072	0.100	0.002	2.069	0.169	0.167	0.001	/	/	/
DM22B3	Mix	0.070	0.009	0.329	0.008	0.012	0.001	0.243	0.043	0.797	0.052	0.816	0.124	0.164	0.002	1.018	0.160	**0.103**
DM22B4	Mix	0.103	0.008	0.216	0.003	0.030	0.004	0.130	0.020	0.188	0.023	0.955	0.152	0.292	0.004	2.320	0.215	**0.153**
DM90-2	Mix	0.494	0.017	/	/	0.034	0.002	0.160	0.020	0.103	0.025	1.158	0.068	0.182	0.002	/	/	/
IF-G[a]	Bulk	0.171	/	0.029	/	0.005	/	0.164	/	/	/	/	/	2.472	0.029	36.81	1.1	2.11
IF-G[b]	Bulk	0.141	0.070	0.024	0.002	0.003	0.002	0.280	0.027	1.208	0.014	0.606	0.026	2.803	0.06	37.85	/	2.43
UCC[c]	/	0.198	/	0.031	/	0.022	/	0.510	/	0.210	/	0.520	/	1.400	/	34.5	/	/
CI[d]	/	41	/	491	/	462	/	943	/	688	/	563	/	0.126	/	0.392	/	/
PUM[e]	/	0.350	0.060	3.900	0.500	3.500	0.400	7.600	1.300	7.000	0.900	7.100	1.300	0.130	0.001	/	/	/
Modern seawater[f]	/	0.007	/	1.0E-05	/	3.0E-06	/	5.0E-04	/	/	/	4.1E-04	/	1.060	/	/	/	/
OKUM[g]	Komatiite	0.566	0.080	0.790	/	0.943	0.080	11.44	/	4.150	0.080	12.20	1.460	/	/	/	/	/
OKUM[h]	Komatiite	/	/	0.780	/	0.990	0.070	11.44	/	4.530	/	11.93	/	/	/	/	/	/
OKUM[i]	Komatiite	0.475	/	0.790	/	0.843	/	10.70	/	4.190	/	11.10	/	0.269	/	/	/	/
OKUM[j]	Komatiite	0.471	/	0.722	/	0.813	/	12.60	/	4.400	/	11.50	/	0.278	0.000	/	/	/
OKUM[a]	Komatiite	0.514	/	0.746	/	0.812	/	12.14	/	/	/	/	/	0.293		/	/	/
OKUM[b]	Komatiite	0.461	0.014	0.811	0.015	0.868	0.022	11.93	0.280	3.835	0.207	13.28	0.210	0.277	0.003	2.29	/	0.255

[a]Schulz et al. 2021, [b]Prost, 2023, [c]Peucker-Ehrenbrink, Jahn 2001; [d]Fischer-Gödde et al. 2010; [e]Becker et al. 2006, Meisel et al. 2001; [f]Lee 1983, Li et al. 2007, Stein and Hannah 2014, Mashio et al. 2017, Liu et al. 2018; [g]Savard et al. 2010; [h]Maier et al. 2012; [i]Chen et al. 2016; [j]Puchtel et al. 2018

Table 2: *Average concentrations and errors of chosen highly siderophile elements in parts per billion (ppb) and Re-Os isotopic composition of the samples. Six samples, highlighted in bold, have PUM-like ($^{187}Os/^{188}Os)_{(i)}$ ratios. Literature data of Temagami BIF[a], Urucum BIF[b] and those of the upper continental crust (UCC)[c], primitive upper mantle (PUM)[e], CI chondrites (CI)[d], the modern seawater[f] and of Ontario komatiite ultramafic (OKUM) reference material[f-k] are given for comparison.*

Analyzing and comparing the HSEs abundances of the individual lithologies indicates that the iron samples contain the lowest concentrations for Re, Os, and Ru, between ~0.11 to ~0.16 ppb for Re, ~0.11 ppb for Os, and between ~0.07 to ~0.11 ppb for Ru, although due to the limited sample size of only two studied iron samples, this observation should be interpreted with caution. Osmium concentrations are by far highest within the chert samples, from ~0.80 to ~1.07 ppb (excluding outliers). For comparison, the Os abundance for both iron- and mixed samples vary between only ~0.11 to ~0.24 ppb. The abundance of Re is also highest within the chert samples, though not as clear as with Os, ranging from ~0.35 to ~0.57 ppb, with an average of

Samples	Lithology	Re/Os	Pt/Ir	Os/Ir	Ru/Pd	Ir/Pt
DM71A	Shale	0.027	16.93	17.86	0.125	0.059
DM17D1	Chert	0.336	20.76	36.83	0.270	0.048
DM17D2	**Chert**	0.045	2.414	269	0.498	0.414
DM17C2	Chert	0.716	8.775	20.00	0.377	0.114
DM22D1	**Iron**	1.019	6.267	1.800	0.062	0.160
DM22D2	Iron	/	19.40	/	0.047	0.052
IND-DGB-BIF2 1a	**Mix**	0.446	/	/	/	/
IND-DGB-BIF2 2	**Mix**	0.783	13.88	4.882	0.121	0.072
IND-DGB-BIF2 4	Mix	1.025	19.50	9.925	0.117	0.051
IND-DGB-BIF2 5	Mix	4.217	237	5.375	0.210	0.004
IND-DGB-BIF2 6	Mix	31.97	13.71	3.824	0.013	0.073
DM22B2	Mix	/	69.00	/	0.048	0.014
DM22B3	**Mix**	0.213	20.25	27.42	0.977	0.049
DM22B4	**Mix**	0.477	4.333	7.200	0.197	0.231
DM90-2	Mix	/	4.706	/	0.089	0.213
IF-G[a]	Bulk	5.897	32.80	5.800	/	0.030
IF-G[b]	Bulk	5.867	93.33	8.000	1.993	0.011
UCC[c]	/	6.387	23.18	1.409	0.404	0.043
CI[d]	/	0.083	2.041	1.063	1.222	0.490
PUM[e]	/	0.090	2.171	1.114	0.986	0.461
Modern seawater[f]	/	700	167	3.333	/	0.006
OKUM[g]	Komatiite	0.716	12.13	0.838	0.340	0.082
OKUM[h]	Komatiite	/	11.56	0.788	0.380	0.087
OKUM[i]	Komatiite	0.601	12.69	0.937	0.377	0.079
OKUM[j]	Komatiite	0.652	15.50	0.888	0.383	0.065
OKUM[a]	Komatiite	0.689	14.95	0.919	/	0.067
OKUM[b]	Komatiite	0.568	13.74	0.934	0.289	0.073

[a]Schulz et al. 2021, [b]Prost, 2023, [c]Peucker-Ehrenbrink, Jahn 2001; [d]Fischer-Gödde et al. 2010; [e]Becker et al. 2006, Meisel et al. 2001; [f]Lee 1983, Li et al. 2007, Stein and Hannah 2014, Mashio et al. 2017, Liu et al. 2018; [g]Savard et al. 2010; [h]Maier et al. 2012; [i]Chen et al. 2016; [j]Puchtel et al. 2018

Table 3: *Interelement ratios of selected highly siderophile elements of the samples. Six samples, highlighted in bold, have a PUM-like ($^{187}Os/^{188}Os)_{(i)}$ ratio. Literature data of Temagami BIF[a], Urucum BIF[b] and those of the upper continental crust (UCC)[c], CI chondrites (CI)[d], the primitive upper mantle[e] the modern seawater[f] and of Ontario komatiite ultramafic (OKUM) reference material[g-k] are given for comparison.*

~0.43 ppb, compared to the average in the mixed samples of ~0.25 ppb. Iridium, Pt and Pd all have rather homogeneous abundances between the different lithologies, in contrast to the mentioned heterogeneities of the other HSEs.

Considering the interelement ratios between the different lithologies, similar to the HSE concentrations, no pattern emerges when comparing the different sample lithologies. The mixed samples tend to have the highest Re/Os, from ~0.21 to ~4.28, and Pt/Ir ratios, from ~4.33 to ~69.0, excluding two outliers with a Re/Os ratio of ~32.0 and a Pt/Ir ratio of ~236. The chert samples, on the other hand, has the highest Os/Ir, Ir/Pt ratios from ~20.0 to ~269 for Os/Ir and from ~0.05 to ~0.41 for Ir/Pt. They also have the on average highest Ru/Pd ratios of ~0.38, though the mixed samples capture the highest ratio of ~0.98. In the iron samples, Pt/Ir, Ru/Pd, and Ir/Pt ratios are consistently at the lower end of the observed range. The limited data for Re/Os and Os/Ir ratios, each represented by only one value, prevent a robust comparison with other lithologies.

In theory, these elements and other HSEs are expected to have higher abundances in the iron samples compared to cherts, with mixed samples lying in-between. However, this is clearly not the case for the observed HSEs concentration as well as for the interelement ratios. Quite the opposite is the case, which can be observed in Figure 4.1, with chert samples recording higher concentrations for nearly all of the analyzed HSEs. Based on the limited number of measured samples analyzed in this study, it is not possible to explain this behavior. Possible explanations could be that mixed samples are not a simple bimodal mixture between chert- and iron samples, or that the analyzed iron samples are not typical for Tomka BIF iron samples in general (only two samples were measured). However, the most obvious (but not confirmed) explanation might be the “nugget effect”, i.e., the heterogeneous distribution of platinum group elements due to their geochemical properties within host rocks and thus also in the powder used for the analyses (e.g., T. Meisel et al., 2001; Aulbach et al., 2016). Given the small sample mass (typically ~200 mg) this might be the most plausible explanation for the observed phenomenon. This is further supported by trace element and REE data from the Tomka BIF (see Figure 5.1 in Chapter 5.1.2), which suggest a clear separation between the lithologies. While the chert samples have the lowest concentrations of these elements, the iron samples generally contain the highest, consistent with the nugget effect possibly influencing and explaining the HSE distributions. Interestingly, Kienle (2024) also analyzed REY patterns across lithologies

within the Tomka BIF but concluded that no clear distinction between the lithologies can be observed. However, if one outlier sample from the dataset of Kienle (2024) would be excluded, a pattern similar to that illustrated in Figure 5.1 becomes apparent, further supporting the observations of a nugget effect present in this study.

As only a sparse dataset exists so far on the abundances of the HSEs in BIFs, this study significantly enhances this dataset. However, at present, no general trends can be observed between the BIFs, their age, and their HSEs contents, implying the need for more follow-up studies on other BIFs to fully assess the HSE budgets in BIFs of different ages.

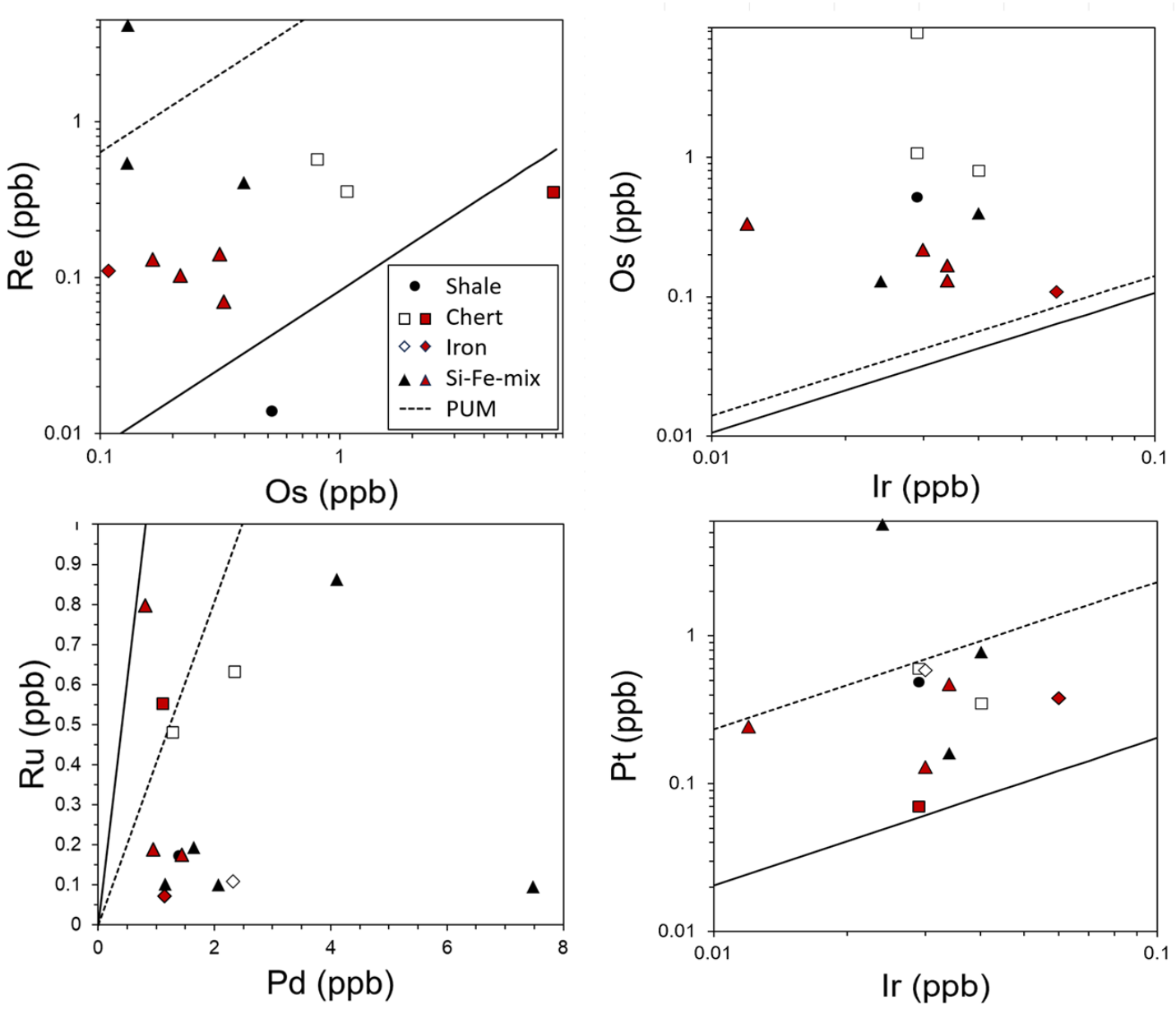

Figure 4.1: *Chosen interelement plots of highly siderophile elements. Black circles represent the shale, white squares the chert, white diamonds the iron samples and black triangles the mixed Si-Fe-mix samples. Samples in red are those which were selected for the construction of a regression line (see Chapter 5.2). The dashed line represents the UCC ratios as a trend (data from Peucker-Ehrenbrink and Jahn 2001); the solid black line represents CI chondrite ratios as a trend (data from Fischer-Gödde et al., 2010).*

4.2 Re-Os isotopic system

The measured isotopic ratios of $^{187}Os/^{188}Os$ and $^{187}Re/^{188}Os$ together with the re-calculated initial $^{187}Os/^{188}Os$ ratios, are presented in Table 2. As for three of the 15 samples (DM22D2, DM22B2 and DM90-2) the Os content and its isotopic ratios were not measured, only 12 samples can be discussed. The measured $^{187}Re/^{188}Os$ ratios vary from ~0.13 to ~155, while $^{187}Os/^{188}Os$ ratios vary between ~0.13 to ~0.41. Initial $^{187}Os/^{188}Os$ ratios (or $^{187}Os/^{188}Os_{(i)}$, calculated using an age of ~3.51 Ga; Mukhopadhyay et al., 2008) vary between ~-9.10 to ~0.40. Four of the initial ratios are negative and thus geologically meaningless. Interestingly, $^{187}Os/^{188}Os_{(i)}$ ratios for six out of the 12 samples cluster around the value of the PUM (~0.13; Becker et al. 2006), as can be seen in Figure 4.2, with values between ~0.10 to ~0.15. These six samples with PUM-like initials are highlighted in red in Figure 4.1 and 4.2 and marked in bold in Tables 2 and 3. These samples are discussed in more detail below.

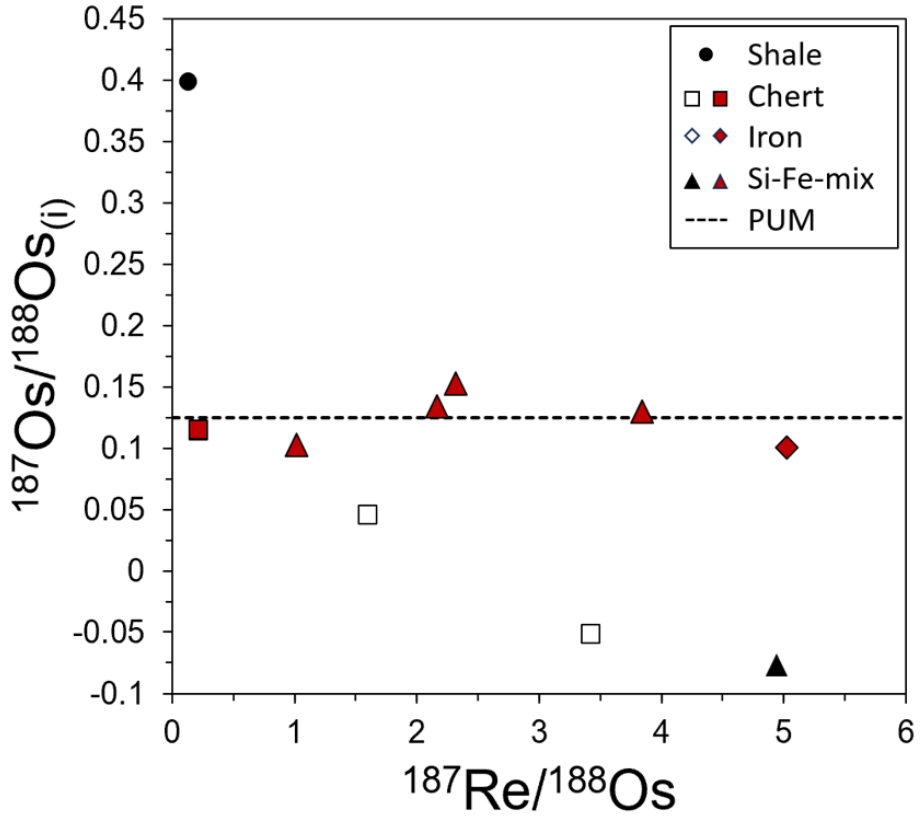

Figure 4.2: *Plot of the $^{187}Os/^{188}Os_{(i)}$ values vs. the $^{187}Re/^{188}Os$ values of 10 samples. Two samples have anomalously high $^{187}Re/^{188}Os$ ratios were omitted to maintain clarity. Six samples, highlighted in red, indicate PUM-like (black dashed line) Os initial ratios, which are discussed later*

The $^{187}Re/^{188}Os$ ratios in BIFs from the literature, Urucum BIF and Temagami BIF, have generally higher values (i.e., more radiogenic) than the studied Tomka BIF samples.

The isotope ratio of the Urucum BIF varies between ~0.25 to ~226 (Prost et al. 2024) and for the Temagami BIF from ~0.61 to ~183 (Schulz et al, 2021). The $^{187}Os/^{188}Os$ ratios for these vary from ~0.14 to ~3.10 in the Urucum BIF and from ~0.17 to ~10.8 in the Temagami BIF, further indicating more radiogenic signals compared to the studied Tomka BIF. Their $^{187}Os/^{188}Os_{(i)}$ ratios have values between ~-6.07 to ~1.64, in the case of the Urucum BIF, and from ~-2.17 to ~2.93 for the Temagami BIF. Both BIFs, similar to this study, calculated some negative, geologically meaningless initial ratios, but some values also record PUM-like ratios (Schulz et al., 2021; Prost et al., 2024). The YMS ironstone have the lowest, but most consistent $^{187}Re/^{188}Os$ and $^{187}Os/^{188}Os$ values of the studies presented, ranging from ~0.35 to ~2.35 for the $^{187}Re/^{188}Os$ ratios and from ~0.61 to ~0.66 for the $^{187}Os/^{188}Os$ ratios. For the back-calculated $^{187}Os/^{188}Os_{(i)}$ ratios, ranging from ~0.58 to ~0.64, no values present negative ratios, but also do not record any values around the PUM $^{187}Os/^{188}Os_{(i)}$ ratio (~0.13; Becker et al., 2006) (Chu et al., 2023).

Discussing the different lithologies in detail, it is noted that the chert layer has the, on average, lowest $^{187}Re/^{188}Os$ (~0.14), $^{187}Os/^{188}Os$ (~1.74) and $^{187}Os/^{188}Os_{(i)}$ ratios (~0.04). As the $^{187}Re/^{188}Os$ ratio and thus the $^{187}Os/^{188}Os_{(i)}$ ratio was determined for only one iron sample, broader comparisons with other lithologies are limited, similar to the HSE data. The $^{187}Os/^{188}Os$ ratios of the iron samples have higher values than the other lithologies, from ~0.19 to ~0.40, but more iron samples would have to be studied for better comparison. As for the mixed samples, they present a distinct increase in their $^{187}Re/^{188}Os$ ratios, varying from ~1.02 to ~155. The $^{187}Os/^{188}Os_{(i)}$ ratios for the mixed samples present an interesting pattern. Either the values are negative, which is the case for three of the mixed samples, or they cluster around the $^{187}Os/^{188}Os$ of the PUM, varying between ~0.10 to ~0.15 (Figure 4.2).

As previously mentioned, lithology-based comparisons within the Tomka BIF are challenging due to the limited number of iron and chert samples, as well as the potential influence of the nugget effect.

In conclusion, it can be stated that for its HSE budget, as well as for its Re-Os isotope signature, the Tomka BIF samples analyzed in this study do not deviate from the literature BIF trend. They do deviate from the presented ironstone data, which could be explained by differences in formation and composition. However, what makes the Tomka BIF unique is its comparatively unradiogenic nature.

5 Discussion

5.1 Syn- and post-depositional alterations

5.1.1 Reliability of Re-Os isotope system in the Tomka BIF

Similar to other already established geochemical proxies for tracing the atmospheric and oceanic O_2-levels, the Re-Os isotope system may provide additional inside into long-term paleo-environmental changes (Stein and Hannah, 2014; Lu et al., 2017, 2018; Liu et al., 2021; Yin et al., 2023). As mentioned above, Re and Os are redox-sensitive elements, being insoluble in reducing- and soluble under oxidizing conditions. An enhanced rate of oxidative weathering of continental crust might thus cause an increased input of radiogenic ^{187}Os to the seawater or of Re, which, over time, lead to a considerable ingrowth of ^{187}Os. This cause-and-effect relationship could potentially be archived in ancient seawater precipitates, such as banded iron formations, which then could be expected to be variably radiogenic depending on their age and oxygen levels at the time of their precipitation. Although the Re-Os-isotope system in principle provides a suitable paleo-redox proxy (Stein and Hannah, 2014; Peucker-Ehrenbrink and Ravizza, 2020; Yin et al., 2023) and the secular evolution trend of seawater $^{187}Os/^{188}Os$ is well reconstructed for the more recent geological history, including the Cenozoic and late Mesozoic (Peucker-Ehrenbrink and Ravizza, 2000; Ravizza and Peucker-Ehrenbrink, 2003; Klemm et al., 2008; Robinson et al., 2009; Katchinoff et al., 2021), this system, so far, was only rarely applied to Precambrian (especially Archean) marine sediments. Such sediments mainly include organic-rich material (e.g., Lu et al., 2017) and only few examples of iron formations (e.g., Cohen et al., 1999; Selby and Creaser, 2003, 2005; Stein and Hannah, 2014; Kendall et al., 2015; Schulz et al., 2021; Prost, 2023; Chu et al., 2023). However, extending the $^{187}Os/^{188}Os$ seawater evolution trend into the Precambrian would be highly valuable for deciphering Os-isotopic fluctuations of ancient seawater, which could be used to track paleoenvironmental conditions (e.g., crustal growth, changing weathering conditions, asteroidal bombardment etc.). As this approach is limited by the availability of reliable seawater archives from that time, a comparably scarce dataset accumulated so far for the Paleoproterozoic and early Mesoproterozoic (Stein and Hannah, 2014; Lu et al., 2017; Peucker-Ehrenbrink and Ravizza, 2020) accompanied by a near complete lack of such data for the Archean (Schulz et al., 2021; Chu et al., 2023). A prerequisite for the

interpretation of any Re-Os isotope data of ancient seawater precipitates, including iron formations, is if they still represent pristine seawater signals. Syn- and/or post-depositional alteration could have obscured, overprinted or erased primary signatures and must be discussed, especially for Archean samples. Such processes might have inevitably altered pristine geochemical signatures, but their extent needs to be evaluated and if all constituents of a given rock (in the case of BIFs, for example, chert- and iron-rich samples) were affected to the same degree. This can often be implemented by geochemical screenings for detritus contamination (i.e., syn-depositional alteration) or hydrothermal overprint (i.e., post-depositional alteration).

5.1.2 Syn-depositional alterations

The process usually ascribed to syn-depositional alteration is detrital aluminosilicate contamination, which might have preferentially have affected iron formations precipitated under shallow-water conditions, arguably near shores of the continental hinterland (Viehmann et al., 2015b; Viehmann, 2016). Since REEs abundances in the UCC are typically orders of magnitude higher than those in seawater (e.g., Ce: ~0.8 ppb in seawater, ~63 ppm in UCC; Sm: ~0.6 ppb in seawater, ~5 ppm in UCC; Nd: ~3.1 ppb in seawater, ~27 ppm in UCC (Parekh et al., 1977; Peucker-Ehrenbrink and Jahn, 2001; Douville et al., 2002), any significant enrichment of REEs in BIFs that correlate with the abundances of immobile elements such as Al and Zr, and other high-

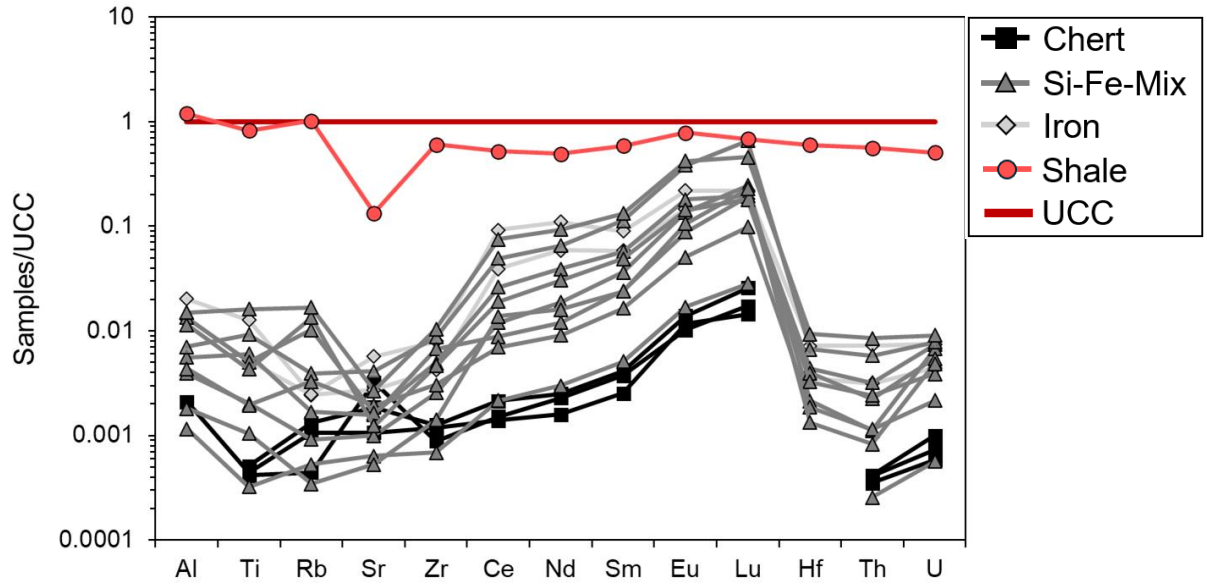

Figure 5.1: *Comparison of UCC-normalized trace element data from the Tomka BIF samples. Highlighted in orange is the shale sample, which is interpreted to represent the detrital endmember. Data for UCC (dark red line) from Peucker-Ehrenbrink and Jahn (2001) and trace element data from Kienle (2024).*

field-strength elements (HFSEs) – commonly associated with clastic detritus input – strongly suggests detrital contamination (e.g., Bau, 1993). In contrast, if elevated REEs (i.e., supracrustal) concentrations in BIFs do not correlate with Al or Zr, the enrichment is more likely attributed to authigenic precipitation from ancient fluids. Positive europium anomalies and flat or heavy REE (HREE) enriched patterns are often used as indicators of hydrothermal influence (Bau, 1991; Danielson et al., 1992; Viehmann et al., 2015a).

The same approach might be applied to Re and Os. Elevated Re and Os concentrations in BIFs, particularly when positively correlated with Al and Zr, indicate a detrital source since these elements are also more concentrated in crustal material than in seawater (Re: ~0.006 to ~0.01 ppt in seawater, ~198 ppt in UCC; Os: ~7.2 to ~7.4 ppt in seawater, ~31 ppt in UCC; Anbar et al., 1992; Woodhouse et al., 1999; Peucker-Ehrenbrink and Jahn, 2001). However, if Re and Os enrichments in BIFs have no correlation with immobile elements, they may reflect an authigenic seawater-derived signal. In such cases, hydrothermal vent systems – especially prevalent during the Archean – could have contributed significant amounts of Re and Os to the oceans, which were subsequently incorporated into the precipitating BIFs.

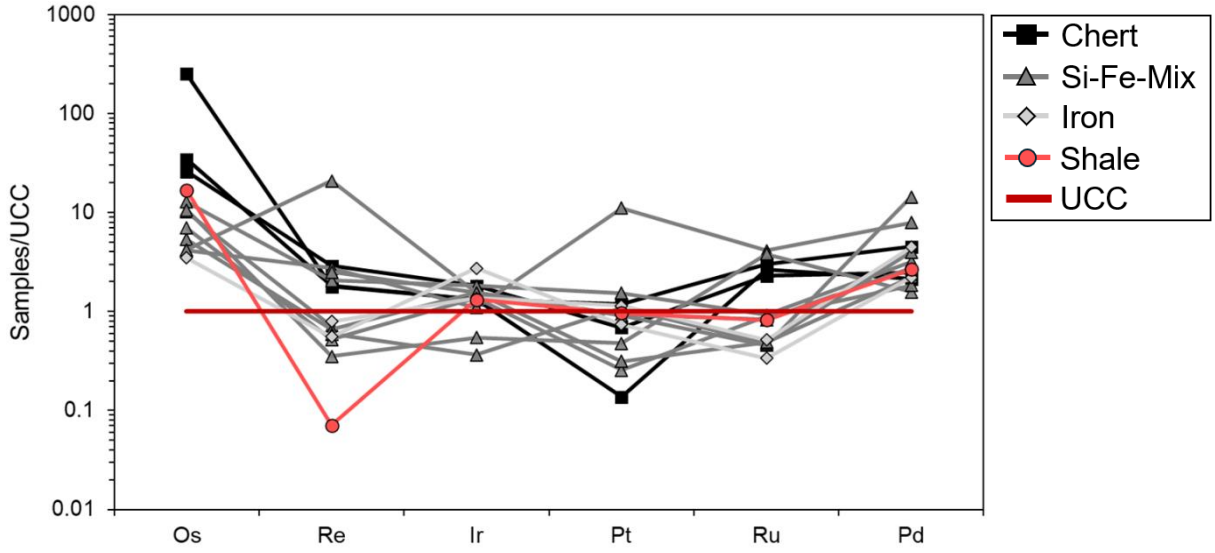

Figure 5.2: *Comparison of UCC-normalized highly siderophile element data from the Tomka BIF samples. Highlighted in orange is the shale sample, which is interpreted to represent a detrital endmember. Data for UCC (dark red line) from Peucker-Ehrenbrink and Jahn (2001).*

Assuming that any detrital aluminosilicate addition to the Tomka seawater basin (from which the Tomka BIF precipitated) were derived from continental hinterland and using today's (UCC-) composition as a detritus proxy, would imply elemental signatures in the Tomka BIF samples to be successively less fractionated with increasing detrital contamination in UCC-normalized element diagrams. Figure 5.1 illustrates similar

pronounced fractionation trends defined by selected trace elements for all analyzed Tomka BIF samples, and as previously mentioned, chert-rich samples present significantly lower concentrations compared to iron-rich samples (with lithology-mixes plotting mostly at intermediate values). Notably, the shale-rich sample (DM71A) is significantly less fractionated, presenting a flat trace element pattern (except the fluid mobile Sr; see discussion Chapter 5.1.3), which mirrors UCC and arguably represents a detrital endmember sample. These relationships can be interpreted in terms of minor syn-depositional (detrital) alteration in the Tomka BIF samples, with regards to selected trace elements illustrated in Figure 5.1.

However, HSE patterns of the Tomka BIF samples (Fig. 5.2) express a more ambiguous picture about possible detrital contamination. Despite some differences in the Re and Os abundances, the shale sample DM71A – similar to the trace element abundances illustrated in Figure 5.1 – mirrors the UCC trend and might represent a better proxy for a pure detritus HSE signature than present-day UCC. However, the HSE pattern of iron-, chert-, and mixed samples scatter around the UCC value with little to no systematic fractionation trend between the samples. As previously mentioned, syn-depositional alteration (i.e., detritus contamination) cannot be adequately evaluated by only analyzing this diagram alone, thus a closer examination of some fluid-immobile elements - such as Al and HFSEs (i.e., Zr, Ti and Hf) - which are typically enriched in detrital input and depleted in marine sediments, is required. In particular, their correlation with HSE concentrations and ^{187}Os isotope signatures warrants further investigation.

In plots of HFSEs versus Re (Figure 5.3b and A3b in Appendix) and Os concentrations (Figure 5.3a and Figure A3a in Appendix) as well as $^{187}Os/^{188}Os$ ratios (Figure 5.3c and Figure A3c in Appendix) the Tomka BIF samples present highly variable Re and Os abundances and $^{187}Os/^{188}Os$ ratios at, more or less, constant Al and other HFSE abundances for all three Tomka lithologies (iron, chert and mixed samples), while the shale sample (postulated detritus endmember) always plot at significantly higher Al and HFSE concentrations. These results suggest that detrital admixture in the Tomka BIF is negligible. Any substantial detrital contamination would result in apparent positive correlations between the shale sample and a hypothesized detritus-free seawater signal (with near zero HFSE contents). However, this cannot be observed; instead, a trend can be identified which indicates increasing contamination by detritus.

It is important to note that, although the “trend” suggests increasing detrital input, the actual Al and Zr concentrations are roughly two orders of magnitude lower in the actual detritus. This difference is visually compressed by the logarithmic scale. In contrast, when only taking the isochronous samples into account, no trend is observed. This is supported by analyzing the r^2 values of the isochronous data points, which all have values below 0.5, indicating an absence of correlation.

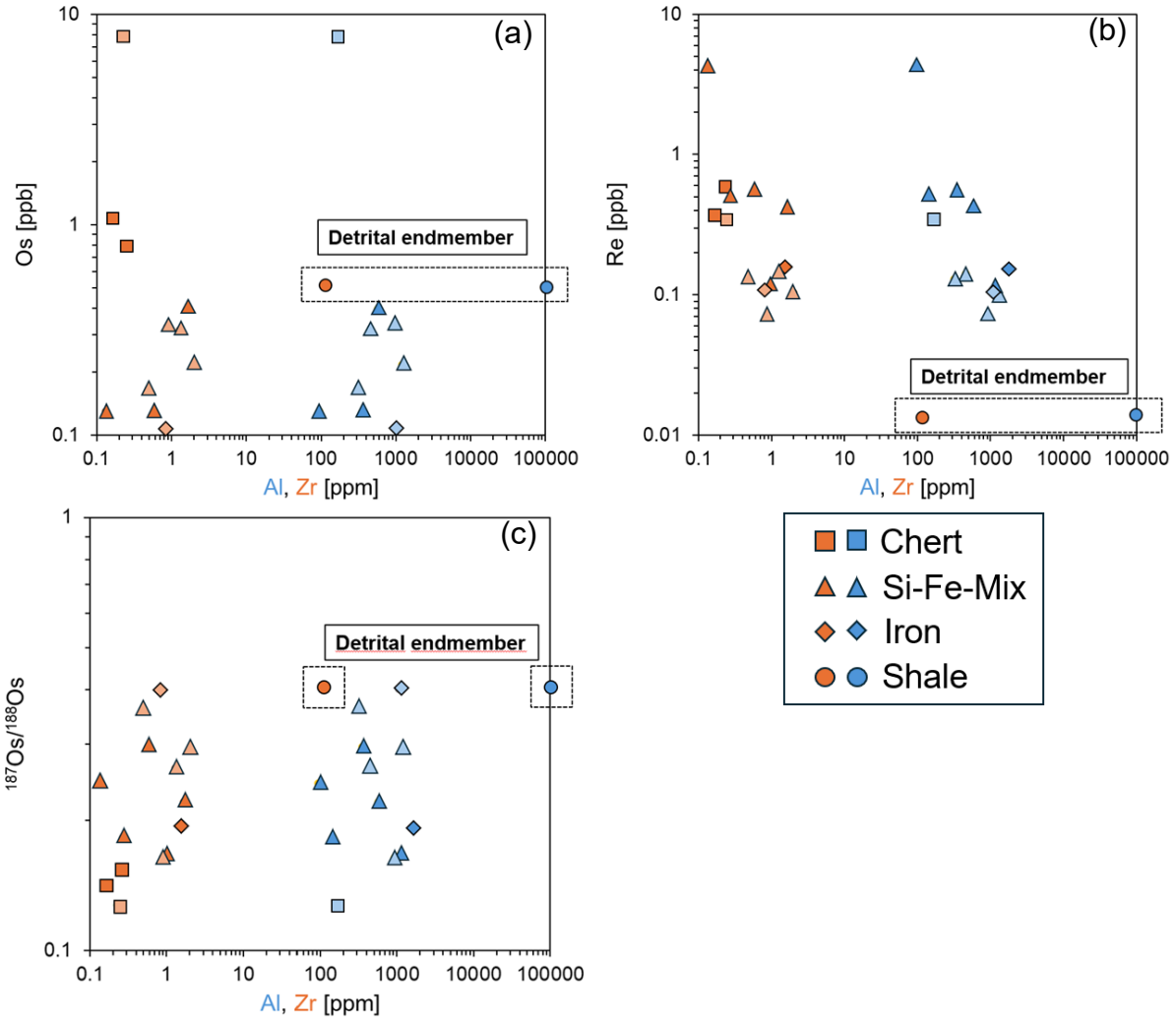

Figure 5.3: *Diagrams of (a) Os concentration, (b) Re concentration, and (c) the $^{187}Os/^{188}Os$ ratios plotted vs. Al and Zr concentrations of the Tomka BIF samples. Samples in lighter color-scales indicate those with a PUM-like initial $^{187}Os/^{188}Os$ ratio (see discussion). For some samples, Os or Al could not be measured (Os: DM22D1, DM22B2 and DM90-2; Al: DM17D1 and DM17C2), explaining the different number of data points in the plots. r^2 values of isochronous data points: (a) Al: ~0.3; Zr: ~0.31; (b) Al: ~0.49; Zr: ~0.31; (c) Al: ~0.11, Zr: ~0.04.*

Despite this, and taking all variations depicted in Figure 5.3 into account, a detrital contribution to the Tomka BIF, if existent, is minor. This conclusion, of a non-significant detrital contamination, can be further strengthened by comparing it to other BIFs of different ages. Some of them have significantly higher Al and Zr concentrations

compared to the Tomka BIF sample yet were postulated to represent pristine seawater composition. Samples from the Neoproterozoic Urucum BIF, for example, have Al contents of up to 1.5 wt.% but demonstrate isochronous Re-Os behavior, arguing for an absence of significant detritus contamination (Prost et al., 2024). Samples from the Mesoarchean Witwatersrand BIF, on the other hand, have Zr contents of up to 15 ppm and were interpreted to demonstrate a closed system behavior (Viehmann et al., 2015b). It should be noted that trends of constant and comparably low immobile element concentrations at diverse HSE abundances and $^{187}Os/^{188}Os$ signatures, as advocated above, also persist when their abundances are normalized to the Fe concentrations of the samples, which accounts for the mineralogical effects between the different lithologies (Figure A4a-c and Figure A5a-c in Appendix).

To further strengthen the interpretation of non-significant syn-depositional alteration, Kienle (2024) advocated that samples from the Tomka BIF (which in part were also analyzed in this study), when compared to other Precambrian BIFs from the Moodies Group (~3.22 Ga; Heubeck et al., 2013; Bonnand et al., 2020), Pietersburg (~2.95 Ga; De Wit et al., 1993; Alexander et al., 2009) and Witwatersrand (~2.90 Ga; Viehmann et al. 2015), have superchondritic Y/Ho ratios and other REY features that can be interpreted as proxies for pure marine Precambrian chemical sediments (Bau et al., 1995, 1996; Bolhar et al., 2004; Alexander et al., 2009; Viehmann et al., 2015b; Bonnand et al., 2020). These observations point towards a lack of significant detrital contamination. In a Y/Ho vs. Zr diagram (Figure A6 in Appendix), Kienle (2024) summarized the usefulness of the Tomka BIF samples as unique geochemical archives for REY signatures.

Collectively, the data presented here, while establishing the Tomka shale sample DM71A as a hypothetical detritus endmember, argue against significant syn-depositional alteration of the chert-, iron-, and mixed Tomka BIF samples.

5.1.3 Post-depositional alteration

Post-depositional alteration involves fluid-rock interaction that could alter the pristine seawater signal of marine precipitates during diagenesis, metamorphism, hydrothermal alteration or weathering after exhumation (Konhauser et al., 2017). As post-depositional alteration can affect the Re-Os isotopic system, the identification and exclusion of post-depositionally altered and detritus-free Tomka BIF samples is a

prerequisite for the identification of seawater signals and for a discussion of their chronological significance.

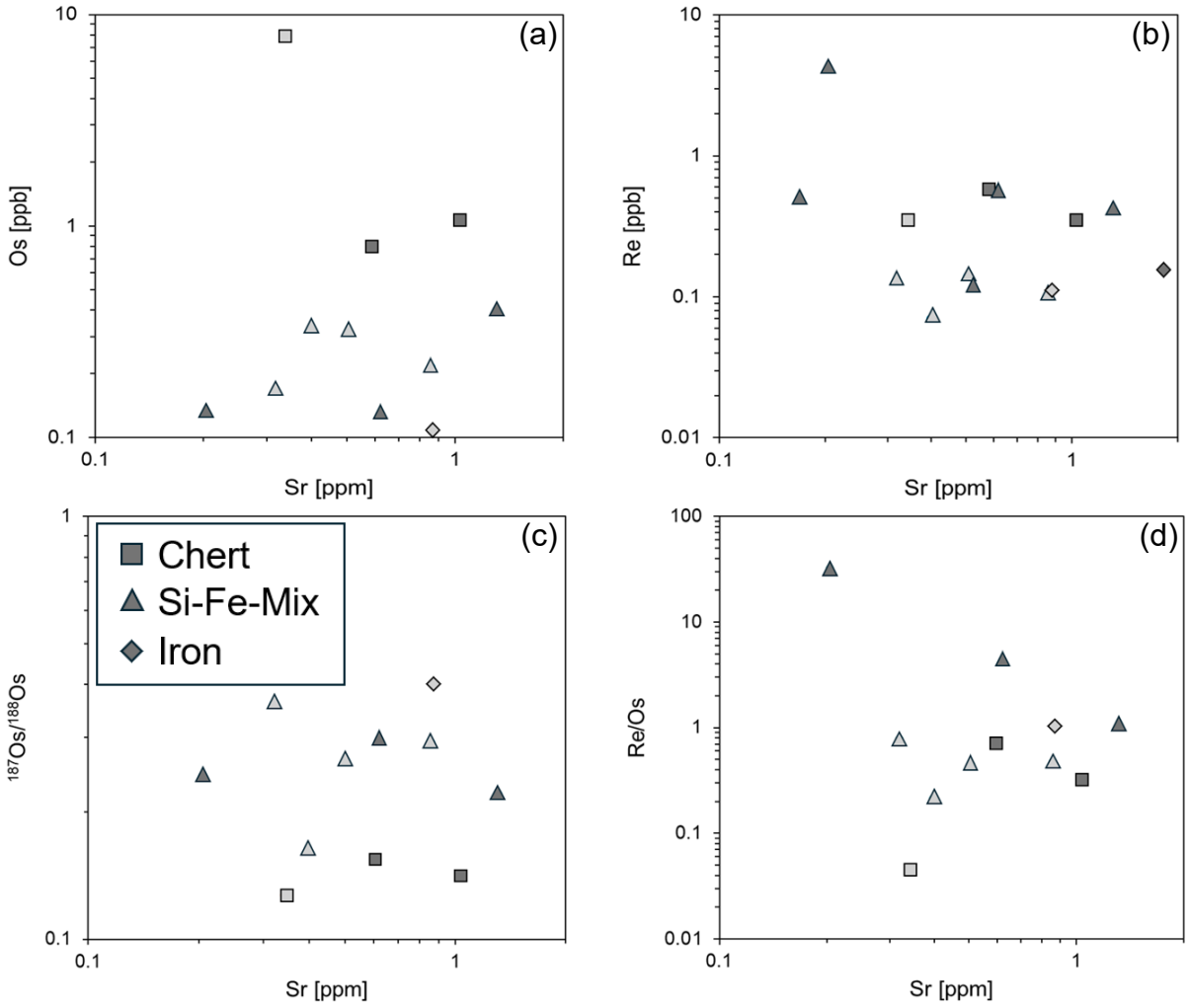

Figure 5.4: *Diagrams of (a) Os concentration, (b) Re concentration, (c) the $^{187}Os/^{188}Os$ ratios, and (d) the Re/Os ratios vs. Sr concentrations of the Tomka BIF samples (excluding the shale sample). Samples in lighter color-scale indicate those with a PUM-like initial $^{187}Os/^{188}Os$ ratio (see discussion). For some samples, the Os concentration (DM22D1, DM22B2 and DM90-2) could not be measured, explaining the different numbers of data points the plots. r^2 values of isochronous data points: (a): ~0.17; (b): ~0.16; (c): ~0.30; (d): ~0.27.*

While the Re-, Os- and $^{187}Os/^{188}Os$ vs Al and Zr diagrams in Chapter 5.1.2 likely confirm an insignificant influence of detritus contamination of the analyzed Tomka samples with respect to HSEs, a possible influence of post-depositional alteration on the HSE budget can be evaluated by comparison to fluid-mobile elements like Sr, for which literature data is available (e.g., Schulz et al., 2021; Prost et al., 2024). Strontium is a large ion lithophile element, which is considered mobile during fluid transport. Paired with the co-variation of the Sr-concentration and its radiogenic isotope composition in water, its characteristics make Sr an excellent tracer for fluid-rock

interactions during diagenetic processes (e.g., Nebel, 2016). As a mobile element, Sr is leached from the rock during interaction with a fluid, while the fluid, in turn, provides additional elements that are incorporated into the chemistry of the rock. Correlations of Sr concentrations in samples from a marine chemical sediment with Re, Os, and/or $^{187}Os/^{188}Os$ ratios, could, thus, in principle be interpreted as an indicator for significant fluid-rock interactions.

Figure 5.4a-d depicts plots of Os- and Re concentrations, as well as $^{187}Os/^{188}Os$ and the Re/Os ratios versus Sr concentrations. Correlations can be observed for both the Os vs. Sr and the Re vs. Sr datasets. With higher Sr concentrations the Os values also increase, while the opposite trend can be seen for Re; as Sr concentrations increase, the Re values decrease. However, this correlation is less significant for Re than for Os. As mentioned previously, Sr is known to be fluid-mobile. In general, Os is interpreted to be less fluid-immobile (Barnes et al., 1985; Woodland et al., 2002), compared to Re (Xiong and Wood, 1999, 2000). This is as odds with the observed results, where the Os content negatively correlates with that of Sr, while Re presents the opposite trend (although less apparent).

Interestingly, when normalized to Fe (see Figure A7a-d in the Appendix), both diagrams, (a) Os vs Sr/Fe and (b) Re vs Sr/Fe, indicate a positive correlation. Furthermore, the Tomka BIF samples with a PUM-like initial $^{187}Os/^{188}Os$ ratio (lighter gray color in Figure 5.4 and A7a-d in Appendix) tend to plot in the Sr-depleted area of the diagram, independent of the different lithologies (except chert sample). This area could either represent the least (post-depositionally) altered side of the diagram and, thus, the authigenic seawater signal, or it is just a normalization artifact that results from differentiating iron-rich (iron, and mixed samples) from iron-poor samples (chert). When plotting the Fe content against the Sr concentration (see Figure 5.5) it appears that the apparent trend in Sr/Fe ratios (Appendix Figure A7a–d) is largely an artifact of Fe variability, as Sr concentrations remain relatively constant while Fe content varies considerably. However, similar to the observed trend in Chapter 5.1.2, when only looking at the isochronous samples, no correlation can be found between the data points. This is supported by their respective r^2 values, which are all <0.5.

Some literature BIF studies, such as for the Temagami BIF (Schulz et al., 2021) reported minor to no post-depositional alterations, whereas the Urucum BIF (Prost et al., 2024) records evidence of at least some degree of post-depositional modification. Despite these differences, both BIFs present distinctly higher Sr concentration

(Temagami BIF: 3.42-266 ppm; Urucum BIF: 12.3-331 ppm) compared to the Tomka BIF; also, their Re and Os concentrations are within ranges similar to those of the Tomka BIF.

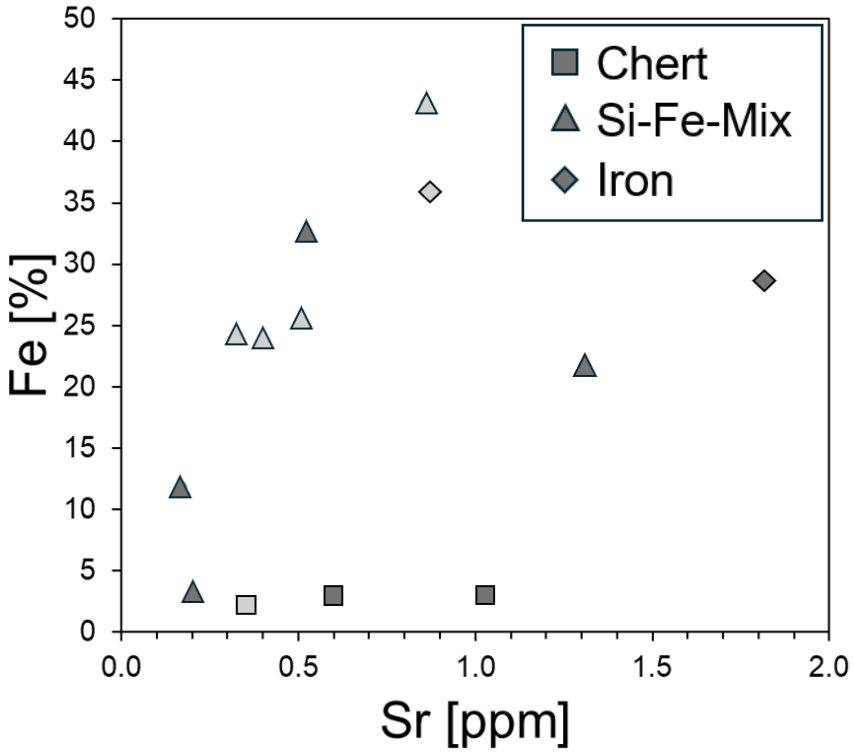

Figure 5.5: *Diagram of Fe concentration (in %) vs. Sr concentration (in ppm) of the Tomka BIF samples. Samples in lighter color-scale indicate those with a PUM-like initial $^{187}Os/^{188}Os$ ratio. Sample IND-DGB-BIF2 5 is not included as no Fe concentration was measured.*

However, post-depositional alteration could result in apparent correlations between Re and Os versus Sr, which could be positive or negative, depending on which elements are added or leached from the rock. While positive trends (Appendix Figure A7a-b) rather suggest a common transport or coupled mobility of Os, Re, and Sr during alteration, mixed trends (as in Figure 5.4) for Re and Os might argue for a decoupling of Re and Os transport during fluid-rock interaction. Alternatively, the system may have remained closed with respect to Re, Os, and Sr, and that any possible correlations reflect primary (pre-alteration) mineralogical relationships. This cannot be finally solved based on the available data.

5.2 The Re-Os isotope signatures in the Tomka BIF and their possible implications

5.2.1 Os isotopic initial values and attempt of direct age determination

As discussed in the preceding chapters, it can be assumed that the analyzed Tomka BIF samples are free or insignificantly affected by detrital contamination and likely variably affected by post-depositional processes, depending on the scenarios outlined above. Although a closed Re-Os isotope system might be unlikely for the Tomka BIF samples analyzed in this study, in this chapter I discuss to which extent this system was disturbed and if any geochronological information can still be extracted from the data; possible paleoenvironmental signatures are discussed in Chapter 5.3.

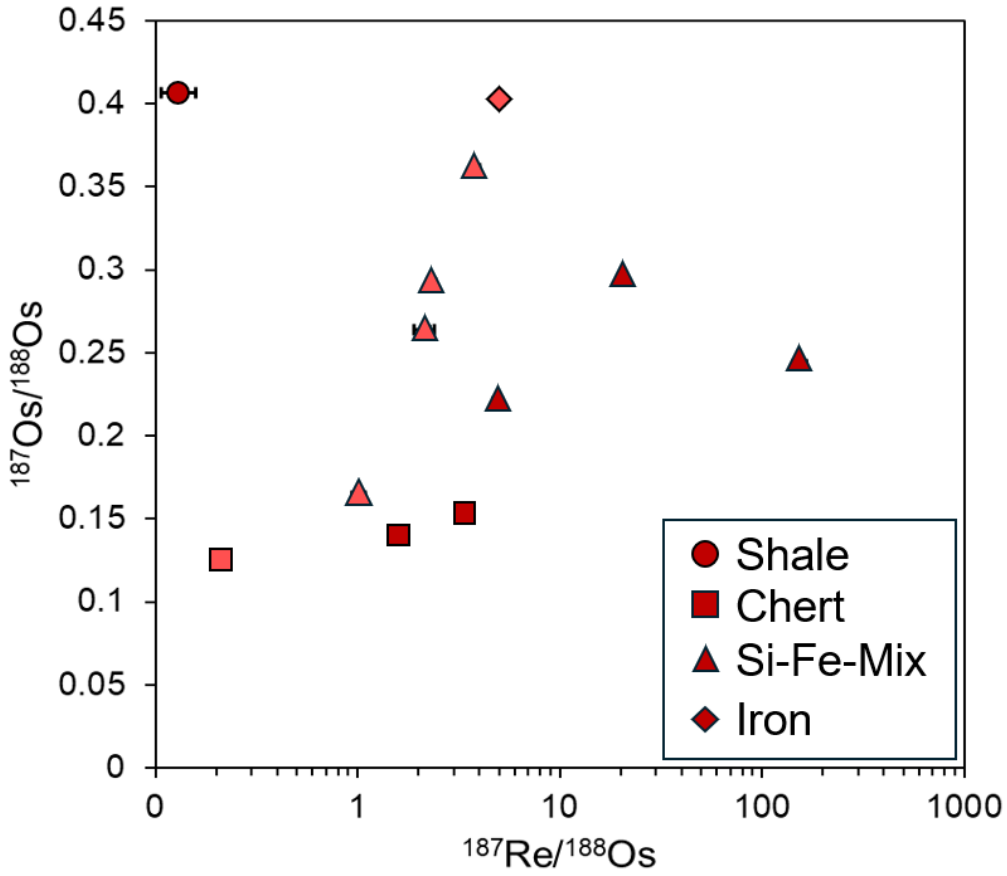

Figure 5.6: *$^{187}Os/^{188}Os$ vs. $^{187}Re/^{188}Os$ for all samples of the Tomka BIF (excluding DM22D2, DM22B2, and DM90-2, for which the $^{187}Re/^{188}Os$ ratio could not be measured). Overall, the samples present a trend of an increasing $^{187}Re/^{188}Os$ ratio with increasing $^{187}Os/^{188}Os$ ratio. Samples in lighter color-scale indicate those with a PUM-like initial $^{187}Os/^{188}Os$ ratio.*

In Figure 5.6, $^{187}Os/^{188}Os$ ratios are plotted against $^{187}Re/^{188}Os$ ratios for the measured samples. Despite considerable scatter, the samples present an overall trend of increasing $^{187}Os/^{188}Os$ ratios with increasing $^{187}Re/^{188}Os$ ratios, as can be expected for

any closed Re-Os isotope system (with increasing radiogenic ^{187}Os ingrowth with increasing Re content). The scatter of these samples is, however, significant resulting in a geological meaningless age, which is not discussed here.

As explained in Chapter 4.3, several of the back-calculated $^{187}Os/^{188}Os_{(i)}$ values strongly deviate from the PUM $^{187}Os/^{188}Os$ ratio of ~0.13 (Becker et al., 2006), leading to in some cases negative and, thus, geologically meaningless values. However, six of those initial ratios (see Figure 5.7) have values around the PUM $^{187}Os/^{188}Os$ ratio.

These six samples with PUM-like initial values, averaging at a $^{187}Os/^{188}Os_{(i)}$ ratio of 0.12 ± 0.02 (compared to the PUM isotopic ratio of approximately ~0.13), were thus selected as prime candidates in an attempt to construct a linear regression.

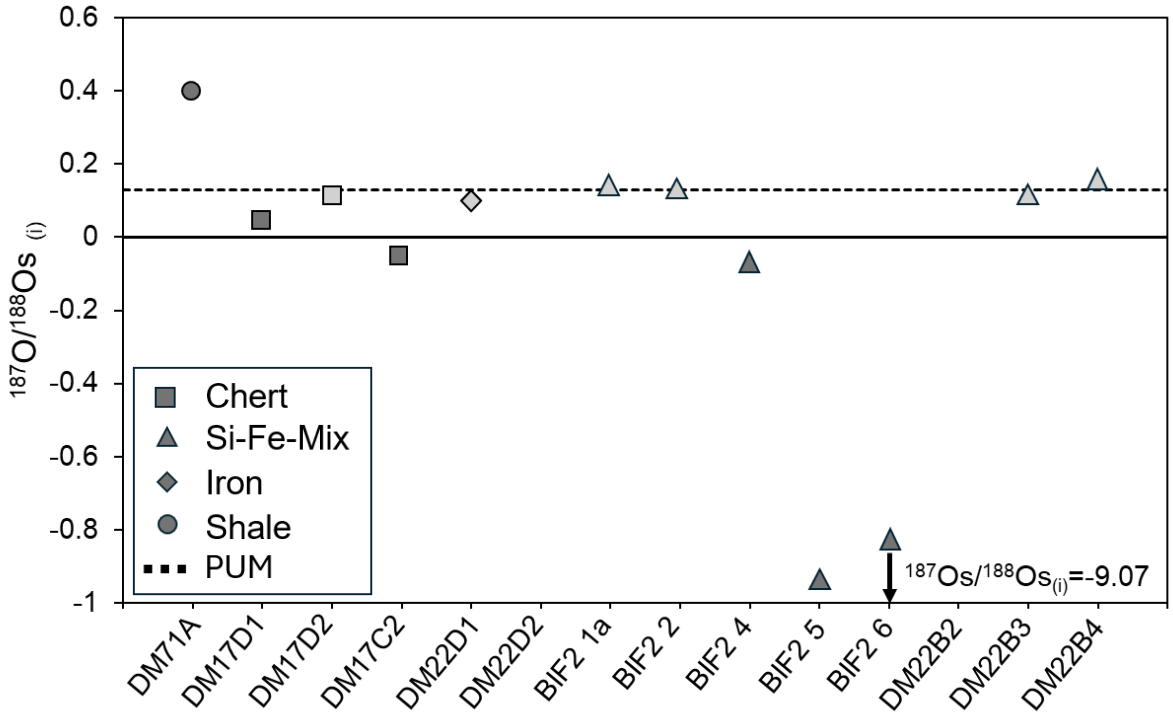

Figure 5.7: *Plot of the back-calculated initial $^{187}Os/^{188}Os$ concentrations of the Tomka-BIF samples. The dashed line represents the PUM $^{187}Os/^{188}Os$ and thus the samples in lighter color shade represent those with an isochronous initial. For samples DM22D2, DM22B2, and DM90-2 no initial could be calculated.*

In Figure 5.8, this first attempt is depicted, using those six samples to define a regression line that corresponds to an age of 3,878 ± 794 Ma. Due to significant scatter in the data, the smaller calculated uncertainty of ± 210 Ma is not used here, as it does not adequately account for the observed over-dispersion in the dataset. A detailed explanation of over-dispersion, the associated MSWD (Mean Square of the Weighted Deviates) and $p(\chi^2)$ value (p-value in a chi-square test) is provided in Appendix A1b.

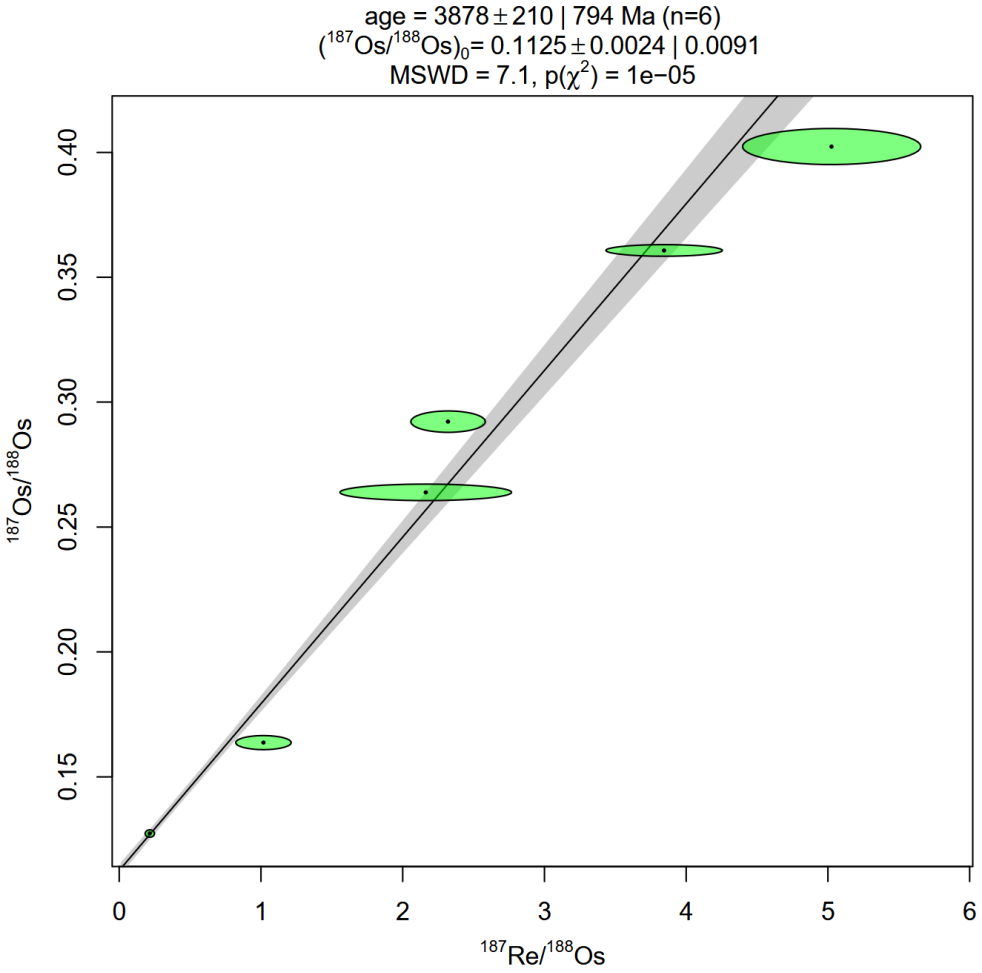

Figure 5.8: *Isochron diagram for the six Tomka BIF samples selected after the criteria discussed in the main text. The regression line defined by these samples corresponds to an age of 3,878 ± 794 Ma, but it indicates overdispersion of the data. Green ellipses around the data points represent the x- and y-errors. The linear regression and the "age" were calculated using the program IsoplotR (version 6.4.2).*

In an attempt to minimize over-dispersion, the data set was further reduced to five samples. This was achieved by further analysis of the samples and examining which of these six samples most likely indicate signs of a detrital and/or hydrothermal input. Among these six samples with a PUM-like $^{187}Os/^{188}Os_{(i)}$ ratio, the Si-Fe-mixed sample DM22B4 has the highest concentrations of not only Al and Zr (Al: ~1291 ppm; Zr: ~2.01 ppm), but also of other HFSE such as Ti (~61.9 ppm) and Hf (~0.05 ppm). It should also be noted that these concentrations of elements indicative of syn-depositional alteration, are not only highest among the six PUM-like samples, but also highest compared to all samples, excluding the shale samples DM71A. Additionally, it has the most radiogenic $^{187}Os/^{188}Os$ initial of the PUM-like samples, at ~0.15. The resulting regression line, as defined by five samples, illustrated in Figure 5.9, corresponds to an age of 3,557 ± 668 Ma.

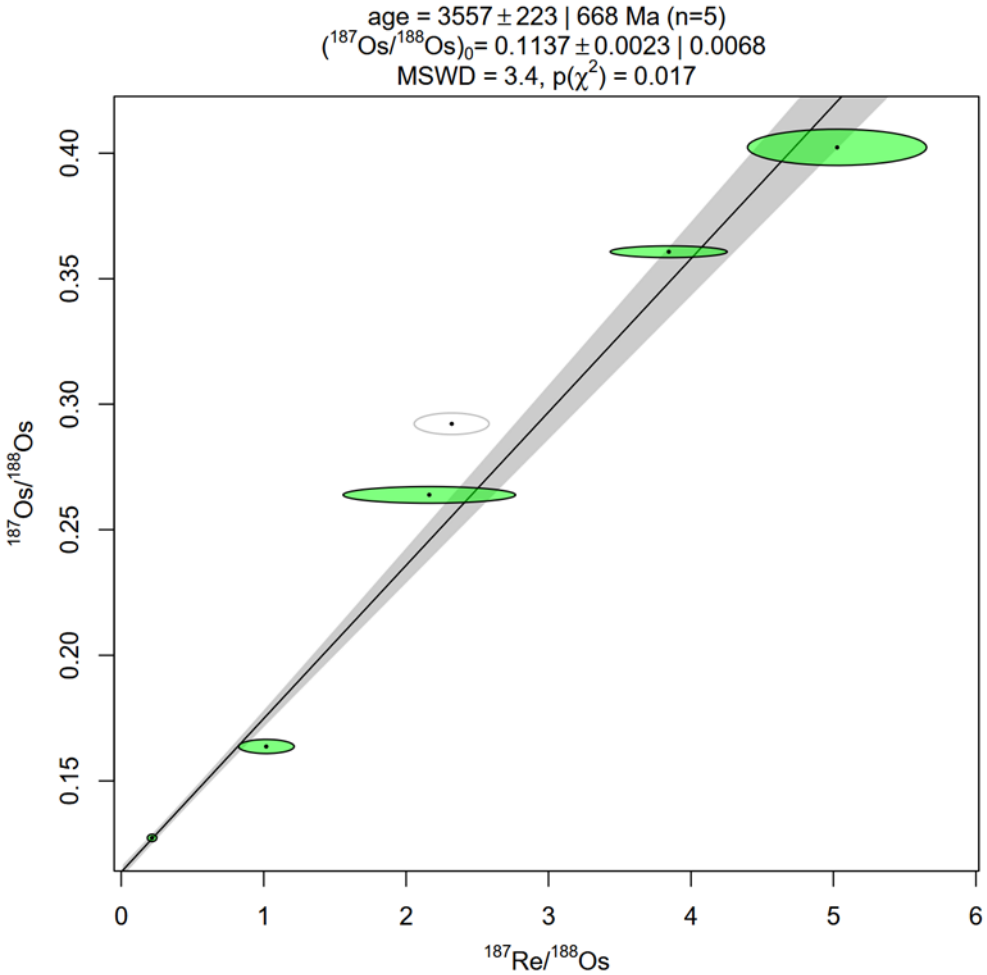

Figure 5.9: *Refined regression line in the Re-Os isochron diagram, considering only five out of the six samples with homogeneous initial $^{187}Os/^{188}Os$. Sample number DM22B4 was not considered, because is has the highest likelihood of syn- and post depositional alteration. A new age has a slightly smaller error of 3,557 ± 668 Ma. Green ellipses around the data points represent the x- and y-errors. The data point with no such error is the sample excluded from the "age" calculation. The linear regression and the "age" were calculated using the program IsoplotR (version 6.4.2).*

The intercept of this regression line with the y-axis corresponds to an initial $^{187}Os/^{188}Os$ ratio of 0.114 ± 0.007. This value is (within uncertainty) almost identical to the value for chondrites (~0.12; Fischer-Gödde et al., 2010), and closely approaches the estimated isotopic composition of the primitive upper mantle (PUM: ~0.13, Becker et al., 2006). In summary, determining a meaningful Re-Os age for the Tomka BIF is challenging due to the age of the sample, the influence of post-depositional alteration, and the resulting (at least in part) open-system behavior. If at least a partly closed system behavior can be assumed for five out of the analyzed 15 samples (due to geochemical reasons outlined above) an age of 3,557 ± 668 Ma can be derived, correlating with an initial $^{187}Os/^{188}Os$ value of 0.114 ± 0.007. The available data and discussion do not allow for a clear determination of whether or not the calculated age is geologically meaningful, nor if it reflects the depositional, or a later metamorphic, age. Based on the large error,

the latter question might be insignificant. The following chapters, however, will argue (i) in favor of a true, albeit rather imprecise, age information by comparison with existing indirect age determinations for the Tomka BIF (Chapter 5.2.2) and (ii) for the true meaning of the corresponding initial $^{187}Os/^{188}Os$ value and that it most plausibly represents a (probably local) authigenic seawater signal at the time of deposition of the Tomka BIF.

5.2.2 Comparison and discussion Tomka BIF age

The discussion outlined above resulted in a Re-Os age estimate, for either the deposition or a subsequent early-stage overprint of the Tomka BIF, of 3,557 ± 668 Ma. The arguments presented above in favor and against true age information (based on geochemical considerations) are complemented here by comparison with literature estimates for the age of the Tomka BIF. These age estimates are based on indirect (between ~3.51 Ga to ~3.28 Ga; Hofmann et al., 2022; Jodder et al., 2023) age estimations, since no direct age estimations are available for the deposition of the Tomka BIF. These (indirect) age constraints for the Tomka Formation were derived from (i) samples from the Talpada Formation, which underlies the Tomka Formation and (ii) from rock samples of intruded granitoids inside the Older Metamorphic Group, which is interpreted to reflect the age of the regional metamorphism in the Badampahar Group, both were derived by using U-Pb SHRIMP zircon dating (Hofmann et al., 2022; Jodder et al., 2023).

The accumulation rates of the different bands, in scale from cm to m in range, of the Tomka BIF imply age differences of a few thousand years between mesobands (using a sedimentation rate of ~1-2 cm/kyr; De Oliveira Carvalho Rodrigues et al., 2019). This variability can affect the precision of age estimates, regardless of the radionuclide system used.

Taking the few literature age estimations of between ~3.51 to ~3.28 Ga as a deposition age into consideration, the calculated age of this study of 3,557 ± 668 Ma is broadly consistent with these prior age constraints, despite the large associated uncertainty. Although this cannot be an argument in favor of a true age estimated based on the regression line in Figure 5.9 (instead of representing a mixing line or simple coincidence), it is not an argument against it as well.

To summarize, the Re-Os model age of 3,557 ± 668 Ma, presented in this study, represents only the third reported attempt at dating banded iron formations (BIFs) using

the Re-Os isotope system, alongside the Archean Temagami BIF (2,661 ± 126 Ma; Schulz et al., 2021) and the Neoproterozoic Urucum BIF (577 ± 38 Ma; Prost et al., 2024). Even though each of these BIFs present only low to moderate degree of metamorphosis (greenschist to lower amphibolite facies), the results suggest that the Re-Os system may have limited robustness as a chronometer for BIFs the further back in time it is applied. This can be observed when looking at the associated uncertainties with each age, which increases with sample age in absolute terms, with the here studied Tomka BIF recording the highest absolute error margin of ± 668 Myr, followed by the Temagami BIF (± 126 Myr) and the Urucum BIF (± 38 Myr).

These results suggest that, while the Re-Os system holds promise for dating younger, less-altered BIFs, its reliability diminishes with age. In this context, the Tomka BIF, as the oldest BIF to date studied by Re-Os geochronology, provides a key endmember for assessing the applicability and limits of this method.

5.3 Os Seawater evolution curve in the Archean

Even though the linear regression of the $^{187}Os/^{188}Os$ vs. $^{187}Re/^{188}Os$ diagram likely does not represent an isochrone and thus a meaningful geological age, it is still possible that the y-axis intercept of the regression diagram (0.114 ± 0.007) could represent the initial $^{187}Os/^{188}Os$ ratio and thus an authigenic seawater signal of the Archean. This value falls well within the PUM-like $^{187}Os/^{188}Os_{(i)}$ ratio ranges reported for the Archean Temagami BIF (0.12 ± 0.10; Schulz et al., 2021), and the Neoproterozoic Urucum BIF (0.122 ± 0.003; Prost et al., 2024). However, it remains uncertain whether (i) the $^{187}Os/^{188}Os_{(i)}$ ratios reported in these three BIF studies truly represent a pristine global seawater signal or merely local excursions within the deposition basin, and (ii) whether comparisons between $^{187}Os/^{188}Os_{(i)}$ ratios derived from BIFs and organic-rich mudrocks (ORMs) are valid. In the compilation of $^{187}Os/^{188}Os_{(i)}$ ratios (Figure 5.10), adapted after Peucker-Ehrenbrink and Ravizza (2020) and primarily based on ORMs, the value of the Urucum BIF, for example, is distinctly lower than of the coeval ORMs in the Neoproterozoic. This could be explained, as mentioned before, by the signal not representing a global seawater Os isotope composition, but just the signal of the unradiogenic local deposition basin of the Urucum BIF (Prost et al., 2024). It could also be caused by the differences between BIFs and ORMs in their deposition mechanisms and settings. To resolve these

uncertainties, additional studies on the Re-Os isotope composition of BIFs across a range of different ages are needed.

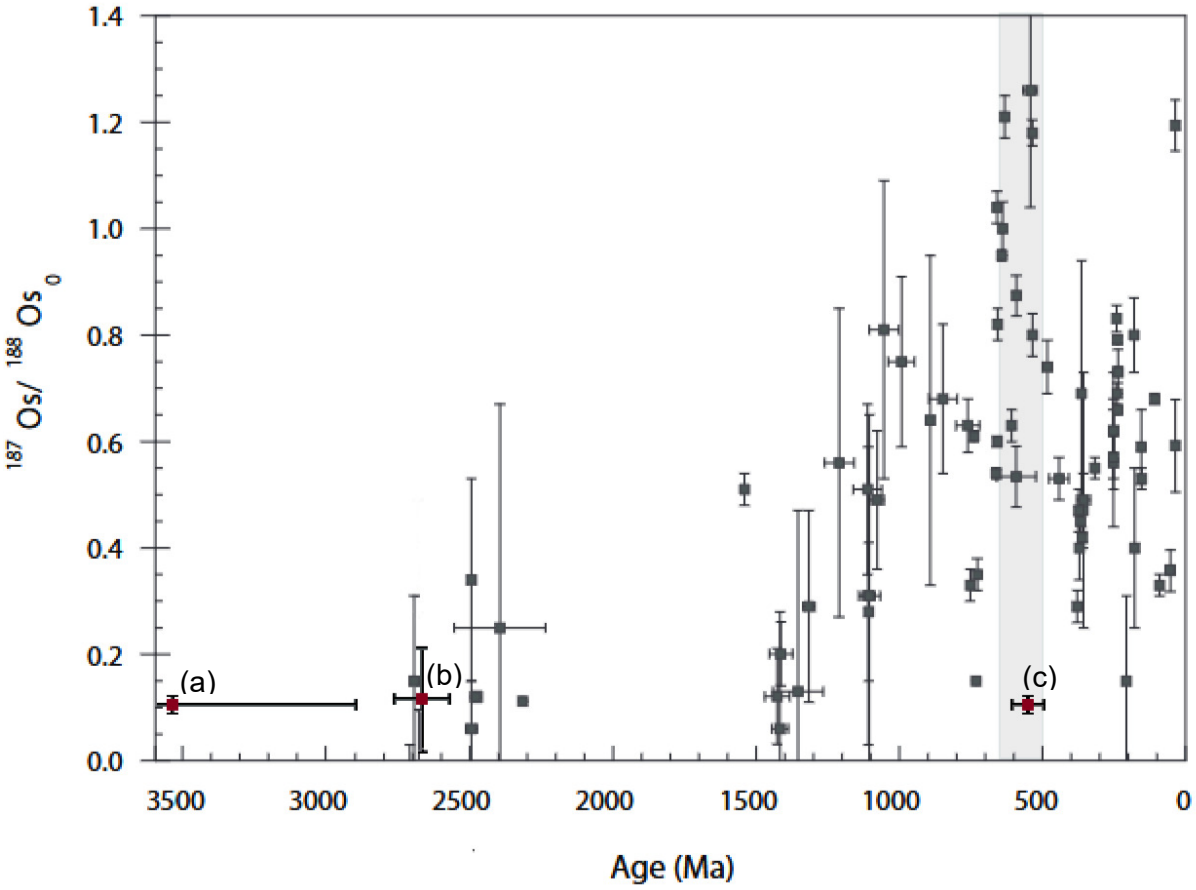

Figure 5.10: *Osmium seawater evolution curve and age data with error-bars over the last 3.5 billion years of organic-rich material. Results from (a) this study, (b) the Temagami BIF (Schulz et al., 2021), and (c) the Urucum BIF (Prost et al., 2024) were added (red data points). Shaded area around the boundary of the Proterozoic and the Cambrian marks an unusually high excursion of the Os isotopic ratio (modified after Peucker-Ehrenbrink and Ravizza, 2020)*

As is illustrated in Figure 5.10, the initial $^{187}Os/^{188}Os$ ratio obtained in this study (0.114 ± 0.007) agrees with the limited existing data (only 3 studies with geologically meaningful results) on Archean seawater compositions of ORMs, compiled by Peucker-Ehrenbrink and Ravizza (2020). Lu et al. (2017) calculated an average $^{187}Os/^{188}Os$ initial based on the available data of 0.18 ± 0.04, which is in line with the results from the Temagami BIF ($^{187}Os/^{188}Os_{(i)}$: 0.12 ± 0.10, Schulz et al., 2021) and from this study (Tomka BIF: 0.114 ± 0.007). Although the small sample size warrants caution, the average value of studies on ORM, together with BIF data, supports the trend of an unradiogenic, PUM-like, Archean seawater composition. As mentioned in the introductory Chapter 1.4.2 this unradiogenic Archean Ocean could be caused by a lack of oxidative weathering combined with the smaller volume of evolved continental

crust, which would have led to hydrothermal input being the dominant source of the marine osmium isotope budget (Sharma et al., 2007; Kendall, 2014; Lu et al., 2017).

6 Conclusions

The ~3.5-3.3 Ga old Tomka banded iron formation (BIF), hosted within the Daitari Greenstone Belt of the Singhbhum Craton in eastern India (Jodder et al., 2023), was analyzed for its highly siderophile element (HSE) content and Re-Os isotope systematics, as it may represent one of the oldest geochemical archives of Archean seawater. The samples thus may represent a primary Os isotopic signature of Archean seawater and provide an opportunity to directly constrain the age of the Tomka BIF through the Re-Os geochronometer. The main results are summarized as follows:

(i) The HSE concentrations in the Tomka BIF are generally slightly higher than those in the upper continental crust (UCC). No consistent patterns could be observed for HSE distribution between the different lithologies. The low Ir concentration of ~0.03 ppb does not indicate any extraterrestrial admixture for the Tomka BIF.

(ii) The studied samples of the Tomka BIF indicate little to no signs of syn-depositional alterations, based on the very low concentration of immobile elements such as Al and Zr, which typically indicate detrital contamination (e.g., Bau, 1993). The shale sample DM71A is interpreted to represent a detrital endmember, due to its elevated Al and Zr concentrations by two orders of magnitude. Although post-depositional alteration could not be definitively assessed, Sr-content and REY signatures (e.g., Kienle, 2024) suggest it was likely limited. Overall, the Tomka BIF is interpreted to represent a partly closed system.

(iii) Six samples yield back-calculated initial $^{187}Os/^{188}Os$ ratios clustering between ~0.10 to ~0.15 and thus around the $^{187}Os/^{188}Os$ ratio of the primitive upper mantle (PUM) of ~0.13 (Becker et al., 2006).

(iv) Six samples with PUM-like initial Os ratios were used to construct a linear regression line to attempt direct dating of the Tomka BIF. The final regression line yielded a model age of 3,557 ± 668 Ma. While this age is imprecise, it broadly agrees with the existing age estimations for the Tomka BIF (between ~3.51 to ~3.28 Ga; Hofmann et al., 2022; Jodder et al., 2023). However, based on the available data, it remains unclear whether

or not this age represents the primary deposition age or a later metamorphic overprint, nor if it truly reflects a meaningful geological age.

(v) Although the linear regression likely does not represent a geologically meaningful age, the $^{187}Os/^{188}Os_{(i)}$ y-intercept (~0.11) may still reflect an authigenic Archean seawater signal. This value is consistent with the signal from the Temagami BIF (~0.12; Schulz et al., 2021) and within the range of the few published Archean seawater $^{187}Os/^{188}Os$ data (averaging to ~0.18; Lu et al., 2017). These findings further strengthen the interpretation of an unradiogenic Os isotope composition for Archean seawater; however, due to the small sample size further studies are required.

7 References

Alexander B. W., Bau M. and Andersson P. (2009) Neodymium isotopes in Archean seawater and implications for the marine Nd cycle in Earth's early oceans. *Earth and Planetary Science Letters* **283**, 144–155.

Alexander B. W., Bau M., Andersson P. and Dulski P. (2008) Continentally-derived solutes in shallow Archean seawater: Rare earth element and Nd isotope evidence in iron formation from the 2.9Ga Pongola Supergroup, South Africa. *Geochimica et Cosmochimica Acta* **72**, 378–394.

Anbar A. D., Creaser R. A., Papanastassiou D. A. and Wasserburg G. J. (1992) Rhenium in seawater: Confirmation of generally conservative behavior. *Geochimica et Cosmochimica Acta* **56**, 4099–4103.

Anbar A. D., Duan Y., Lyons T. W., Arnold G. L., Kendall B., Creaser R. A., Kaufman A. J., Gordon G. W., Scott C., Garvin J. and Buick R. (2007) A Whiff of Oxygen Before the Great Oxidation Event? *Science* **317**, 1903–1906.

Anbar A. D. and Holland H. D. (1992) The photochemistry of manganese and the origin of banded iron formations. *Geochimica et Cosmochimica Acta* **56**, 2595–2603.

Andreasen R. and Sharma M. (2009) Comment on "Neodymium-142 Evidence for Hadean Mafic Crust." *Science* **325**, 267–267.

Audi G., Bersillon O., Blachot J. and Wapstra A. H. (2003) The Nubase evaluation of nuclear and decay properties. *Nuclear Physics A* **729**, 3–128.

Aulbach S., Mungall J. E. and Pearson D. G. (2016) Distribution and Processing of Highly Siderophile Elements in Cratonic Mantle Lithosphere. *Reviews in Mineralogy and Geochemistry* **81**, 239–304.

Barnes S.-J., Naldrett A. J. and Gorton M. P. (1985) The origin of the fractionation of platinum-group elements in terrestrial magmas. *Chemical Geology* **53**, 303–323.

Barrett T. J., Fralick P. W. and Jarvis I. (1988) Rare-earth-element geochemistry of some Archean iron formations north of Lake Superior, Ontario. *Canadian Journal of Earth Sciences* **25**, 570–580.

Basta F. F., Maurice A. E., Fontboté L. and Favarger P.-Y. (2011) Petrology and geochemistry of the banded iron formation (BIF) of Wadi Karim and Um Anab, Eastern Desert, Egypt: Implications for the origin of Neoproterozoic BIF. *Precambrian Research* **187**, 277–292.

Bau M. (1991) Rare-earth element mobility during hydrothermal and metamorphic fluid-rock interaction and the significance of the oxidation state of europium. *Chemical Geology* **93**, 219–230.

Bau M. (1993) Effects of syn- and post-depositional processes on the rare-earth element distribution in Precambrian iron-formations. *European Journal of Mineralogy* **5**, 257–267.

Bau M. (1996) Controls on the fractionation of isovalent trace elements in magmatic and aqueous systems: evidence from Y/Ho, Zr/Hf, and lanthanide tetrad effect. *Contributions to Mineralogy and Petrology* **123**, 323–333.

Bau M. (1999) Scavenging of dissolved yttrium and rare earths by precipitating iron oxyhydroxide: experimental evidence for Ce oxidation, Y-Ho fractionation, and lanthanide tetrad effect. *Geochimica et Cosmochimica Acta* **63**, 67–77.

Bau M. and Dulski P. (1996) Distribution of yttrium and rare-earth elements in the Penge and Kuruman iron-formations, Transvaal Supergroup, South Africa. *Precambrian Research* **79**, 37–55.

Bau M., Dulski P. and Möller P. (1995) Yttrium and Holmium in South Pacific Seawater: Vertical Distribution and Possible Fractionation Mechanisms. *Geochemistry* **55**, 1–15.

Bau M., Koschinsky A., Dulski P. and Hein J. R. (1996) Comparison of the partitioning behaviours of yttrium, rare earth elements, and titanium between hydrogenetic marine ferromanganese crusts and seawater. *Geochimica et Cosmochimica Acta* **60**, 1709–1725.

Becker H., Horan M. F., Walker R. J., Gao S., Lorand J.-P. and Rudnick R. L. (2006) Highly siderophile element composition of the Earth's primitive upper mantle: Constraints from new data on peridotite massifs and xenoliths. *Geochimica et Cosmochimica Acta* **70**, 4528–4550.

Bekker A. and Kovalick A. (2021) Ironstones and Iron Formations. In *Encyclopedia of Geology* (eds. D. Alderton and S. A. Elias). Elsevier. pp. 914–921.

Bekker A., Planavsky N. J., Krapež B., Rasmussen B., Hofmann A., Slack J. F., Rouxel O. J. and Konhauser K. O. (2014) Iron Formations: Their Origins and Implications for Ancient Seawater Chemistry. In *Treatise on Geochemistry (Vol. 9)* (eds. H. D. Holland and K. K. Turekian). Elsevier. pp. 561–628.

Bekker A., Slack J. F., Planavsky N., Krapez B., Hofmann A., Konhauser K. O. and Rouxel O. J. (2010) Iron Formation: The Sedimentary Product of a Complex Interplay among Mantle, Tectonic, Oceanic, and Biospheric Processes. *Economic Geology* **105**, 467–508.

Belevtsev Ya. N., Belevtsev R. Ya. and Siroshtan R. I. (1983) Chapter 5 The Krivoy Rog Basin. In *Developments in Precambrian Geology* (eds. A. F. Trendall and R. C. Morris). Elsevier. pp. 211–249.

Berner R. A., Beerling D. J., Dudley R., Robinson J. M. and Wildman R. A. (2003) Phanerozoic Atmospheric Oxygen. *Annual Review of Earth and Planetary Sciences* **31**, 105–134.

Beukes N. J. and Gutzmer J. (2008) Origin and Paleoenvironmental Significance of Major Iron Formations at the Archean-Paleoproterozoic Boundary. *Reviews in Economic Geology* **15**, 5–47.

Beukes N. J. and Klein C. (1990) Geochemistry and sedimentology of a facies transition — from microbanded to granular iron-formation — in the early Proterozoic Transvaal Supergroup, South Africa. *Precambrian Research* **47**, 99–139.

Birck J. L., Barman M. R. and Capmas F. (1997) Re-Os Isotopic Measurements at the Femtomole Level in Natural Samples. *Geostandards and Geoanalytical Research* **21**, 19–27.

Bolhar R., Kamber B. S., Moorbath S., Fedo C. M. and Whitehouse M. J. (2004) Characterisation of early Archaean chemical sediments by trace element signatures. *Earth and Planetary Science Letters* **222**, 43–60.

Bonnand P., Lalonde S. V., Boyet M., Heubeck C., Homann M., Nonnotte P., Foster I., Konhauser K. O. and Köhler I. (2020) Post-depositional REE mobility in a Paleoarchean banded iron formation revealed by La-Ce geochronology: A cautionary tale for signals of ancient oxygenation. *Earth and Planetary Science Letters* **547**, 116452.

Bowring S. A. and Williams I. S. (1999) Priscoan (4.00-4.03 Ga) orthogneisses from northwestern Canada. *Contributions to Mineralogy and Petrology* **134**, 3–16.

Brandon A. D., Humayun M., Puchtel I. S., Leya I. and Zolensky M. (2005) Osmium Isotope Evidence for an *s* -Process Carrier in Primitive Chondrites. *Science* **309**, 1233–1236.

Braterman P. S., Cairns-Smith A. G. and Sloper R. W. (1983) Photo-oxidation of hydrated Fe2+—significance for banded iron formations. *Nature* **303**, 163–164.

Braun M., Georgiev Y. M., Schönherr T., Wilsenach H. and Zuber K. (2017) A new precision measurement of the α -decay half-life of ^{190}Pt. *Physics Letters B* **768**, 317–320.

Brenan J. M., Bennett N. R. and Zajacz Z. (2016) Experimental Results on Fractionation of the Highly Siderophile Elements (HSE) at Variable Pressures and Temperatures during Planetary and Magmatic Differentiation. *Reviews in Mineralogy and Geochemistry* **81**, 1–87.

Bruland K. W., Middag R. and Lohan M. C. (2014) Controls of Trace Metals in Seawater. In *Treatise on Geochemistry (Vol. 8)* (eds. H. D. Holland and K. K. Turekian). Elsevier. pp. 19–51.

Cairns-Smith A. G. (1978) Precambrian solution photochemistry, inverse segregation, and banded iron formations. *Nature* **276**, 807–808.

Canfield D. E. (1998) A new model for Proterozoic ocean chemistry. *Nature* **396**, 450–453.

Canfield D. E., Poulton S. W., Knoll A. H., Narbonne G. M., Ross G., Goldberg T. and Strauss H. (2008) Ferruginous Conditions Dominated Later Neoproterozoic Deep-Water Chemistry. *Science* **321**, 949–952.

Canfield D. E., Poulton S. W. and Narbonne G. M. (2007) Late-Neoproterozoic Deep-Ocean Oxygenation and the Rise of Animal Life. *Science* **315**, 92–95.

Charbonnier Q., Bouchez J., Gaillardet J., Calmels D. and Dellinger M. (2022) The influence of black shale weathering on riverine barium isotopes. *Chemical Geology* **594**, 120741.

Chaudhuri T. (2020) A review of Hadean to Neoarchean crust generation in the Singhbhum Craton, India and possible connection with Pilbara Craton, Australia: The geochronological perspective. *Earth-Science Reviews* **202**, 103085.

Chaudhuri T., Wan Y., Mazumder R., Ma M. and Liu D. (2018) Evidence of Enriched, Hadean Mantle Reservoir from 4.2-4.0 Ga zircon xenocrysts from Paleoarchean TTGs of the Singhbhum Craton, Eastern India. *Scientific Reports* **8**, 7069.

Chou C.-L. (1978) Fractionation of siderophile elements in the Earth's upper mantle. In *Proceedings of the Lunar and Planetary Science Conference 9th* pp. 219–230.

Chu Z., Qiu Y., Zhou X., Yang X., Peng P., Zhao T. and Xu J. (2023) Re-Os, Sr-Nd isotopic and PGE elemental constraints for the formation of mid-Proterozoic ironstones in North China Craton: Implications for the atmospheric oxygen level. *Earth and Planetary Science Letters* **621**, 118367.

Claeys P., Kiessling W. and Alvarez W. (2002) Distribution of Chicxulub ejecta at the Cretaceous-Tertiary boundary. In *Catastrophic events and mass extinctions: impacts and beyond* (eds. C. Koeberl and K. G. MacLeod). Geological Society of America Special Publication v. 356. pp. 55–68.

Cohen A. S., Coe A. L., Bartlett J. M. and Hawkesworth C. J. (1999) Precise Re–Os ages of organic-rich mudrocks and the Os isotope composition of Jurassic seawater. *Earth and Planetary Science Letters* **167**, 159–173.

Cohen A. S. and Waters F. G. (1996) Separation of osmium from geological materials by solvent extraction for analysis by thermal ionisation mass spectrometry. *Analytica Chimica Acta* **332**, 269–275.

Colodner D., Sachs J., Ravizza G., Turekian K., Edmond J. and Boyle E. (1993) The geochemical cycle of rhenium: a reconnaissance. *Earth and Planetary Science Letters* **117**, 205–221.

Condie K. C., O'Neill C. and Aster R. C. (2009) Evidence and implications for a widespread magmatic shutdown for 250 My on Earth. *Earth and Planetary Science Letters* **282**, 294–298.

Cox G. M., Halverson G. P., Minarik W. G., Le Heron D. P., Macdonald F. A., Bellefroid E. J. and Strauss J. V. (2013) Neoproterozoic iron formation: An evaluation of its temporal, environmental and tectonic significance. *Chemical Geology* **362**, 232–249.

Danielson A., Möller P. and Dulski P. (1992) The europium anomalies in banded iron formations and the thermal history of the oceanic crust. *Chemical Geology* **97**, 89–100.

De Baar H. J. W., Brewer P. G. and Bacon M. P. (1985) Anomalies in rare earth distributions in seawater: Gd and Tb. *Geochimica et Cosmochimica Acta* **49**, 1961–1969.

De Oliveira Carvalho Rodrigues P., Hinnov L. A. and Franco D. R. (2019) A new appraisal of depositional cyclicity in the Neoarchean-Paleoproterozoic Dales Gorge Member (Brockman Iron Formation, Hamersley Basin, Australia). *Precambrian Research* **328**, 27–47.

De Vrese P., Stacke T., Caves Rugenstein J., Goodman J. and Brovkin V. (2021) Snowfall-albedo feedbacks could have led to deglaciation of snowball Earth starting from mid-latitudes. *Communications Earth & Environment* **2**, 91.

De Wit M. J., Armstrong R. A., Kamo S. L. and Erlank A. J. (1993) Gold-bearing sediments in the Pietersburg greenstone belt; age equivalents of the Witwatersrand Supergroup sediments, South Africa. *Economic Geology* **88**, 1242–1252.

Derry L. and Jacobsen S. B. (1990) The chemical evolution of Precambrian seawater: Evidence from REEs in banded iron formations. *Geochimica et Cosmochimica Acta* **54**, 2965–2977.

Dimroth E. (1976) Apects of the sedimentary petrology of cherty iron-formation. In *Handbook of Strata-bound and Strataform Ore Deposits* (ed. K. H. Wolf). Elsevier. pp. 203–254.

Dodd M. S., Wang H., Li C., Towner M., Thomson A. R., Slack J. F., Wan Y., Pirajno F., Manikyamba C., Wang Q. and Papineau D. (2022) Abiotic anoxic iron oxidation, formation of Archean banded iron formations, and the oxidation of early Earth. *Earth and Planetary Science Letters* **584**, 117469.

Dorr II J. V. N. (1945) Manganese and iron deposits of Morro do Urucum, Mato Grosso, Brazil. *U.S. Geological Survey Bulletin* **946a**, 1–67.

Douville E., Charlou J. L., Oelkers E. H., Bienvenu P., Colon C. F. J., Donval J. P., Fouquet Y., Prieur D. and Appriou P. (2002) The rainbow vent fluids (36°14VN, MAR): the influence of ultramafic rocks and phase separation on trace metal content in Mid-Atlantic Ridge hydrothermal fluids. *Chemical Geology* **184**, 37–48.

Drake M. J. (2005) Origin of water in the terrestrial planets. *Meteoritics & Planetary Science* **40**, 519–527.

Drake M. J. and Righter K. (2002) Determining the composition of the Earth. *Nature* **416**, 39–44.

Dunn J. A. and Dey A. K. (1942) Geology and Petrology of Eastern Singhbhum and Surrounding Areas. *Memoirs of the Geological Survey of India* **69**, 281–450.

Dymek R. F. and Klein C. (1988) Chemistry, petrology and origin of banded iron-formation lithologies from the 3800 Ma Isua supracrustal belt, West Greenland. *Precambrian Research* **39**, 247–302.

Edwards C. T. (2019) Links between early Paleozoic oxygenation and the Great Ordovician Biodiversification Event (GOBE): A review. *Palaeoworld* **28**, 37–50.

Emerson D. and Moyer C. L. (2002) Neutrophilic Fe-Oxidizing Bacteria Are Abundant at the Loihi Seamount Hydrothermal Vents and Play a Major Role in Fe Oxide Deposition. *Applied and Environmental Microbiology* **68**, 3085–3093.

Fairchild I. J. and Kennedy M. J. (2007) Neoproterozoic glaciation in the Earth System. *Journal of the Geological Society, London* **164**, 895–921.

Farquhar J., Thiemens M. and Bao H. (2000) Atmospheric Influence of Earth's Earliest Sulfur Cycle. *Science* **289**, 756–758.

Finlay A. J., Selby D. and Gröcke D. R. (2010) Tracking the Hirnantian glaciation using Os isotopes. *Earth and Planetary Science Letters* **293**, 339–348.

Fischer-Gödde M. and Becker H. (2012) Osmium isotope and highly siderophile element constraints on ages and nature of meteoritic components in ancient lunar impact rocks. *Geochimica et Cosmochimica Acta* **77**, 135–156.

Fischer-Gödde M., Becker H. and Wombacher F. (2010) Rhodium, gold and other highly siderophile element abundances in chondritic meteorites. *Geochimica et Cosmochimica Acta* **74**, 356–379.

Fischer-Gödde M. and Kleine T. (2017) Ruthenium isotopic evidence for an inner Solar System origin of the late veneer. *Nature* **541**, 525–527.

Fyon J. and Cole S. (1989) Geology of part of the Temagami greenstone belt, District of Nipissing, including relationships between lithological, alteration, and structural features and precious-metal occurrences. *Ontario Geological Survey Publication Miscellaneous Paper* **146**, 108–115.

Gaucher C., Sial A. N. and Frei R. (2015) Chapter 17 - Chemostratigraphy of Neoproterozoic Banded Iron Formation (BIF): Types, Age and Origin. In *Chemostratigraphy* (ed. Mu. Ramkumar). Elsevier. pp. 433–449.

Georgiev S. V., Stein H. J., Hannah J. L., Henderson C. M. and Algeo T. J. (2015) Enhanced recycling of organic matter and Os-isotopic evidence for multiple magmatic or meteoritic inputs to the Late Permian Panthalassic Ocean, Opal Creek, Canada. *Geochimica et Cosmochimica Acta* **150**, 192–210.

German C. R. and Seyfried W. E. (2014) Hydrothermal Processes. In *Treatise on Geochemistry (Vol. 8)* (eds. H. D. Holland and K. K. Turekian). Elsevier. pp. 191–233.

Glikson A. and Allen C. (2004) Iridium anomalies and fractionated siderophile element patterns in impact ejecta, Brockman Iron Formation, Hamersley Basin, Western Australia: evidence for a major asteroid impact in simatic crustal regions of the early Proterozoic earth. *Earth and Planetary Science Letters* **220**, 247–264.

Goddéris Y., Donnadieu Y., Nédélec A., Dupré B., Dessert C., Grard A., Ramstein G. and François L. M. (2003) The Sturtian 'snowball' glaciation: fire and ice. *Earth and Planetary Science Letters* **211**, 1–12.

Gole M. J. (1981) Archean banded iron-formations, Yilgarn Block, Western Australia. *Economic Geology* **76**, 1954–1974.

Gourcerol B., Thurston P. C., Kontak D. J., Côté-Mantha O. and Biczok J. (2016) Depositional setting of Algoma-type banded iron formation. *Precambrian Research* **281**, 47–79.

Gross G. A. (1965) Geology of iron deposits in Canada. I. General geology and evaluation of iron deposits. *Geological Survey of Canada. Economic Geology Report* **22**.

Gross G. A., Canada G. and Steet B. (1980) A classification of iron-formations based on depositional environments. *Canadian Mineralogist* **18**, 215–222.

Han T.-M. and Runnegar B. (1992) Megascopic Eukaryotic Algae from the 2.1-Billion-Year-Old Negaunee Iron-Formation, Michigan. *Science* **257**, 232–235.

Hannah J. L., Bekker A., Stein H. J., Markey R. J. and Holland H. D. (2004) Primitive Os and 2316 Ma age for marine shale: implications for Paleoproterozoic glacial events and the rise of atmospheric oxygen. *Earth and Planetary Science Letters* **225**, 43–52.

Hannah J. L. and Stein H. J. (2012) Re–Os geochemistry. In *Reading the Archive of Earth's Oxygenation, volume 3: Global Events and the Fennoscandian Arctic Russia – Drilling Early Earth Project.* (eds. V. A. Melezhik, L. R. Kump, A. E. Fallick, H. Strauss, E. J. Hanski, A. R. Prave, and A. Lepland). Springer Berlin Heidelberg. pp. 1506–1514.

Harrison T. M. (2009) The Hadean Crust: Evidence from >4 Ga Zircons. *Annual Review of Earth and Planetary Sciences* **37**, 479–505.

Hartman H. (1984) The evolution of photosynthesis and microbial mats: A speculation on banded iron formations. In *Microbial Mats: Stromatolites* (eds. Y. Cohen, R. W. Castenholz, and H. O. Halvorson). Alan R. Liss, New York. pp. 449–453.

Hegner E., Kröner A. and Hofmann A. W. (1984) Age and isotope geochemistry of the Archaean Pongola and Usushwana suites in Swaziland, southern Africa: a case for crustal contamination of mantle-derived magma. *Earth and Planetary Science Letters* **70**, 267–279.

Helmstaedt H., Eisbacher G. H. and McGregor J. A. (1979) Copper mineralization near an intra-Rapitan unconformity, Nite copper prospect, Nlackenzie Mountains, Northwest Territories, Canada. *Canadian Journal of Earth Sciences* **16**, 50–59.

Herwartz D. and Viehmann S. (2024) Does water transparency control the banding in shallow water iron formations? *South African Journal of Geology* **127**, 379–390.

Heubeck C., Engelhardt J., Byerly G. R., Zeh A., Sell B., Luber T. and Lowe D. R. (2013) Timing of deposition and deformation of the Moodies Group (Barberton Greenstone Belt, South Africa): Very-high-resolution of Archaean surface processes. *Precambrian Research* **231**, 236–262.

Heumann K. G. (1992) Isotope dilution mass spectrometry. *International Journal of Mass Spectrometry and Ion Processes* **118–119**, 575–592.

Hoffman P. F. and Schrag D. P. (2002) The snowball Earth hypothesis: testing the limits of global change. *Terra Nova* **14**, 129–155.

Hoffmann P. F., Hawkins D. P., Isachsen C. E. and Bowring S. A. (1996) Precise U- Pb zircon ages for early Damaran magmatism in the Summas Mountains and Welwitschia Inlier, northern Damara belt, Namibia. *Communications of the Geological Survey of Namibia* **11**, 47–52.

Hofmann A., Jodder J., Xie H., Bolhar R., Whitehouse M. and Elburg M. (2022) The Archaean geological history of the Singhbhum Craton, India – a proposal for a consistent framework of craton evolution. *Earth-Science Reviews* **228**, 103994.

Holland H. D. (1973) The Oceans; A Possible Source of Iron in Iron-Formations. *Economic Geology* **68**, 1169–1172.

Holland H. D. (1984) *The chemical evolution of the atmosphere and oceans*., Princeton University Press, Princeton, N.J, 1-598.

Holland H. D. (2002) Volcanic gases, black smokers, and the great oxidation event. *Geochimica et Cosmochimica Acta* **66**, 3811–3826.

Holland H. D. (2006) The oxygenation of the atmosphere and oceans. *Philosophical Transactions of the Royal Society B: Biological Sciences* **361**, 903–915.

Hyde W. T., Crowley T. J., Baum S. K. and Peltier W. R. (2000) Neoproterozoic `snowball Earth' simulations with a coupled climate/ice-sheet model. *Nature* **405**, 425–429.

Inghram M. G. (1954) Stable Isotope Dilution as an Analytical Tool. *Annual Review of Nuclear Science* **4**, 81–92.

Isley A. E. (1995) Hydrothermal Plumes and the Delivery of Iron to Banded Iron Formation. *The Journal of Geology* **103**, 169–185.

Iyengar S. V. P. and Murthy Y. G. K. (1982) The evolution of the Archean Proterozoic crust in parts of Bihar and Orissa, eastern India. *Records of the Geological Survey of India* **112**, 1–5.

Jain A. K., Banerjee D. M. and Kale V. S. (2020) *Tectonics of the Indian Subcontinent*., Springer International Publishing, 1-576.

Jodder J. (2021) The geology of the Daitari greenstone belt, Singhbhum craton, India - Insights into early life 3.5 Ga ago. PhD thesis, University of Johannesburg.

Jodder J., Hofmann A., Xie H., Elburg M. A. and Wilson A. (2023) Geochronology of the Daitari Greenstone Belt, Singhbhum Craton, India. *Precambrian Research* **388**, 106997.

Kappler A., Pasquero C., Konhauser K. O. and Newman D. K. (2005) Deposition of banded iron formations by anoxygenic phototrophic Fe(II)-oxidizing bacteria. *Geology* **33**, 865–868.

Katchinoff J. A. R., Syverson D. D., Planavsky N. J., Evans E. S. J. and Rooney A. D. (2021) Seawater Chemistry and Hydrothermal Controls on the Cenozoic Osmium Cycle. *Geophysical Research Letters* **48**, e2021GL095558.

Kendall B. (2014) An osmium-based method for assessing the source of dissolved rhenium and molybdenum to Archean seawater. *Chemical Geology* **385**, 92–103.

Kendall B., Creaser R. A., Reinhard C. T., Lyons T. W. and Anbar A. D. (2015) Transient episodes of mild environmental oxygenation and oxidative continental weathering during the late Archean. *Science Advances* **1**, e1500777.

Kienle S. (2024) Reconstruction of a 3.5-billion-year-old marine environment: Evidence from trace element systematics of the iron formation exposed in the Daitari Greenstone Belt, Singhbhum Craton, India. Master's thesis, University of Vienna.

Kimura K., Lewis R. S. and Anders E. (1974) Distribution of gold and rhenium between nickel-iron and silicate melts: implications for the abundance of siderophile elements on the Earth and Moon. *Geochimica et Cosmochimica Acta* **38**, 683–701.

Klein C. (2005) Some Precambrian banded iron-formations (BIFs) from around the world: Their age, geologic setting, mineralogy, metamorphism, geochemistry, and origins. *American Mineralogist* **90**, 1473–1499.

Klein C. and Beukes N. J. (1993) Sedimentology and geochemistry of the glaciogenic late Proterozoic Rapitan Iron-Formation in Canada. *Economic Geology* **88**, 542–565.

Klemm V., Frank M., Levasseur S., Halliday A. N. and Hein J. R. (2008) Seawater osmium isotope evidence for a middle Miocene flood basalt event in ferromanganese crust records. *Earth and Planetary Science Letters* **273**, 175–183.

Klinkhammer G., Elderfield H. and Hudson A. (1983) Rare earth elements in seawater near hydrothermal vents. *Nature* **305**, 185–188.

Knoll A. H., Javaux E. J., Hewitt D. and Cohen P. (2006) Eukaryotic organisms in Proterozoic oceans. *Phil. Trans. R. Soc. B* **361**, 1023–1038.

Koeberl C. (2014) The Geochemistry and Cosmochemistry of Impacts. In *Treatise on Geochemistry (Vol. 2)* (eds. H. D. Holland and K. K. Turekian). Elsevier. pp. 73–118.

Konhauser K. O., Amskold L., Lalonde S. V., Posth N. R., Kappler A. and Anbar A. (2007) Decoupling photochemical Fe(II) oxidation from shallow-water BIF deposition. *Earth and Planetary Science Letters* **258**, 87–100.

Konhauser K. O., Planavsky N. J., Hardisty D. S., Robbins L. J., Warchola T. J., Haugaard R., Lalonde S. V., Partin C. A., Oonk P. B. H., Tsikos H., Lyons T. W., Bekker A. and Johnson C. M. (2017) Iron formations: A global record of Neoarchaean to Palaeoproterozoic environmental history. *Earth-Science Reviews* **172**, 140–177.

Lantink M. L., Davies J. H. F. L., Mason P. R. D., Schaltegger U. and Hilgen F. J. (2019) Climate control on banded iron formations linked to orbital eccentricity. *Nature Geoscience* **12**, 369–374.

Lantink M. L., Davies J. H. F. L., Ovtcharova M. and Hilgen F. J. (2022) Milankovitch cycles in banded iron formations constrain the Earth–Moon system 2.46 billion years ago. *Proceedings of the National Academy of Sciences* **119**, e2117146119.

Li S., Chai Z. and Mao X. (2007) Iridium in the Bering Sea and Arctic Ocean studied by neutron activation analysis. *Journal of Radioanalytical and Nuclear Chemistry* **271**, 125–128.

Li W., Beard B. L. and Johnson C. M. (2015) Biologically recycled continental iron is a major component in banded iron formations. *Proceedings of the National Academy of Sciences* **112**, 8193–8198.

Li X., Li C., Jiang X., Zhao H., Zhou L., Qu W. and Du A. (2023) High-resolution Re-Os isotope stratigraphy, and geochemical fingerprints identification of Late Ordovician–Early Silurian strata in northern Guizhou, China: Implications for LOME and environmental changes. *Earth-Science Reviews* **243**, 104497.

Li Y.-L. (2014) Micro- and nanobands in late Archean and Palaeoproterozoic banded-iron formations as possible mineral records of annual and diurnal depositions. *Earth and Planetary Science Letters* **391**, 160–170.

Linnen R. L., Samson I. M., Williams-Jones A. E. and Chakhmouradian A. R. (2014) Geochemistry of the Rare-Earth Element, Nb, Ta, Hf, and Zr Deposits. In *Treatise on Geochemistry (Vol. 13)* (eds. H. D. Holland and K. K. Turekian). Elsevier. pp. 543–568.

Liu C. X., Capirala A., Olson S. L., Jansen M. F. and Dauphas N. (2024) Ocean mixing timescale through time and implications for the origin of iron formations. *Geochemical Perspectives Letters* **31**, 54–59.

Liu K., Gao X., Li L., Chen C.-T. A. and Xing Q. (2018) Determination of ultra-trace Pt, Pd and Rh in seawater using an off-line pre-concentration method and inductively coupled plasma mass spectrometry. *Chemosphere* **212**, 429–437.

Liu X.-M., Kah L. C., Knoll A. H., Cui H., Wang C., Bekker A. and Hazen R. M. (2021) A persistently low level of atmospheric oxygen in Earth's middle age. *Nature Communications* **12**, 351.

Lowenstein T. K., Kendall B. and Anbar A. D. (2014) The Geologic History of Seawater. In *Treatise on Geochemistry (Vol. 8)* (eds. H. D. Holland and K. K. Turekian). Elsevier. pp. 569–622.

Lu W., Ridgwell A., Thomas E., Hardisty D. S., Luo G., Algeo T. J., Saltzman M. R., Gill B. C., Shen Y., Ling H.-F., Edwards C. T., Whalen M. T., Zhou X., Gutchess K. M., Jin L., Rickaby R. E. M., Jenkyns H. C., Lyons T. W., Lenton T. M., Kump L. R. and Lu Z. (2018) Late inception of a resiliently oxygenated upper ocean. *Science* **361**, 174–177.

Lu X., Kendall B., Stein H. J. and Hannah J. L. (2017) Temporal record of osmium concentrations and $^{187}Os/^{188}Os$ in organic-rich mudrocks: Implications for the osmium geochemical cycle and the use of osmium as a paleoceanographic tracer. *Geochimica et Cosmochimica Acta* **216**, 221–241.

Luguet A., Behrens M., Pearson D. G., König S. and Herwartz D. (2015) Significance of the whole rock Re–Os ages in cryptically and modally metasomatised cratonic peridotites: Constraints from HSE–Se–Te systematics. *Geochimica et Cosmochimica Acta* **164**, 441–463.

Luguet A., Nowell G. M. and Pearson D. G. (2008) 184Os/188Os and 186Os/188Os measurements by Negative Thermal Ionisation Mass Spectrometry (N-TIMS): Effects of interfering element and mass fractionation corrections on data accuracy and precision. *Chemical Geology* **248**, 342–362.

Lyons T. W., Anbar A. D., Severmann S., Scott C. and Gill B. C. (2009) Tracking Euxinia in the Ancient Ocean: A Multiproxy Perspective and Proterozoic Case Study. *Annual Review of Earth and Planetary Sciences* **37**, 507–534.

Lyons T. W., Reinhard C. T. and Planavsky N. J. (2014) The rise of oxygen in Earth's early ocean and atmosphere. *Nature* **506**, 307–315.

Lyons T. W., Tino C. J., Fournier G. P., Anderson R. E., Leavitt W. D., Konhauser K. O. and Stüeken E. E. (2024) Co-evolution of early Earth environments and microbial life. *Nature Reviews Microbiology* **22**, 572–586.

Macdonald F. A., Schmitz M. D., Crowley J. L., Roots C. F., Jones D. S., Maloof A. C., Strauss J. V., Cohen P. A., Johnston D. T. and Schrag D. P. (2010) Calibrating the Cryogenian. *Science* **327**, 1241–1243.

Mänd K., Robbins L. J., Planavsky N. J., Bekker A. and Konhauser K. O. (2022) *Iron Formations as Palaeoenvironmental Archives*. 1st ed., Cambridge University Press, 1-31.

Mashio A. S., Obata H. and Gamo T. (2017) Dissolved Platinum Concentrations in Coastal Seawater: Boso to Sanriku Areas, Japan. *Archives of Environmental Contamination and Toxicology* **73**, 240–246.

Meisel T., Burnham O., Kriete C. and Schulz T. (2013) Osmium isotope and PGE reference materials OKUM and MUH-1. *Mineralogical Magazine* **77**, 1734.

Meisel T., Moser J. and Wegscheider W. (2001) Recognizing heterogeneous distribution of platinum group elements (PGE) in geological materials by means of the Re–Os isotope system. *Analytical and Bioanalytical Chemistry* **370**, 566–572.

Meisel T., Walker R. J., Irving A. J. and Lorand J.-P. (2001) Osmium isotopic compositions of mantle xenoliths: a global perspective. *Geochimica et Cosmochimica Acta* **65**, 1311–1323.

Mills B. J. W., Krause A. J., Jarvis I. and Cramer B. D. (2023) Evolution of Atmospheric O_2 Through the Phanerozoic, Revisited. *Annual Review of Earth and Planetary Sciences* **51**, 253–276.

Mloszewska A. M., Pecoits E., Cates N. L., Mojzsis S. J., O'Neil J., Robbins L. J. and Konhauser K. O. (2012) The composition of Earth's oldest iron formations: The Nuvvuagittuq Supracrustal Belt (Québec, Canada). *Earth and Planetary Science Letters* **317–318**, 331–342.

Mottl M. J., Glazer B. T., Kaiser R. I. and Meech K. J. (2007) Water and astrobiology. *Geochemistry* **67**, 253–282.

Mukhopadhyay D. and Matin A. (2020) The Architecture and Evolution of the Singhbhum Craton. *Episodes* **43**, 19–50.

Mukhopadhyay J. (2020) Archean banded iron formations of India. *Earth-Science Reviews* **201**, 102927.

Mukhopadhyay J., Beukes N. J., Armstrong R. A., Zimmermann U., Ghosh G. and Medda R. A. (2008) Dating the Oldest Greenstone in India: A 3.51-Ga Precise U-Pb SHRIMP Zircon Age for Dacitic Lava of the Southern Iron Ore Group, Singhbhum Craton. *The Journal of Geology* **116**, 449–461.

Mukhopadhyay J., Mishra B., Chakrabarti K., De S. and Ghosh G. (2016) Uraniferous paleoplacers of the Mesoarchean Mahagiri Quartzite, Singhbhum craton, India: Depositional controls, nature and source of >3.0Ga detrital uraninites. *Ore Geology Reviews* **72**, 1290–1306.

Ndime E. N., Ganno S. and Nzenti J. P. (2019) Geochemistry and Pb–Pb geochronology of the Neoarchean Nkout West metamorphosed banded iron formation, southern Cameroon. *International Journal of Earth Sciences* **108**, 1551–1570.

Nebel O. (2016) Strontium. In *Encyclopedia of Geochemistry* (ed. W. M. White). Encyclopedia of Earth Sciences Series. Springer International Publishing, Cham. pp. 1377–1378.

Norman M. D. (2023) The ^{187}Re-^{187}Os and ^{190}Pt-^{186}Os Radiogenic Isotope Systems: Techniques and Applications to Metallogenic Systems. In *Isotopes in Economic Geology, Metallogenesis and Exploration* (eds. D. Huston and J. Gutzmer). Mineral Resource Reviews. Springer International Publishing, Cham. pp. 89–122.

Nutman A. P., Bennett V. C., Friend C. R. L. and Rosing M. T. (1997) ~ 3710 and ⩾ 3790 Ma volcanic sequences in the Isua (Greenland) supracrustal belt; structural and Nd isotope implications. *Chemical Geology* **141**, 271–287.

Och L. M. and Shields-Zhou G. A. (2012) The Neoproterozoic oxygenation event: Environmental perturbations and biogeochemical cycling. *Earth-Science Reviews* **110**, 26–57.

Olierook H. K. H., Clark C., Reddy S. M., Mazumder R., Jourdan F. and Evans N. J. (2019) Evolution of the Singhbhum Craton and supracrustal provinces from age, isotopic and chemical constraints. *Earth-Science Reviews* **193**, 237–259.

Olson S. L., Kump L. R. and Kasting J. F. (2013) Quantifying the areal extent and dissolved oxygen concentrations of Archean oxygen oases. *Chemical Geology* **362**, 35–43.

O'Neil J., Francis D. and Carlson R. W. (2011) Implications of the Nuvvuagittuq Greenstone Belt for the Formation of Earth's Early Crust. *Journal of Petrology* **52**, 985–1009.

Palme H. and O'Neill H. St. C. (2014) Cosmochemical Estimates of Mantle Composition. In *Treatise on Geochemistry (Vol. 3)* (eds. H. D. Holland and K. K. Turekian). Elsevier. pp. 1–39.

Paquay F. S., Ravizza G. and Coccioni R. (2014) The influence of extraterrestrial material on the late Eocene marine Os isotope record. *Geochimica et Cosmochimica Acta* **144**, 238–257.

Parekh P. P., Möller P., Dulski P. and Bausch W. M. (1977) Distribution of trace elements between carbonate and non-carbonate phases of limestone. *Earth and Planetary Science Letters* **34**, 39–50.

Paul M., Reisberg L., Vigier N., Zheng Y., Ahmed K. M., Charlet L. and Huq M. R. (2010) Dissolved osmium in Bengal plain groundwater: Implications for the marine Os budget. *Geochimica et Cosmochimica Acta* **74**, 3432–3448.

Pearson D. G. and Woodland S. J. (2000) Solvent extraction/anion exchange separation and determination of PGEs (Os, Ir, Pt, Pd, Ru) and Re–Os isotopes in geological samples by isotope dilution ICP-MS. *Chemical Geology* **165**, 87–107.

Percak-Dennett E. M., Beard B. L., Xu H., Konishi H., Johnson C. M. and Roden E. E. (2011) Iron isotope fractionation during microbial dissimilatory iron oxide reduction in simulated Archaean seawater. *Geobiology* **9**, 205–220.

Percival L. M. E., Selby D., Bond D. P. G., Rakociński M., Racki G., Marynowski L., Adatte T., Spangenberg J. E. and Föllmi K. B. (2019) Pulses of enhanced continental weathering associated with multiple Late Devonian climate perturbations: Evidence from osmium-isotope compositions. *Palaeogeography, Palaeoclimatology, Palaeoecology* **524**, 240–249.

Peters S. T. M., Münker C., Becker H. and Schulz T. (2014) Alpha-decay of ^{184}Os revealed by radiogenic ^{180}W in meteorites: Half-life determination and viability as geochronometer. *Earth and Planetary Science Letters* **391**, 69–76.

Peucker-Ehrenbrink B. and Hannigan R. E. (2000) Effects of black shale weathering on the mobility of rhenium and platinum group elements. *Geology* **28**, 475-478.

Peucker-Ehrenbrink B. and Jahn B. (2001) Rhenium-osmium isotope systematics and platinum group element concentrations: Loess and the upper continental crust: Eroding continental crust. *Geochemistry, Geophysics, Geosystems* **2**, 2001GC000172.

Peucker-Ehrenbrink B. P. and Ravizza G. (1996) Continental runoff of osmium into the Baltic Sea. *Geology* **24**, 327–330.

Peucker-Ehrenbrink B. and Ravizza G. (2000) The marine osmium isotope record. *Terra Nova* **12**, 205–219.

Peucker-Ehrenbrink B. and Ravizza G. (2012) Osmium Isotope Stratigraphy. In *The Geologic Time Scale* (eds. F. M. Gradstein, J. G. Ogg, M. D. Schmitz, and G. M. Ogg). Elsevier. pp. 145–166.

Peucker-Ehrenbrink B. and Ravizza G. E. (2020) Osmium Isotope Stratigraphy. In *Geologic Time Scale 2020* (eds. F. M. Gradstein, J. G. Ogg, M. D. Schmitz, and G. M. Ogg). Elsevier. pp. 239–257.

Piacentini T., Vasconcelos P. M. and Farley K. A. (2013) $^{40}Ar/^{39}Ar$ constraints on the age and thermal history of the Urucum Neoproterozoic banded iron-formation, Brazil. *Precambrian Research* **228**, 48–62.

Pierson-Wickmann A.-C., Reisberg L. and France-Lanord C. (2000) The Os isotopic composition of Himalayan river bedloads and bedrocks: importance of black shales. *Earth and Planetary Science Letters* **176**, 203–218.

Planavsky N. J., McGoldrick P., Scott C. T., Li C., Reinhard C. T., Kelly A. E., Chu X., Bekker A., Love G. D. and Lyons T. W. (2011) Widespread iron-rich conditions in the mid-Proterozoic ocean. *Nature* **477**, 448–451.

Poulton S. W. and Canfield D. E. (2011) Ferruginous Conditions: A Dominant Feature of the Ocean through Earth's History. *Elements* **7**, 107–112.

Prost T. (2023) „Direct radiometric dating of a Neoproterozoic iron formation – Rhenium-Os and highly siderophile element systematics of the Urucum Iron Formation, Brazil". Master's thesis, University of Vienna.

Prost T., Schulz T., Viehmann S., Walde D. H. G. and Koeberl C. (2024) Highly siderophile element and Re-Os isotope systematics of a Neoproterozoic Iron Formation and its temporal relation to glaciation events. *Geochimica et Cosmochimica Acta* **384**, 140–154.

Ramakrishnan M. and Vaidyanadhan R. (2010) *Geology of India*. Reprint edition., Geological Society of India, Bangalore, 1-984.

Rasmussen B., Meier D. B., Krapež B. and Muhling J. R. (2013) Iron silicate microgranules as precursor sediments to 2.5-billion-year-old banded iron formations. *Geology* **41**, 435–438.

Ravizza G. and Peucker-Ehrenbrink B. (2003) Chemostratigraphic Evidence of Deccan Volcanism from the Marine Osmium Isotope Record. *Science* **302**, 1392–1395.

Ravizza G. and Turekian K. K. (1989) Application of the ^{187}Re-^{187}Os system to black shale geochronometry. *Geochimica et Cosmochimica Acta* **53**, 3257–3262.

Robbins L. J., Lalonde S. V., Planavsky N. J., Partin C. A., Reinhard C. T., Kendall B., Scott C., Hardisty D. S., Gill B. C., Alessi D. S., Dupont C. L., Saito M. A., Crowe S. A., Poulton S. W., Bekker A., Lyons T. W. and Konhauser K. O. (2016) Trace elements at the intersection of marine biological and geochemical evolution. *Earth-Science Reviews* **163**, 323–348.

Robinson N., Ravizza G., Coccioni R., Peucker-Ehrenbrink B. and Norris R. (2009) A high-resolution marine $^{187}Os/^{188}Os$ record for the late Maastrichtian: Distinguishing the chemical fingerprints of Deccan volcanism and the KP impact event. *Earth and Planetary Science Letters* **281**, 159–168.

Rooney A. D., Hnatyshin D., Toma J., Saintilan N. J., Millikin A. E. G., Selby D. and Creaser R. A. (2024) Application of the ^{187}Re-^{187}Os geochronometer to crustal materials: Systematics, methodology, data reporting, and interpretation. *Geological Society of America Bulletin* **136**, 4091–4129.

Rooney A. D., Macdonald F. A., Strauss J. V., Dudás F. Ö., Hallmann C. and Selby D. (2014) Re-Os geochronology and coupled Os-Sr isotope constraints on the Sturtian snowball Earth. *Proceedings of the National Academy of Sciences* **111**, 51–56.

Rooney A. D., Strauss J. V., Brandon A. D. and Macdonald F. A. (2015) A Cryogenian chronology: Two long-lasting synchronous Neoproterozoic glaciations. *Geology* **43**, 459–462.

Saha A. K. (1988) Some aspects of the crustal growth of the Singhbhum-Orissa Iron Ore craton, eastern India. *Indian Journal of Geology* **60**, 270–278.

Saha A. K. (1994) *Crustal Evolution of Singhbhum-North Orissa, Eastern India*. Geological Society of India, 1-341.

Sarkar S. C. and Gupta A. (2012) *Crustal Evolution and Metallogeny in India*. 1st ed., Cambridge University Press, New York, 1-840.

Schad M., Halama M., Bishop B., Konhauser K. O. and Kappler A. (2019) Temperature fluctuations in the Archean ocean as trigger for varve-like deposition of iron and silica minerals in banded iron formations. *Geochimica et Cosmochimica Acta* **265**, 386–412.

Schulz T., Viehmann S., Hezel D. C., Koeberl C. and Bau M. (2021) Highly Siderophile Elements and Coupled Fe-Os Isotope Signatures in the Temagami Iron Formation, Canada: Possible Signatures of Neoarchean Seawater Chemistry and Earth's Oxygenation History. *Astrobiology* **21**, 924–939.

Selby D. and Creaser R. A. (2003) Re–Os geochronology of organic rich sediments: an evaluation of organic matter analysis methods. *Chemical Geology* **200**, 225–240.

Selby D. and Creaser R. A. (2005) Direct radiometric dating of the Devonian-Mississippian time-scale boundary using the Re-Os black shale geochronometer. *Geology* **33**, 545–548.

Selby D., Creaser R. A., Stein H. J., Markey R. J. and Hannah J. L. (2007) Assessment of the ^{187}Re decay constant by cross calibration of Re–Os molybdenite and U–Pb zircon chronometers in magmatic ore systems. *Geochimica et Cosmochimica Acta* **71**, 1999–2013.

Sharma M., Rosenberg E. J. and Butterfield D. A. (2007) Search for the proverbial mantle osmium sources to the oceans: Hydrothermal alteration of mid-ocean ridge basalt. *Geochimica et Cosmochimica Acta* **71**, 4655–4667.

Shen Y. (2002) Middle Proterozoic ocean chemistry: Evidence from the McArthur Basin, northern Australia. *American Journal of Science* **302**, 81–109.

Søgaard E. G., Medenwaldt R. and Abraham-Peskir J. V. (2000) Conditions and rates of biotic and abiotic iron precipitation in selected Danish freshwater plants and microscopic analysis of precipitate morphology. *Water Research* **34**, 2675–2682.

Sreenivas B., Dey S., Bhaskar Rao Y. J., Vijaya Kumar T., Babu E. V. S. S. K. and Williams I. S. (2019) A new cache of Eoarchaean detrital zircons from the Singhbhum craton, eastern India and constraints on early Earth geodynamics. *Geoscience Frontiers* **10**, 1359–1370.

Stein H. and Hannah J. (2014) Rhenium–Osmium Geochronology: Sulfides, Shales, Oils, and Mantle. In *Encyclopedia of Scientific Dating Methods* (eds. W. J. Rink and J. Thompson). Springer Netherlands, Dordrecht. pp. 1–25.

Stein H. J. (2014) Dating and Tracing the History of Ore Formation. In *Treatise on Geochemistry (Vol. 13)* (eds. H. D. Holland and K. K. Turekian). Elsevier. pp. 87–118.

Stern R. A. and Bleeker W. (1998) Age of the World's Oldest Rocks Refined Using Canada's SHRIMP: The Acasta Gneiss Complex, Northwest Territories, Canada. *Geoscience Canada* **25**, 27–31.

Syverson D. D., Katchinoff J. A. R., Yohe L. R., Tutolo B. M., Seyfried W. E. and Rooney A. D. (2021) Experimental partitioning of osmium between pyrite and fluid: Constraints on the mid-ocean ridge hydrothermal flux of osmium to seawater. *Geochimica et Cosmochimica Acta* **293**, 240–255.

Thompson K. J., Kenward P. A., Bauer K. W., Warchola T., Gauger T., Martinez R., Simister R. L., Michiels C. C., Llirós M., Reinhard C. T., Kappler A., Konhauser K. O. and Crowe S. A. (2019) Photoferrotrophy, deposition of banded iron formations, and methane production in Archean oceans. *Science Advances* **5**, eaav2869.

Trendall A. F. (2002) The Significance of Iron-Formation in the Precambrian Stratigraphic Record. In *Precambrian Sedimentary Environments* (eds. W. Altermann and P. L. Corcoran). Wiley. pp. 33–66.

Valley J. W., Peck W. H., King E. M. and Wilde S. A. (2002) A cool early Earth. *Geology* **30**, 351–354.

Van Acken D., Thomson D., Rainbird R. H. and Creaser R. A. (2013) Constraining the depositional history of the Neoproterozoic Shaler Supergroup, Amundsen Basin, NW Canada: Rhenium-osmium dating of black shales from the Wynniatt and Boot Inlet Formations. *Precambrian Research* **236**, 124–131.

Van Hise C. R. and Leith C. K. (1911) *The geology of the Lake Superior region*., United States Geological Survey, 1-641.

Vermeesch P. (2018) IsoplotR: A free and open toolbox for geochronology. *Geoscience Frontiers* **9**, 1479–1493.

Viehmann S. (2016) The evolution of Precambrian environments and their impact on the trace element and Hf-Nd isotopic compositions of ancient seawater. PhD thesis, Jacobs University Bremen.

Viehmann S., Bau M., Bühn B., Dantas E. L., Andrade F. R. D. and Walde D. H. G. (2016) Geochemical characterisation of Neoproterozoic marine habitats: Evidence from trace elements and Nd isotopes in the Urucum iron and manganese formations, Brazil. *Precambrian Research* **282**, 74–96.

Viehmann S., Bau M., Hoffmann J. E. and Münker C. (2015a) Geochemistry of the Krivoy Rog Banded Iron Formation, Ukraine, and the impact of peak episodes of increased global magmatic activity on the trace element composition of Precambrian seawater. *Precambrian Research* **270**, 165–180.

Viehmann S., Bau M., Smith A. J. B., Beukes N. J., Dantas E. L. and Bühn B. (2015b) The reliability of ~2.9 Ga old Witwatersrand banded iron formations (South Africa) as

archives for Mesoarchean seawater: Evidence from REE and Nd isotope systematics. *Journal of African Earth Sciences* **111**, 322–334.

Walker R. J. (2009) Highly siderophile elements in the Earth, Moon and Mars: Update and implications for planetary accretion and differentiation. *Geochemistry* **69**, 101–125.

Walker R. J. (2015) Rhenium–Osmium Dating (Meteorites). In *Encyclopedia of Scientific Dating Methods* (eds. W. Jack Rink and J. W. Thompson). Encyclopedia of Earth Sciences Series. Springer Netherlands, Dordrecht. pp. 703–707.

Wendt I. and Carl C. (1991) The statistical distribution of the mean squared weighted deviation. *Chemical Geology: Isotope Geoscience section* **86**, 275–285.

Wernitznig S. (2023) Geochemical investigation of impactites from the Boltysh impact structure and possible relationship to early Danian sediments from the Umbria-Marche Basin, Italy. Master's thesis, University of Vienna.

Wilde S. A., Valley J. W., Peck W. H. and Graham C. M. (2001) Evidence from detrital zircons for the existence of continental crust and oceans on the Earth 4.4 Gyr ago. *Nature* **409**, 175–178.

Woodhouse O. B., Ravizza G., Kenison Falkner K., Statham P. J. and Peucker-Ehrenbrink B. (1999) Osmium in seawater: vertical profiles of concentration and isotopic composition in the eastern Pacific Ocean. *Earth and Planetary Science Letters* **173**, 223–233.

Woodland S. J., Pearson D. G. and Thirlwall M. F. (2002) A Platinum Group Element and Re–Os Isotope Investigation of Siderophile Element Recycling in Subduction Zones: Comparison of Grenada, Lesser Antilles Arc, and the Izu–Bonin Arc. *Journal of Petrology* **43**, 171–198.

Xiong Y. and Wood S. A. (1999) Experimental determination of the solubility of ReO_2 and the dominant oxidation state of rhenium in hydrothermal solutions. *Chemical Geology* **158**, 245–256.

Xiong Y. and Wood S. A. (2000) Experimental quantification of hydrothermal solubility of platinum-group elements with special reference to porphyry copper environments. *Mineralogy and Petrology* **68**, 1–28.

Yin L., Zhao P., Liu J. and Li J. (2023) Re-Os isotope system in organic-rich samples for dating and tracing: Methodology, principle, and application. *Earth-Science Reviews* **238**, 104317.

8 Appendix

A1: Isotope dilution

Isotope dilution mass spectrometry is a method for extremely accurate isotope measurements using a tracer solution, a so-called spike, composed of a known quantity of specific isotopes (Inghram, 1954; Heumann, 1992). For the studied HSE samples, a spike of ^{99}Ru-^{105}Pd-^{185}Re-^{190}Os-^{191}Ir-^{194}Pt was used.

The spike is then added to the samples studied, which then must be equilibrated. This has the effect that if subsequently any substance is lost, it does not influence the quality of the result. After measuring the equilibrated sample, the known isotopic composition of the spike is subtracted from the total signal to resolve the true isotopic composition of the sample (Inghram, 1954; Heumann, 1992).

A2: Recipe for chromatographic anion exchange wet chemistry

HSE Column Chemistry

Procedure	Reagents & Amounts
1st stage: Anion column (1 ml Resin)	
Resin cleaning	10 ml H_2O
	10 ml 6 M HNO_3
	10 ml conc. HCl
	2 ml H_2O
Equilibration	2 ml 1 M HCl
	2 ml 0.5 M HCl
Load sample	10 ml 0.5 M HCl
	5 ml 1 M HCl
	2 ml 0.8 M HNO_3
	2 ml 0.8 M HNO_3
Collect Re, Ir, Pt, Ru	15 ml conc. HCl
	2 ml H_2O
Collect Pd	15 ml conc HCl
Collect Pd	10 ml conc. HCl
Collect Pd	10 ml conc. HCl
Dried down and both cuts redissolved in 1 ml 1 M HCl	
2nd stage LN-Spec column	
Resin cleaning	4 ml H2O
	4 ml 6 M HCl
	5 ml 6 M HCl
	4 ml 2 M HF
	4 ml 6 M HCl
	4 ml 2 M HF
	4 ml H_2O
Equilibration	4 ml 1 M HCl
Load and Collect Pd	1 ml 1 M HCl
Collect Pd	4 ml 1 M HCl
Load and Collect Re, Ir, Pt, Ru	1 ml 1 M HCl
Collect Re, Ir, Pt, Ru	5 ml 1 M HCl
Cleaning	4 ml 2 M HF
	4 ml 2 M HF
	4 ml 6 M HCl
	4 ml 2 M HF
	4 ml 6 M HCl
	4 ml 2 M HF

Figure A1: *Procedure for chromatographic anion exchange wet chemistry (after Chu et al. 2014)*

A3: Os, Re and $^{187}Os/^{188}Os$ against Ti and Hf

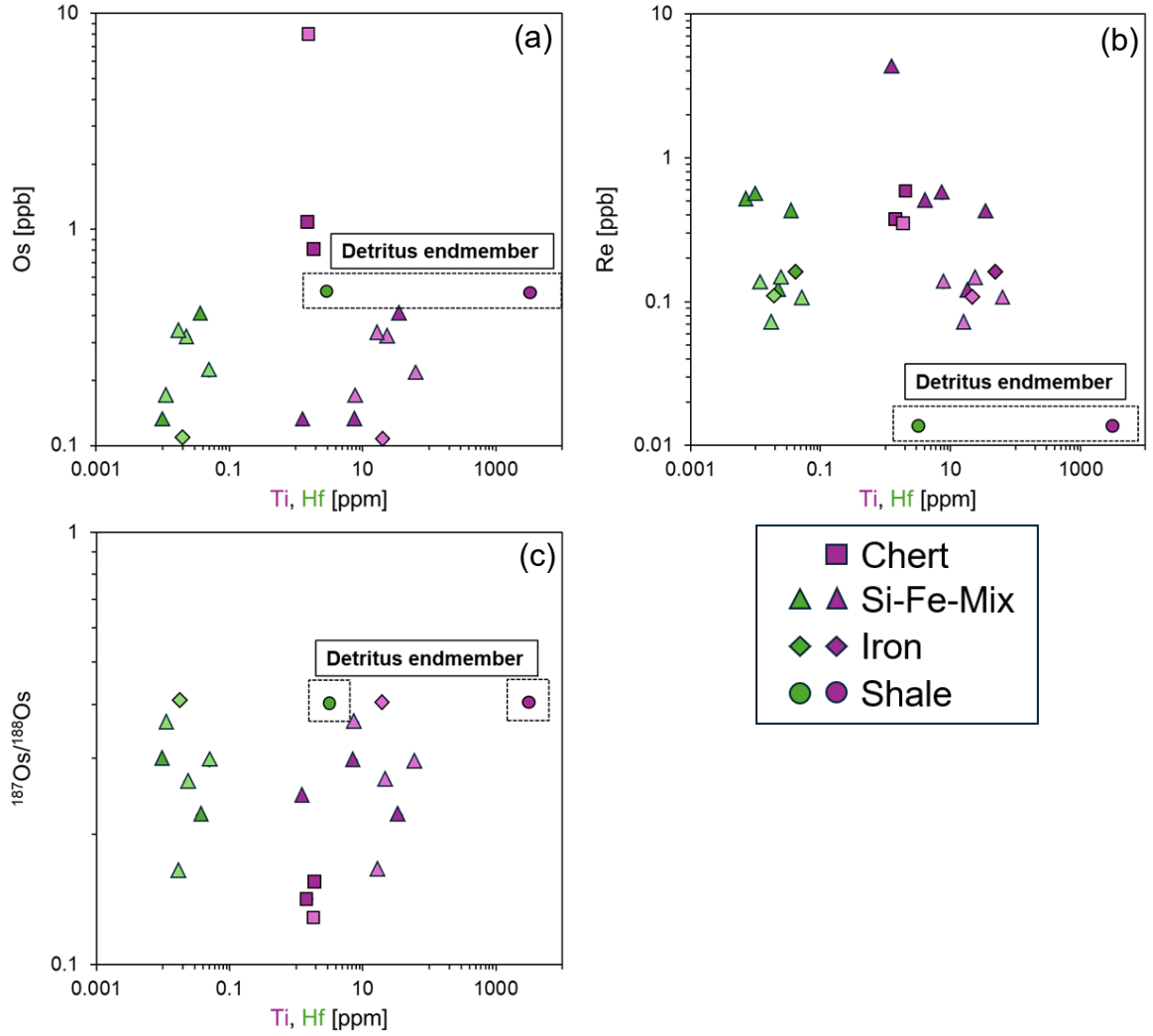

Figure A3a-c: *Diagrams of Os concentration (a), Re concentration (b) and the $^{187}Os/^{188}Os$ ratios (c) plotted against the Ti and Hf concentrations of the Tomka BIF samples. Samples in lighter color-scales indicate those with a PUM-like $(^{187}Os/^{188}Os)_0$. For some samples, no Os, Re and/or $^{187}Os/^{188}Os$ was measured, hence there are different numbers of data points in each plot.*

A4: Os, Re and $^{187}Os/^{188}Os$ against Ti/Fe and Hf/Fe

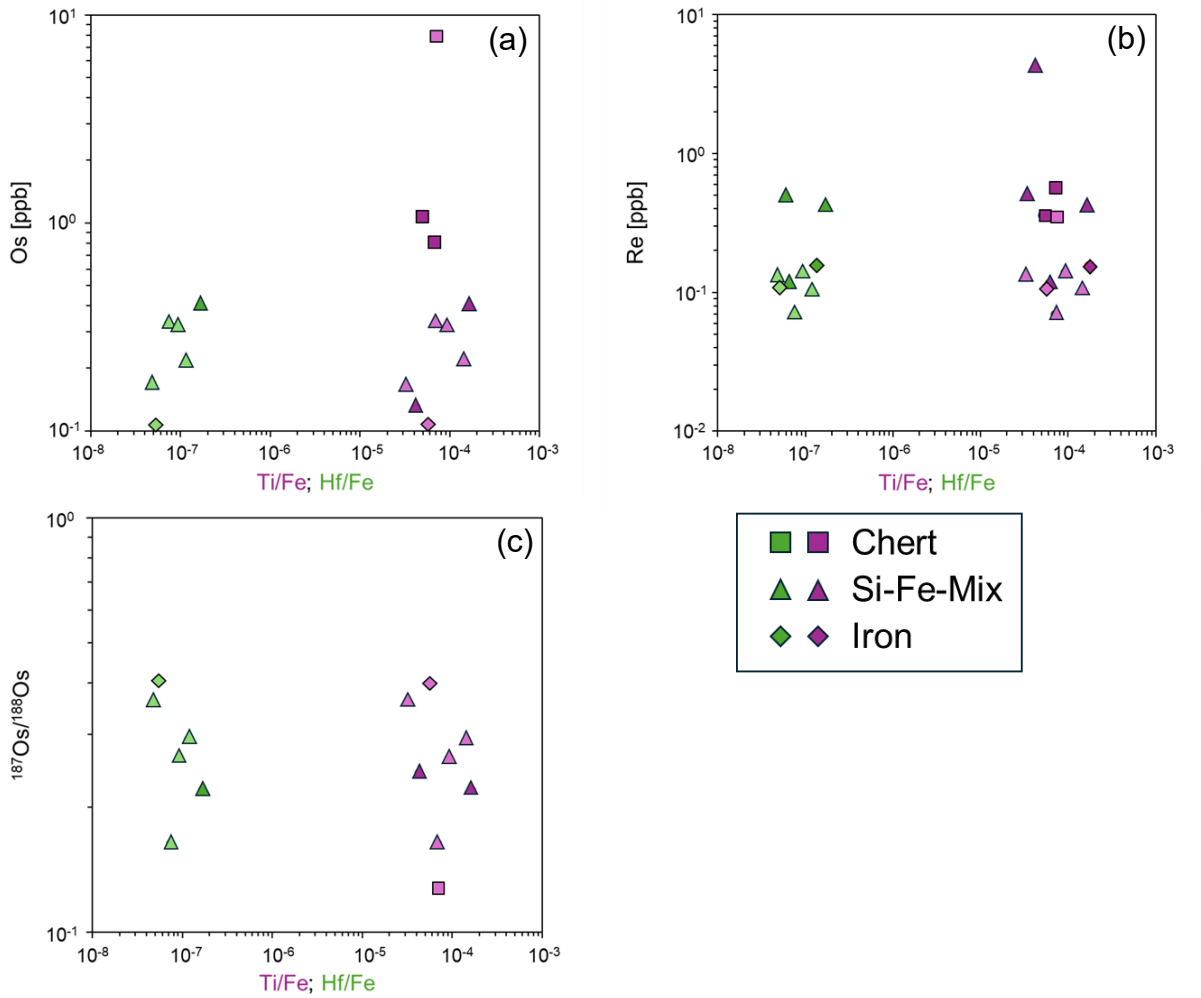

Figure A4a-c: *Diagrams of (a)Os concentration, (b) Re concentration and the(c) $^{187}Os/^{188}Os$ ratios plotted against the Fe normalized Ti and Hf concentrations of the Tomka BIF samples. No trend can be observed, which differentiate between the lithologies. The shale sample is not plotted, due to a lack of Fe abundance data being available. Samples in lighter color-scale indicate those with a PUM-like $(^{187}Os/^{188}Os)_0$. For some samples, no Os, Re and/or $^{187}Os/^{188}Os$ was measured, hence there are different numbers of data points in each plot.*

A5: Os, Re and $^{187}Os/^{188}Os$ against Al/Fe and Zr/Fe

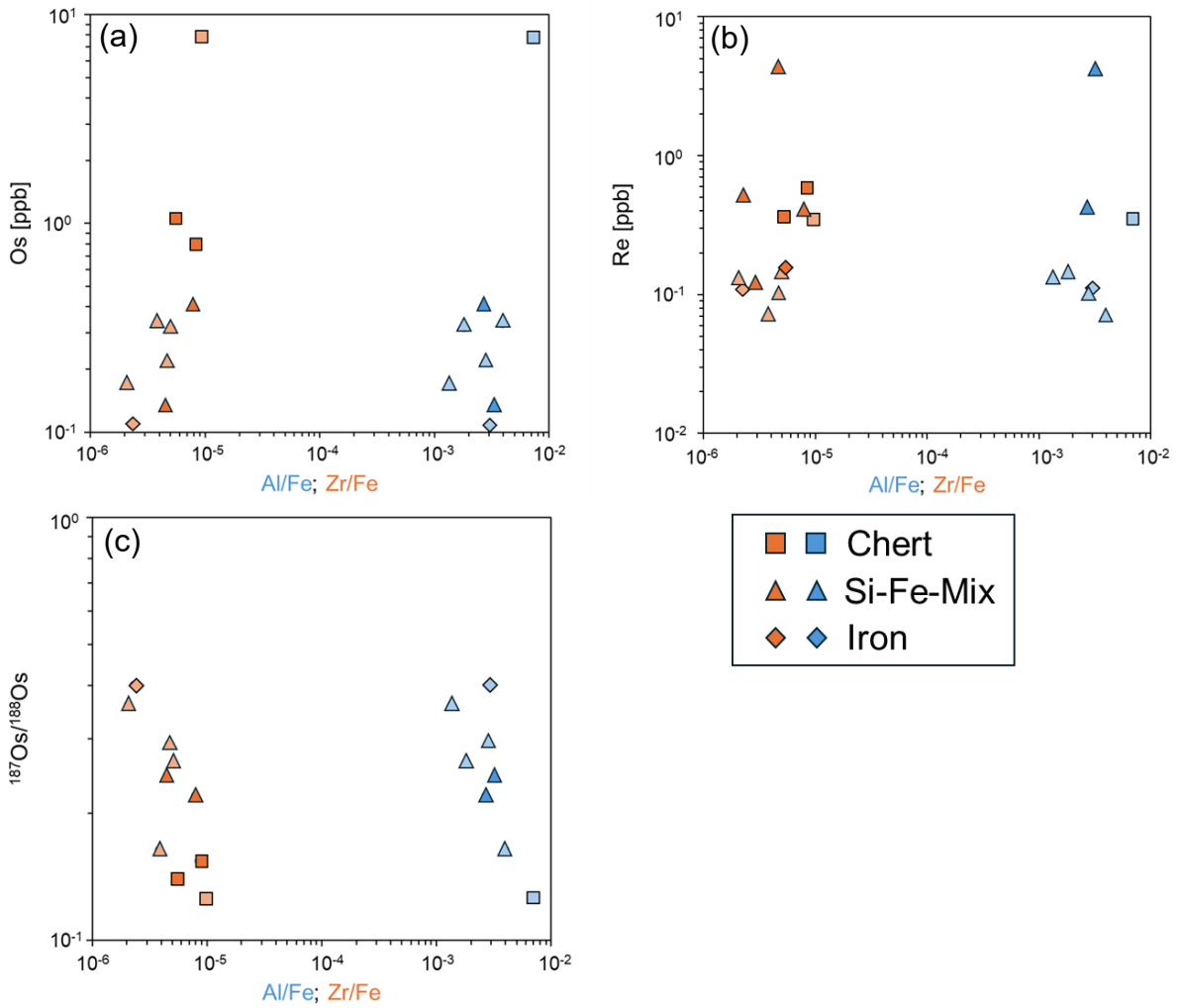

Figure A5a-c: *Diagrams of (a) Os concentration, (b) Re concentration and the (c) $^{187}Os/^{188}Os$ ratios plotted against the Fe normalized Al and Hf concentrations of the Tomka BIF samples. No trend can be observed, which differentiate the lithologies. The shale sample is not plotted, due to a lack of Fe abundance data being available. Samples in lighter color-scale indicate those with a PUM-like $(^{187}Os/^{188}Os)_0$. For some samples, no Os, Re and/or $^{187}Os/^{188}Os$ was measured, hence there are different numbers of data points in each plot.*

A6: Y/Ho vs Zr plot published with permission of Kienle 2024

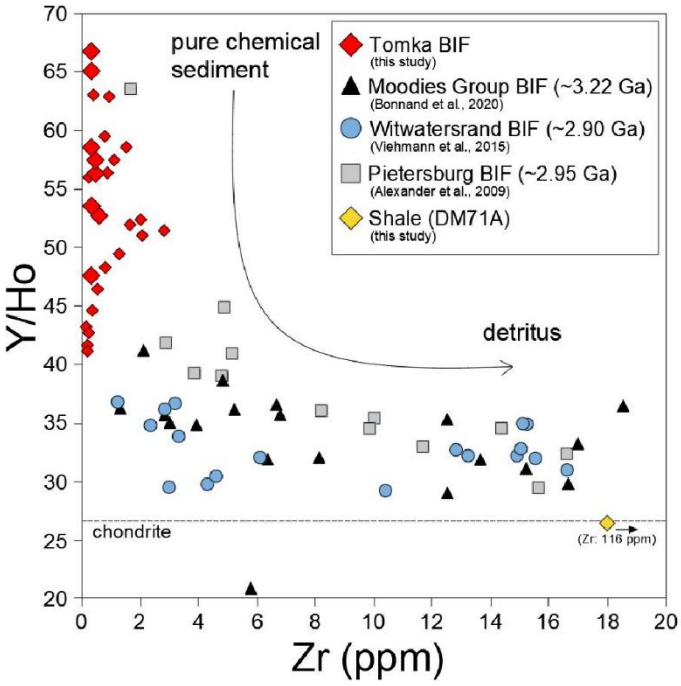

Figure A6: *Plot of Y/Ho ratio vs. Zr concentration of Meso- and Paleoarchean BIF, including the Tomka BIF (Kienle 2024). Pure chemical sediments have super-chondritic Y/Ho ratios and low concentrations of immobile elements. The Y/Ho ratios decrease towards chondritic ratios as Zr-concentrations increase, indicating increasing detrital contamination.*

A7: Os, Re, $^{187}Os/^{188}Os$ and Re/Os against Sr

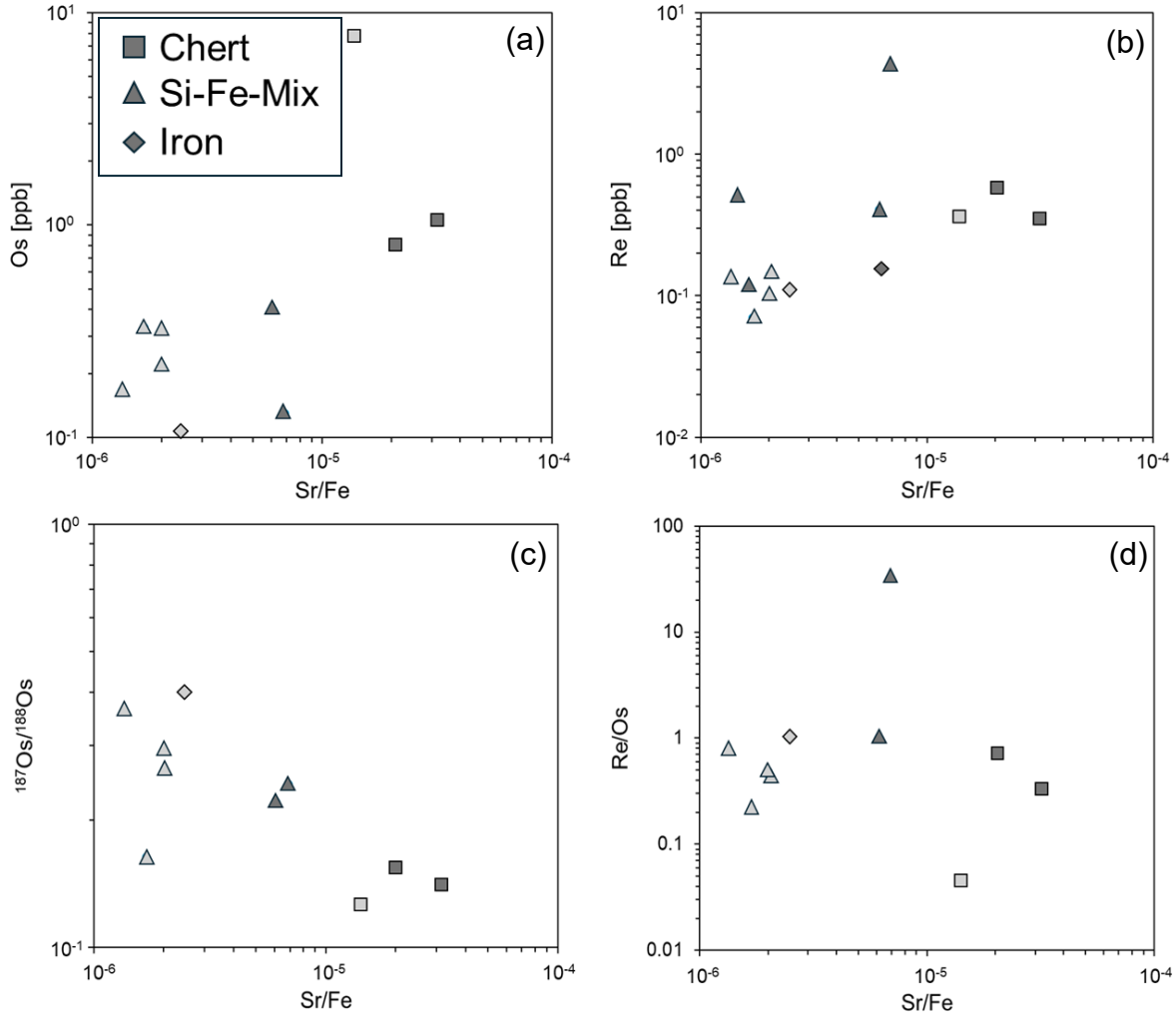

Figure A7a-d: *Diagrams of the (a) Os concentration, (b) Re concentration, (c) $^{187}Os/^{188}Os$ ratios and (d) the Re/Os ratio plotted against the Fe normalized Sr concentrations of the Tomka BIF samples. Samples in lighter color-scale indicate those with a PUM-like $(^{187}Os/^{188}Os)_0$. For some samples, no Os, Re and/or $^{187}Os/^{188}Os$ was measured, hence there are different numbers of data points in each plot.*

A8: Isochron regression and error statistics

To plot the regression lines, the program IsoplotR was used, developed by Vermeesch (2018). For the results presented in this study, the data are often overly dispersed, meaning the data points scatter more than what is to be expected based on the analytical uncertainties. To test if the presented data set is overly dispersed, first the chi-square statistic χ^2_{stat} is calculated. Based on the chi-square statistic, the p-value can be defined, which is the probability that a datapoint i has a value higher than the χ^2_{stat} under a chi-square distribution (Vermeesch, 2018). The typical value chosen for p is often 0.05, as is for IsoplotR. If now the presented data falls below this chosen p-value the data would be overdispersed, if it is much greater than 0.05 it would be underdispersed (Vermeesch, 2018). A second method of monitoring if the dataset is over- or underdispersed is by calculating the MSWD (Mean square weighted deviation). It measures how much a datapoint i deviates from the best-fit line relative to the expected analytical uncertainty (Wendt and Carl, 1991). It can be calculated by dividing the chi-square statistic χ^2_{stat} by the degrees of freedom df (Vermeesch, 2018). For details on how the chi-square statistic and the MSWD is calculated in IsoplotR, the reader is referred to Vermeesch (2018), where the methodology is described in detail.

In general, three different modes of the MSWD can be distinguished: MSWD << 1, MSWD ≈ 1 and the MSWD >> 1. If the mean square weighted deviates are much smaller than 1, then the calculated analytical errors are too large and the dataset would be overdispersed. The opposite, calculated analytical errors being too small, could be the case if the MSWD is greater than 1. Another possibility could be geologically induced scattering. If the MSWD is roughly 1, it indicates that the data points fit their calculated uncertainties (Stein, 2014).

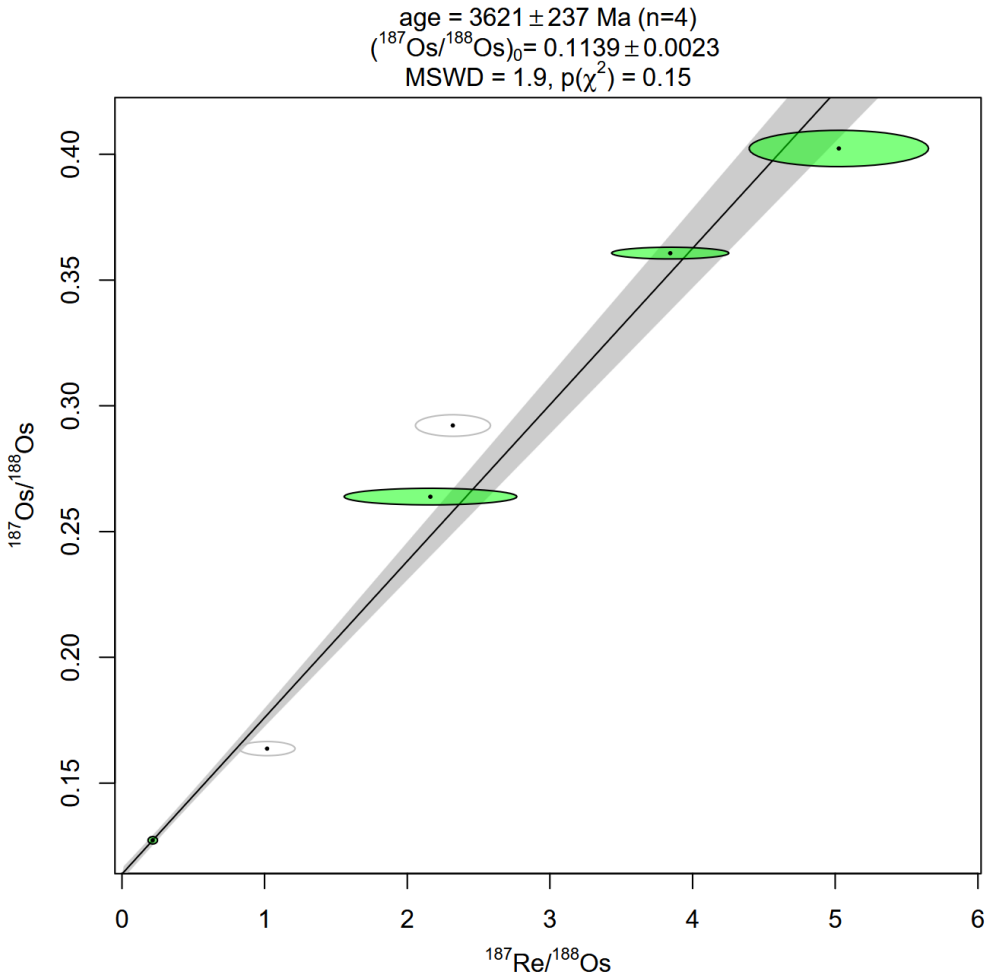

Figure A8: *Isochron diagram using only four of the six samples with a PUM-like initial Os isotopic ratio and omitting sample number DM22B3 and DM22B4. This "age" of 3,621 Ma has a much lower error, although still high, of "only" ± 237 Ma and only minor amount of overdispersion. The small sample size brings the question of how relevant this result is. Green ellipses around the datapoints represent the x- and y-errors. A data point with no such error is the sample excluded from the "age" calculation. The linear regression and the "age" were calculated using the program IsoplotR (version 6.4.2).*

A9: Trace element concentrations (in ppm) in the Tomka BIF published with permission of Kienle 2024

	DM71A	DM17D1	DM17D2	DM17C2	DM22D1	DM22D2	IND-DGB-BIF2 1a	IND-DGB-BIF2 2	IND-DGB-BIF2 4	IND-DGB-BIF2 5	IND-DGB-BIF2 6	DM22B2	DM22B3	DM22B4	DM90-2
ppm	Clay	Chert	Chert	Chert	Iron	Iron	Mix	Mix	Mix	Mix	Mix	Mix	Mix	Mix	Mix
Fe		31861.2	24195	29151.9	357020	288247	251917.7265	238656.2827	213913.0353		29529.80652	323314	236168	430922	118458
Li	4.286	0.574	0.578	0.627	0.324	0.586	0.297	0.176	0.241	0.303	0.223	0.047	0.049	0.099	0.054
Al	97037	/	171	/	1058	1642	456	321	575	353	94.2	1094	934	1219	147
P	426	57.5	46.7	52.1	74.5	131	217	247	154	56.3	47.5	64.0	60.9	87.0	51.0
Sc	8.218	0.586	0.353	0.390	0.749	1.061	0.461	0.310	0.495	0.101	0.068	0.794	0.591	0.901	0.147
Ti	3148	1.60	1.69	1.95	19.82	48.64	23.09	7.73	35.44	7.48	1.24	19.30	16.49	61.90	4.01
Co	3.524	2.258	0.741	2.599	3.947	5.266	4.019	6.676	8.196	1.151	1.157	3.580	2.417	5.003	1.430
Ni	65.0	36.1	31.0	29.5	51.3	76.9	51.9	86.9	76.4	28.2	24.8	59.1	44.0	76.5	46.0
Cu	/	0.711	2.208	1.471	/	0.165	/	7.712	0.282	/	10.53	/	/	1.078	/
Rb	85.42	0.037	0.089	0.110	0.205	0.209	0.140	0.077	0.328	0.276	0.044	0.859	1.122	1.405	0.029
Sr	42.73	1.033	0.341	0.598	0.873	1.820	0.506	0.319	1.310	0.619	0.204	0.524	0.397	0.859	0.170
Y	11.02	0.296	0.483	0.594	7.552	8.788	5.054	8.432	27.30	3.015	0.990	8.062	6.727	16.67	10.08
Zr	116	0.170	0.229	0.244	0.812	1.533	1.298	0.492	1.687	0.589	0.133	0.954	0.891	2.011	0.271
Nb	8.165	0.015	0.015	0.012	0.096	0.155	0.105	0.064	0.127	0.072	0.014	0.090	0.115	0.170	0.041
Mo	/	4.252	4.972	3.051	3.687	6.588	4.826	9.993	6.391	4.089	3.534	4.705	4.336	5.879	5.166
Cd	/	0.014	0.019	0.012	0.024	0.033	0.019	0.021	0.019	0.011	0.007	0.017	0.015	0.021	0.011
Cs	/	0.007	0.009	0.010	0.007	0.009	0.136	0.118	0.137	0.133	0.105	0.012	0.018	0.022	0.008
Ba	517	8.489	3.622	4.085	4.500	8.118	2.783	/	4.554	2.974	< LOQ	5.556	7.037	9.000	0.491
La	16.51	0.059	0.066	0.085	4.479	13.47	0.410	0.593	2.440	0.521	0.204	1.337	0.958	3.561	0.753
Ce	32.81	0.095	0.088	0.135	2.472	5.808	0.557	0.756	3.112	0.438	0.136	1.656	1.202	4.710	0.870
Pr	3.702	0.013	0.009	0.015	0.412	0.860	0.069	0.103	0.385	0.057	0.019	0.239	0.182	0.567	0.104
Nd	13.29	0.062	0.043	0.067	1.596	2.980	0.324	0.507	1.762	0.246	0.081	1.054	0.821	2.507	0.431
Sm	2.748	0.018	0.012	0.019	0.275	0.422	0.113	0.170	0.529	0.077	0.024	0.269	0.229	0.622	0.112
Eu	0.783	0.010	0.012	0.014	0.146	0.220	0.088	0.136	0.383	0.051	0.017	0.179	0.142	0.419	0.106
Gd	2.580	0.025	0.029	0.039	0.474	0.723	0.297	0.413	1.415	0.160	0.048	0.444	0.379	1.114	0.427
Tb	0.365	0.004	0.006	0.006	0.069	0.094	0.056	0.069	0.268	0.028	0.008	0.068	0.066	0.178	0.076
Dy	2.046	0.027	0.042	0.049	0.494	0.612	0.415	0.548	2.045	0.220	0.063	0.492	0.464	1.271	0.576
Ho	0.419	0.007	0.009	0.012	0.127	0.150	0.102	0.147	0.526	0.057	0.017	0.128	0.119	0.318	0.155
Er	1.326	0.024	0.030	0.041	0.399	0.479	0.334	0.479	1.629	0.193	0.057	0.413	0.375	1.002	0.492
Tm	0.200	0.004	0.004	0.006	0.055	0.067	0.051	0.068	0.212	0.029	0.007	0.057	0.054	0.139	0.067
Yb	1.411	0.031	0.028	0.045	0.352	0.429	0.346	0.439	1.273	0.187	0.056	0.365	0.344	0.858	0.427
Lu	0.212	0.005	0.004	0.008	0.056	0.068	0.059	0.076	0.204	0.030	0.009	0.061	0.056	0.141	0.071
Hf	3.179	/	/	/	0.019	0.038	0.023	0.011	0.035	0.010	/	0.021	0.017	0.050	0.007
Ta	0.542	/	/	/	/	0.012	/	/	0.013	/	/	/	/	0.013	/
W		0.632	0.731	0.237	1.027	1.490	2.508	3.288	1.649	1.008	0.283	0.864	1.302	0.683	0.948
Pb	4.743	0.215	0.264	0.188	0.666	1.062	1.236	1.217	1.249	0.733	0.478	0.446	0.529	0.593	0.728
Th	5.871	0.004	0.004	0.004	0.033	0.076	0.034	0.012	0.061	0.012	0.003	0.024	0.025	0.089	0.009
U	1.366	0.002	0.003	0.002	0.012	0.020	0.020	0.018	0.021	0.006	0.002	0.015	0.011	0.024	0.013
Y/Ho	26.26	43.19	53.45	47.59	59.36	58.52	49.41	57.37	51.87	52.62	58.49	62.90	56.39	52.40	65.12
Th/U	4.299	2.348	1.615	2.185	2.751	3.770	1.678	0.642	2.873	2.064	1.757	1.615	2.405	3.645	0.661
PAAS normalized	**DM71A**	**DM17D1**	**DM17D2**	**DM17C2**	**DM22D1**	**DM22D2**	**IND-DGB-BIF2 1a**	**IND-DGB-BIF2 2**	**IND-DGB-BIF2 4**	**IND-DGB-BIF2 5**	**IND-DGB-BIF2 6**	**DM22B2**	**DM22B3**	**DM22B4**	**DM90-2**
Element in ppm	Clay	Chert	Chert	Chert	Iron	Iron	Mix	Mix	Mix	Mix	Mix	Mix	Mix	Mix	Mix
La	0.432	0.002	0.002	0.002	0.117	0.353	0.011	0.016	0.064	0.014	0.005	0.035	0.025	0.093	0.020
Ce	0.412	0.001	0.001	0.002	0.031	0.073	0.007	0.010	0.039	0.006	0.002	0.021	0.015	0.059	0.011
Pr	0.419	0.001	0.001	0.002	0.047	0.097	0.008	0.012	0.044	0.006	0.002	0.027	0.021	0.064	0.012
Nd	0.392	0.002	0.001	0.002	0.047	0.088	0.010	0.015	0.052	0.007	0.002	0.031	0.024	0.074	0.013
Pm	/	/	/	/	/	/	/	/	/	/	/	/	/	/	/
Sm	0.495	0.003	0.002	0.003	0.049	0.076	0.020	0.031	0.095	0.014	0.004	0.049	0.041	0.112	0.020
Eu	0.725	0.009	0.011	0.013	0.135	0.203	0.081	0.126	0.354	0.047	0.016	0.166	0.132	0.388	0.098
Gd	0.554	0.005	0.006	0.008	0.102	0.155	0.064	0.089	0.304	0.034	0.010	0.095	0.081	0.239	0.092
Tb	0.472	0.005	0.007	0.008	0.089	0.121	0.073	0.090	0.346	0.036	0.011	0.088	0.085	0.230	0.099
Dy	0.437	0.006	0.009	0.010	0.106	0.131	0.089	0.117	0.437	0.047	0.013	0.105	0.099	0.272	0.123
Y	0.408	0.011	0.018	0.022	0.280	0.325	0.187	0.312	1.011	0.112	0.037	0.299	0.249	0.618	0.373
Ho	0.423	0.007	0.009	0.013	0.128	0.152	0.103	0.148	0.531	0.058	0.017	0.129	0.120	0.321	0.156
Er	0.465	0.009	0.010	0.014	0.140	0.168	0.117	0.168	0.571	0.068	0.020	0.145	0.131	0.352	0.173
Tm	0.495	0.010	0.011	0.016	0.137	0.164	0.125	0.169	0.524	0.071	0.018	0.141	0.132	0.343	0.165
Yb	0.500	0.011	0.010	0.016	0.125	0.152	0.123	0.156	0.451	0.066	0.020	0.130	0.122	0.304	0.151
Lu	0.489	0.012	0.010	0.018	0.130	0.157	0.137	0.175	0.471	0.070	0.020	0.140	0.129	0.326	0.163
Y/Ho [g/g]	0.964	1.585	1.962	1.747	2.179	2.148	1.814	2.106	1.904	1.931	2.147	2.309	2.070	1.923	2.390
(Ce/Ce*)A	0.923	1.035	1.370	1.286	0.672	0.682	1.143	1.122	1.113	0.987	0.930	0.906	0.894	1.084	1.002
(Pr/Pr*)	1.043	0.987	0.874	0.898	1.194	1.211	0.947	0.958	0.956	1.006	1.031	1.042	1.046	0.965	0.999
Sm/Yb	0.989	0.287	0.216	0.217	0.397	0.500	0.166	0.197	0.211	0.210	0.215	0.375	0.338	0.368	0.133
Eu/Sm	1.465	3.003	5.057	3.702	2.731	2.672	3.988	4.119	3.713	3.358	3.662	3.421	3.188	3.465	4.876
Eu/Eu*	1.488	2.455	2.825	2.560	2.157	2.229	2.150	2.510	1.981	2.214	2.469	2.692	2.356	2.566	2.122
Gd/Gd*	1.093	1.159	1.117	1.408	1.407	1.381	1.129	1.426	1.194	1.417	1.354	1.347	1.144	1.274	1.235
La/La*	/	1.890	3.008	2.262	2.558	3.028	2.436	2.976	2.391	2.873	3.435	1.850	1.894	2.077	1.973
Yb/Pr	/	7.398	9.538	9.732	2.672	1.561	15.65	13.29	10.36	10.36	9.469	4.793	5.938	4.733	12.82